Universidad de Jaén

Escuela de Doctorado

TESIS DOCTORAL

•

GENERACIÓN CONTROLADA DE BURBUJAS Y ESTUDIO DE SU DINÁMICA COLECTIVA

PRESENTADA POR:
JAVIER RUIZ RUS

DIRIGIDA POR:
PROF. CARLOS MARTÍNEZ BAZÁN
DRA. ROCÍO BOLAÑOS JIMÉNEZ
DR. ALEJANDRO SEVILLA SANTIAGO

JAÉN, OCTUBRE 2019

Universidad de Jaén

Controlled formation of bubbles and analysis of their collective dynamics

Tesis Doctoral

Autor
Javier Ruiz Rus

Directores
Prof. Carlos Martínez Bazán
Dra. Rocío Bolaños Jiménez
Dr. Alejandro Sevilla Santiago

Jaén, Octubre 2019

DEPARTAMENTO DE INGENIERÍA MECÁNICA Y MINERA
Escuela Politécnica Superior de Jaén

Controlled formation of bubbles and analysis of their collective dynamics

Generación controlada de burbujas y estudio de su dinámica colectiva

Autor
Javier Ruiz Rus

Directores de Tesis
Prof. Carlos Martínez Bazán
Dra. Rocío Bolaños Jiménez
Dr. Alejandro Sevilla Santiago

Jaén, Octubre 2019

A mis padres y, por supuesto, a Inma

Cuentan de un sabio, que un día
tan pobre y mísero estaba,
que sólo se sustentaba
de unas yerbas que cogía.
"Habrá otro", entre sí decía,
"más pobre y triste que yo?"
Y cuando el rostro volvió,
halló la respuesta, viendo
que iba otro sabio cogiendo
las hojas que él arrojó.

La vida es sueño
Pedro Calderón de la Barca

He who marches out of step hears another drum

One flew over the cuckoo's nest
Ken Kesey

Cuando ayunéis, no pongáis cara triste, como los hipócritas;
porque ellos desfiguran sus rostros,
para mostrar a los hombres que están ayunando.
Pero tú cuando ayunes, unge tu cabeza y lava tu rostro,
para no hacer ver a los hombres que ayunas.

Mateo 6:16-18

Tesis doctoral

Controlled formation of bubbles and analysis of their collective dynamics

Autor: Javier Ruiz Rus

Directores de Tesis:
Prof. Carlos Martínez Bazán
Dra. Rocío Bolaños Jiménez
Dr. Alejandro Sevilla Santiago

Firma del Tribunal Calificador:

Firma

Presidente:
Vocal:
Secretario:
Suplente:
Suplente:

Calificación:

Jaén, de Octubre de 2019

Agradecimientos

Aunque dar las gracias por escrito hace que se pierda la verdadera esencia de la gratitud, quisiera dejar constancia de todas las personas que han contribuido a que este trabajo haya sido posible.

En primer lugar a mis directores, a Rocío por darme la oportunidad de realizar este trabajo, a Alejandro por su brillante visión y a Carlos, ejemplo a seguir en todos los aspectos, tu motivación es el impulso que nos mueve a todos.

También a todos los miembros del Grupo de Mecánica de Fluidos de Jaén. A Manu por todo lo que hemos aprendido juntos y por compartir la pasión sin la que esto que hacemos sería impensable. A José Carlos por haberme enseñado tantas cosas, pero sobre todo por mostrarme el camino para aprenderlas. A José Ignacio por ser ejemplo de devoción y esfuerzo contínuo. A Cándido por su particular visión de este mundo; a Mariano, del que no me dio tiempo a aprender todo lo que me podía ofrecer y a Carlos. Por supuesto a Cosme por intentar materializar todos los esquemas que tórpemente le dibujaba y también a Alejandro y Mario, siempre pacientes.

Quiero mostrar mi gratitud a Véronique y a Patricia, por haberme dado la oportunidad de aprender de ellas durante mi estancia en el IMFT de Toulouse, vuestro esfuerzo desinteresado tanto en el plano profesional como personal es una deuda difícil de subsanar. También a todos los compañeros del IMFT que tan amablemente me acogieron y ayudaron, especialmente a Clément, Adrien, Samuel y Esli. Y a todos los investigadores de allí o que pasaron por allí y altruistamente se interesaron en mi trabajo ofreciéndome ayuda y consejo, especialmente a S. Cazin, N. Rimbert, D. Lo Jacono, J. Sebilleau y M. Obligado.

Me gustaría dedicar unas líneas de reconocimiento a todos los participantes del Workshop, como ejemplo de unidad y motivación en este campo que tanto nos gusta. Gracias a Javier, José Manuel, Ignacio, Guillaume, Paco, Luis y Fran, entre otros muchos, por intentar inculcarnos vuestra pasión y algo de vuestro conocimiento. También a todos los compaẽros y amigos, Patri, Alejandro, Enrique, Pablo, Désirée y tantos otros que compartimos el mismo destino.

En cuanto al plano personal, no hay palabras suficientes para agradecer a mi familia todo lo que hacen por mí y la confianza y amor que me brindan día a día. Gracias de corazón.

Y finalmente, gracias a Inma, la gran artífice de este trabajo. Compañera y amiga infatigable, que ha soportado más que nadie las consecuencias de esta labor agotadora. Ya sabes de sobra todo lo que te agradezco el infinito apoyo que me has ofrecido, la paciencia y el cariño. Sin ti, está claro que no hubiese sido posible.

Resumen

Las emergentes aplicaciones de las burbujas a la industria y la medicina han hecho surgir nuevos retos de carácter ingenieril. Gran parte de ellos están relacionados con los procesos de generación de burbujas y con la dinámica asociada a su movimiento, ya sea de forma aislada o colectiva en flujos multifase. En esta Tesis doctoral se presentan estudios experimentales dirigidos a analizar la generación controlada de burbujas en diferentes configuraciones y a caracterizar la dinámica colectiva de enjambres de burbujas que evolucionan debido a la coalescencia.

En la primera parte, se analizan de forma experimental dos métodos diferentes destinados al control activo del proceso de generación de burbujas en corrientes no confinadas de agua-aire en configuración de co-flujo. Estos métodos se han implementado en dos geometrías diferentes, por un lado una configuración plana de corrientes agua-aire-agua bajo condiciones de alimentación de caudal de aire constante; en segundo lugar se ha utilizado una configuración de chorro axilsimétrica en la que el caudal de aire varía a lo largo del ciclo de burbujeo.

En la primera configuración, la frecuencia de formación de burbujas se controla mediante perturbaciones simétricas de la corriente de agua generadas periódicamente mediante la modulación sinusoidal de la velocidad de salida del agua. La amplitud de las variaciones de velocidad del líquido se ha obtenido a través de las fluctuaciones de presión medidas en la corriente de líquido. La efectividad del proceso de forzado se ha caracterizado por medio del análisis de la señal temporal de presión en el aire junto con imágenes de alta velocidad del proceso de burbujeo. Se ha observado que el proceso de burbujeo puede ser controlado por medio de amplitudes de forzado mayores a un determinado valor crítico, dando lugar a burbujas monodispersas generadas a la frecuencia de forzado seleccionada. Finalmente, se han caracterizado de forma cualitativa los efectos del forzado mediante una formulación unidimensional de las ecuaciones de continuidad y conservación de cantidad de movimiento en la lámina de agua, manteniendo los efectos de la tensión superficial pero despreciando el efecto de la corriente interna de aire.

El segundo método de forzado propuesto supone una técnica fácil de implementar y que permite un control preciso de la producción de burbujas en co-flujos cilíndricos, pudiendo controlarse de forma independiente tanto la frecuencia de generación como el volumen de las burbujas generadas. Para conseguir generar burbujas a la frecuencia deseada, se ha incorporado un dispositivo de forzado basado en la actuación de un altavoz en la línea de alimentación de gas de un sistema de co-flujo con inyector de longitud corta. Por lo tanto, la fase gaseosa se fuerza mediante una modulación de presión que induce una variación del caudal de gas que alimenta a la burbuja. El proceso forzado de generación de burbujas

se ha caracterizado experimentalmente para diferentes frecuencias. Para ello, el burbujeo que se establece de forma natural en este tipo de configuración, es impuesto, dando lugar a la generación de burbujas sincronizada a la frecuencia de forzado seleccionada, siempre y cuando la amplitud de la señal de presión introducida sea lo suficientemente grande. El análisis detallado de la evolución de la entrefase de la burbuja ha permitido describir el proceso forzado de generación y los diferentes regímenes que se establecen. Finalmente, dicho proceso controlado de formación de burbujas se ha modelado mediante la ecuación de Rayleigh-Plesset para crecimiento esférico, despreciando los efectos de la viscosidad.

La segunda parte de esta Tesis está dirigida al estudio experimental de la dinámica de la población de burbujas en enjambres confinados que ascienden debido a la flotabilidad a altos números de Reynolds. Para investigar la evolución de la población durante el ascenso, se han realizado diversos experimentos con inyección de diferentes fracciones de volumen de gas, registrando imágenes del enjambre en diferentes posiciones. La evolución de la distribución de tamaños presentes en la población se ha obtenido mediante el análisis digital de las imágenes registradas, haciendo uso de un algoritmo de detección y clasificación de burbujas, especialmente desarrollado para esa tarea. Se han observado grandes cambios en la función de densidad de probabilidad de tamaños de burbuja a lo largo de la dirección vertical, principalmente debido a la coalescencia de las burbujas. Los mecanismos que dan lugar a la coalescencia se han identificado a través de un análisis estadístico de las colisiones detectadas en las imágenes. Finalmente, se han llevado a cabo experimentos adicionales, a altas velocidades de grabación, para determinar la frecuencia de coalescencia en el enjambre como una función de la distribución de tamaños. El método de seguimiento de burbujas ha sido especialmente diseñado para detectar cada uno de los eventos de coalescencia que tienen lugar en las diferentes posiciones.

Palabras clave: Formación de burbujas, burbujeo forzado, chorros con coflujo, coalescencia, frecuencia de coalescencia, ecuación de balance de población.

Abstract

The current applications of bubbles to industry and medicine present several challenging engineering problems. Most of them are related to the bubble generation process and the dynamics involved in their motion either as isolated bubbles or in a bubbly flow. This PhD dissertation presents experimental studies based on the controlled bubble generation under different configurations as well as on the dynamics of confined bubble swarms whose evolution is governed by coalescence.

In the first part, two different methods to actively control the bubble formation process in unbounded air-liquid co-flowing streams are experimentally analyzed. They have been implemented in two geometries, namely a planar water-air-water co-flow configuration with constant air flow rate feeding conditions, and an axisymmetric air-water co-flowing jet in which the air flow rate varies during the bubbling cycle.

In the first configuration, the bubble generation frequency is controlled by means of symmetrical dilational perturbations that are periodically induced on the water streams through the sinusoidal modulation of the water velocity at the nozzle exit. In this work, the amplitude of the induced liquid velocity variations has been obtained through the measurements of the pressure fluctuations in the liquid stream. Moreover, the effectiveness of the forcing process has been characterized by analyzing the temporal evolution of the air pressure at the outlet and the images extracted from high-speed movies. It has been found that the bubbling process can be properly controlled by critical values of the forcing amplitude, giving rise to the formation of monodisperse bubbles generated at the selected forcing frequency. The forcing effect has been qualitatively characterized by a one-dimensional formulation of the leading order continuity and momentum equation of the liquid sheet, keeping the surface tension effects but neglecting the inner air stream effects.

The second forcing method proposed represents an easy-to-implement technique to accurately control the bubble production in cylindrical gas-liquid co-flow systems, that allows an independent selection of the generation frequency as well as the bubble volume. In order to impose the bubble detachment at the desired frequency, a forcing device, based on a loudspeaker, has been incorporated into the gas line of a co-flow system with a short gas injection needle. Therefore, the gas phase is forced by means of pressure modulation, inducing a periodic variation of the gas flow rate feeding the bubble. The resulting perturbed bubble generation process is experimentally characterized for different forcing frequencies. Firstly, natural bubbling regimes are established. Then, the system is forced, and synchronized bubble generation takes place at the selected frequency, provided that the amplitude of the pressure modulation is large enough. A detailed analysis of the

gas-liquid interface has allowed us to describe the perturbed bubble formation process and the different generation regimes that are established. Finally, the forced bubbling regime has been modelled by means of the inviscid form of the spherical Rayleigh-Plesset equation.

The second part of the dissertation is focused on the experimental analysis of the dynamics of a population of bubbles within a confined swarm of bubbles rising at high-Reynolds number driven by buoyancy. In order to investigate the evolution of the population of bubbles as they rise, systematic experiments have been performed for different injected air volume fractions, recording images at several heights. The downstream evolution of the bubble size distribution has been obtained after processing the images of the bubble swarm using a specially developed algorithm for bubble detection and classification. Major changes of the bubble size probability density function have been observed along the vertical direction, mainly caused by bubble coalescence. The mechanisms leading to bubble coalescence have been characterized by means of a statistical analysis of the bubble collisions detected in the images. Finally, additional experiments at high recording rates have been performed to determine the coalescence frequency as a function of the distribution of sizes. To that aim, a special bubble tracking method have been develop to detect every coalescence event.

Keywords: Bubble formation, bubbling forcing, co-flowing jets, coalescence, coalescence frequency, population balance equation.

Contents

List of Tables

List of Figures

CHAPTER
ONE

Introduction

1.1 Bubble formation

Bubble generation represents an important operation in the context of material, mineral, chemical and food industries, to name a few. Many emerging technologies, such as those related to biomedicine, require the use of monodisperse microbubbles (Rodríguez-Rodríguez *et al.*, 2015). In this context, bubbles can be used, for instance, as contrast agents in ultrasound techniques or for drug delivery (Ferrara *et al.*, 2007). These emerging applications are demanding new methods to generate bubbles at a given frequency and with a highly controllable size. Water aeration is another important application, characterized by the requirement of very large air throughputs (see Åmand *et al.*, 2013). The efficiency of these systems is controlled by the amount of gas dissolved in the liquid per unit of time, and the dissolution rate is proportional to the surface of the gas-liquid interface. A possible way to increase the interfacial area is to decrease the volume of the injected bubbles, what can in principle be achieved using porous plates or microfluidic devices. However, these systems are prone to clogging issues due to the smallness of the injection ports. Thus, developing robust devices able to inject very large air flow rates with small bubbles is still a challenging engineering problem.

The simplest method to produce bubbles is by releasing gas into a still liquid from a submerged orifice or nozzle. When the gas flow rate is sufficiently small, the bubble grows quasi-statically, and it detaches from the injector when the buoyancy force overtakes the surface tension force that holds the bubble to the injector wall (see for example Davidson & Schuler, 1960*a*,*b*; Longuet-Higgins *et al.*, 1991; Oğuz & Prosperetti, 1993; Bolaños-Jiménez *et al.*, 2008, among many others). Under these quasi-static conditions, the final bubble size is given by a balance between surface tension and buoyancy forces. The latter balance provides the simple estimation $V_F = \pi d/(\rho g)$ for the volume of the released bubble, usually called the *Fritz volume*, where d is the injector diameter. Unfortunately, this simple and robust method has several drawbacks. The first one is that, in order to generate small bubbles, an injector of small diameter is required, which is difficult to machine, and that may lead to clogging problems. Moreover, this method is restricted to values of the bubbling frequencies and injected gas flow rates. Indeed, if the gas flow rate is larger than a certain critical value, the distance between subsequently released bubbles decreases,

leading to their coalescence close to the injector. The latter phenomenon invalidates this method to generate controlled-size bubbles at high frequencies. Thus, additional forces that promote bubble detachment from the injector are required to generate monodisperse bubbles at high production rates.

Several techniques have been developed over the years to reduce the bubble size. One of them consists of generating turbulence in the continuous phase, so that the turbulent stresses acting on the dispersed phase cause its rupture. This technique produces a cascading process, inducing the subsequent breakup of the dispersed phase into pieces of smaller and smaller size, until a critical size is reached for which the turbulence stresses acting on the bubble surface become of the order of the confining surface tension stresses. Bubble breakup inside a fully developed turbulent water flow is a very complex phenomenon which can be described by statistical models, and has been studied by Kolmogorov (1949), Coulaloglou & Tavlarides (1977) and Martínez-Bazán *et al.* (1999*a*,*b*, 2010), among others (see the review by Lasheras *et al.*, 2002, for additional information). The main limitation of this technique is that, although it allows the generation of very small bubbles, their associated size distribution is unavoidably polydisperse.

To generate bubbles that are both small and monodiperse, many different methods have been proposed (Rodríguez-Rodríguez *et al.*, 2015). In particular, among the techniques where only mechanical forces are involved, the simplest ones are based on assisting the bubble breakup by imposing an outer liquid flow field. These methods can be classified depending on the relative direction between the outer liquid flow and that of the air stream (Rodríguez-Rodríguez *et al.*, 2015). Thus, *cross-flow* devices are those in which the air and liquid streams are perpendicularly oriented, while in the *co-flow* technique, the liquid is supplied as a parallel flow in the same direction as the air stream. In *flow-focusing* devices, the liquid flow is also fed parallel to the air flow, but in this case both the gas and the liquid streams are forced to flow through an orifice, leading to the formation of a highly-stretched two-phase meniscus (Gañán-Calvo & Gordillo, 2001; Gordillo *et al.*, 2004; Gañán-Calvo, 2004; Garstecki *et al.*, 2004). The latter method is widely used in microfluidics nowadays.

Among the above mentioned techniques, the simplest one is the parallel co-flow configuration. In this method, the gas flow is injected inside a laminar stream of liquid which flows in the same direction. This configuration allows the injection of much larger gas flow rates than in the case without outer co-flow, avoiding the irregular flow regimes and the bubble coalescence events that take place when the gas is injected into otherwise stagnant liquid. Maier (1927) was the first to investigate this technique, and documented the decrease of the bubble size when the gas flow was introduced through a cylindrical needle inside an outer laminar liquid co-flow. Later on, Chuang & Goldschmidt (1970) confirmed Maier's observations by performing systematic experiments, and Oğuz & Prosperetti (1993) also considered this configuration by means of theory and numerical simulations of the poten-

tial flow in the liquid, proposing a scaling law for the bubble size as a function of the co-flow velocity. More recently, Sevilla *et al.* (2005*a*) and Gordillo *et al.* (2007), performed a detailed experimental, theoretical and numerical study of a cylindrical co-flowing configuration in a high-Reynolds-number water jet discharging in a stagnant air atmosphere, characterizing the bubble formation and providing suitable scaling laws for the bubble size and the bubbling time. From these studies it is deduced that the most important practical limitation of the simple cylindrical co-flow technique is that the minimum size and the maximum production frequency of the emitted bubbles are determined by the injector diameter and the co-flow velocity. Thus, generating very small bubbles at very large frequencies, which is a typical requirement of many technological applications, implies the use of small injectors and large liquid co-flow velocities, what makes the system prone to clogging and energetically costly.

A planar co-flow configuration represents an alternative method to produce controlled-size bubbles (Bolaños-Jiménez *et al.*, 2011; Gutiérrez-Montes *et al.*, 2013, 2014; Bolaños-Jiménez *et al.*, 2016). In this geometry, which has been comparatively less studied than the cylindrical one, a planar air film discharges between two parallel water sheets. This technique has been shown to generate nearly monodisperse planar bubbles, yielding much larger injected gas flow rates compared with the cylindrical geometry. In particular, Bolaños-Jiménez *et al.* (2011) identified two different flow regimes: in the *jetting* regime the air sheet does not break near the injector tip, whereas in the *bubbling* regime, the air film periodically breaks into individual bubbles close to the injector. The transition between both regimes was characterized by means of experiments and numerical simulations as a function of the control parameters, namely, the Weber number, $We = \rho_w u_w^2 H_o/\sigma$, and the water-to-air velocity ratio, $\Lambda = u_w/u_a$, being ρ_w the water density, H_o the half-thickness of the air stream at the injector exit, and σ the surface tension coefficient. In the planar case, the surface tension force stabilizes the water-air-water sheet was obtained, in contrast with its effect on the cylindrical geometry, where it contributes to the destabilization of the air-water jet. In addition, the jetting-to-bubbling transition was explained as a transition from a convective to an absolute instability that requires a region of absolute instability with a size of the order of one local absolute wavelength evaluated at the outlet. A detailed numerical analysis of the bubbling regime was performed by Gutiérrez-Montes *et al.* (2013), who measured the frequency and size of the generated bubbles as a function of the control parameters. Furthermore, these authors provided a detailed description of the temporal evolution of the bubble shape and of the pressure field, aimed at unraveling the dominant physical mechanisms behind the bubbling process. The latter was described as a two-stage process: during the *neck formation* phase, which starts just after the collapse of the previous bubble, the air ligament remains attached to the outer side of the injector walls, so that the air flowing into the air ligament undergoes a sudden expansion from the inner to the outer thickness of the injector. This expansion

induces a negative gauge pressure in the air stream at the injector outlet that persists along the whole stage, causing the formation of an incipient neck at the inner air-water interface. During the rest of this stage, the neck moves downwards at the water velocity while it begins to accelerate towards the symmetry plane, causing a pressure drop in the air stream across the neck. Since the injected gas flow rate is constant, this makes the air pressure to increase at the injector outlet. This process continues, and during the *collapse stage* it self-accelerates. In this phase the high pressure rise induces the inflation of the air ligament, what causes the decrease of the gas flow rate that passes through the neck. Taking these facts into account, a scaling law was proposed for the characteristic bubbling time, $t_c \propto H_o/u_a\sqrt{(\rho_w/\rho)(h-1)/\left[We\beta(1-\beta)\right]}$, in good agreement with the experimental results, where $\beta = H_i/H_o$ is the inner-to-outer air thickness ratio. This scaling law takes the sudden expansion that the air stream suffers at the outlet as the dominant mechanism that causes the neck formation. In a follow-up study, these results were complemented with a simple theoretical model of the bubbling process based on the sudden expansion mechanism, that correctly reproduced the experimental results (Bolaños-Jiménez *et al.*, 2016). However, in the limit $\beta \to 1$, i.e. small injector wall thicknesses, the pressure drop induced by the sudden expansion was shown to play a negligible role (Gutiérrez-Montes *et al.*, 2014). In this case, the bubbling time is controlled by alternative mechanisms leading to negative gauge pressures in the air stream, such as the elongation of the growing bubble. The relative importance of the different mechanisms depends on the specific geometry, as well as on the characteristics on the injection system (Gutiérrez-Montes *et al.*, 2014), which determine the size and frequency of the generated bubbles. In particular, the spanwise length of the pancake-like shape bubbles is prescribed by the corresponding length of the air injection port. Therefore, as explained in the case of the cylindrical co-flow described in the previous paragraph, to improve the applicability and performance of the planar co-flow device, an additional forcing mechanism is required to reduce the size of the generated bubbles, as well as to increase their generation frequency.

A natural way to control the formation of bubbles at the frequencies and sizes required for practical applications is to apply an appropriate forcing protocol to the gas-liquid stream. Such techniques have been widely studied and successfully applied to the case of liquid jets injected into ambient gas, mostly motivated by the practical need to improve the design of inkjet printing devices (Lee, 1974; Basaran, 2002). Indeed, most of the experimental studies of the fundamentals and applications of the capillary instability of liquid jets in the Rayleigh regime made use of some kind of forcing device to select a certain frequency and a corresponding wavelength. These experimental studies where designed either to check the validity of the linear instability theory of Rayleigh (1878) (see Donnelly & Glaberson, 1966; González & García, 2009, among many others), or to control the size and frequency of the generated liquid drops (Kalaaji *et al.*, 2003), as well as the formation of satellite droplets (Goedde & Yuen, 1970; Rutland & Jameson, 1970;

Lafrance, 1975; Chaudhary & Maxworthy, 1980*b*). It is important to emphasize that, to generate a slender liquid jet inside a gas, the only condition that must be accomplished is that the inertia of the injected liquid stream is larger than the surface tension forces that tend to keep the liquid mass attached to the injector walls. In dimensionless terms, the latter condition means that the liquid Weber number is of order unity or larger, in which case the slender liquid jet is convectively unstable (Leib & Goldstein, 1986*b*,*a*). In contrast, when a gas stream is injected subsonically into an ambient liquid that is otherwise at rest, the resulting flow regime is absolutely unstable, since the inertia of the inner gas is always much smaller than that of the outer liquid. Consequently, in this *bubbling regime*, large individual bubbles are formed near the injector (Oğuz & Prosperetti, 1993). However, when an outer liquid co-flow is applied with a sufficiently large velocity, a transition to a jetting regime takes place, featuring a long gas jet that breaks-up into bubbles far from the nozzle (Sevilla *et al.*, 2005*b*). From a practical point of view, the main disadvantage of the jetting regime is that it requires a large liquid velocity, of the order of the gas velocity, and therefore it finds little use in applications. The fact that the flow is dominated by the inertia of the outer liquid has another important consequence for the physics of bubble generation. Indeed, the typical pressure fluctuations inside a forming bubble that is attached to the injector scale with the outer liquid density. These pressure fluctuations may well be of the order of the pressure drop along the gas feeding line, which scale with the gas density, the gas viscosity, and the geometry of the injection line. In these common cases, the injected gas flow rate is time dependent due to the forcing of the pressure disturbances at the injector outlet (Gordillo *et al.*, 2007). Moreover, for modeling purposes, the unsteady gas flow in the feeding line is unknown *a priori*, and must be included as an additional unknown together with a proper model to account for the hydraulic resistance associated with the gas feeding system (Oğuz & Prosperetti, 1993; Gordillo *et al.*, 2007). From these considerations, it is clear that the design of forcing strategies for the controlled formation of bubbles is much more involved than in the case of liquid jets. Indeed, although there are recent studies dealing with the forced breakup of liquid-liquid streams in co-flow configurations (Sauret & Cheung Shum, 2012; Zhu *et al.*, 2016*a*) and in flow-focusing systems (Zhu *et al.*, 2016*b*; Mu *et al.*, 2018; Yang *et al.*, 2019), to the best of the author's knowledge the first systematic studies of hydrodynamically stimulated bubble formation systems in pure co-flow configurations have been performed in the context of the present PhD dissertation.

1.2 Bubble coalescence

Coalescence can be seen as a *three-steps process* involving three different kinds of fluid mechanics problems (Prince & Blanch, 1990; Chesters, 1991). The first step consists in the approach of the bubbles that get closer due to their relative motion. This step is

controlled by the *external* flow that may lead to contact. Once bubbles are in contact, in order for coalescence to happen, it is necessary that the thin liquid film between the bubbles be drained. The *internal* problem to be solved at this second stage is that of a thin liquid film drainage. The last stage initiates when the film has become thin enough so that inter-molecular forces, such as van der Waals ones for pure fluids, become predominant and generate the breakup of this liquid film and the coalescence of the bubbles. The present work focuses on the analysis of the hydrodynamics controlling the first stage in a high-Reynolds number confined bubble swarm.

Basic formalism for coalescence modeling and elements for closure laws are now introduced in order to set the framework of the present investigation. Let's consider a cloud of bubbles of different size moving at different velocities, defining the probability density $p(\mathbf{x}, t, v, \mathbf{u})$ as the probability of finding in the spatial range between $\mathbf{x}$ y $\mathbf{x} + \mathrm{d}\mathbf{x}$ at a given time t bubbles whose volume falls between v y $v + \mathrm{d}v$ and whose velocity is between $\mathbf{u}$ y $\mathbf{u} + \mathrm{d}\mathbf{u}$. The spatio-temporal evolution of this probability density can be described by the Boltzmann equation (Williams, 1985),

$$\frac{\partial p}{\partial t} + \nabla \cdot (\mathbf{u}\, p) + \nabla_{\mathbf{u}} \cdot (\mathbf{F}\, p) = -\frac{\partial (\mathcal{R}\, p)}{\partial v} + \dot{Q}'_{\mathrm{b}} + \dot{Q}'_{\mathrm{d}} + \Gamma \tag{1.1}$$

where $\mathbf{F}$ is the force per unit mass on the bubble, $\dot{Q}'_{\mathrm{b}}$ and $\dot{Q}_{\mathrm{d}}$ are the birth and death rates of change of the bubbles due to breakup and coalescence, $\mathcal{R}$ is the rate of change of the volume v of a bubble due to evaporation, condensation or dissolution, and Γ represents the rate of change of the distribution function, p, caused by collisions with other bubbles which do not result in coalescence.

In order to describe the sizes of a population of bubbles, it is worth integrating equation (1.1) over the entire velocity space, considering $n(v, \mathbf{x}, t) = \int p\, d\mathbf{u}$ the probability density function in number corresponding to the relative number of inclusions with a volume in between v and $v + dv$ as compared to the total number of bubbles (Lasheras *et al.*, 2002),

$$\frac{\partial n}{\partial t} + \nabla \cdot (\bar{\mathbf{u}}\, n) + \frac{\partial (\mathcal{R}\, n)}{\partial v} = \dot{Q}_b + \dot{Q}_d \tag{1.2}$$

where $\bar{\mathbf{u}}$ is the mean velocity of bubbles of volume v at a location $\mathbf{x}$ at time t, $\dot{Q}_{\mathrm{b}} = \int \dot{Q}'_{\mathrm{b}}\, \mathrm{d}\mathbf{u}$, and $\dot{Q}_{\mathrm{d}} = \int \dot{Q}'_{\mathrm{d}}\, \mathrm{d}\mathbf{u}$. In the case of bubbles in liquid flows of interest in the present work, dissolution effects can be neglected ($\mathcal{R} = 0$) since the dissolution times are much larger the characteristics residence time of bubbles. Equation (1.2) may depend on space and time if the problem is non homogeneous and unsteady. A dependence on the velocities of the bubbles can also be introduced if, for a given size, possible velocities are distributed in a large range where coalescence and breakup dominant mechanisms may vary. For simpler presentation we do not incorporate this effect in the following equations. Thus, the equation that determines the transport and the evolution of $n(v, \mathbf{x}, t)$ is the Liouville-Boltzmann's

equation. It is a generalization of Smoluchowski's equation used for coagulation and it is usually called the Population Balance Equation (PBE) (Williams, 1985). When neglecting changes of volume due to thermodynamical phase change, taking into account breakup as well as coalescence, this equation writes (Coulaloglou & Tavlarides, 1977; Yao & Morel, 2004; Marchisio & Fox, 2013; Martínez-Bazán, 1999)

$$\frac{\partial n(v,\mathbf{x},t)}{\partial t} + \nabla \cdot \left[n(v,\mathbf{x},t)\, \bar{\mathbf{u}}(v,\mathbf{x},t) \right] = \dot{Q}_c + \dot{Q}_b \tag{1.3}$$

where $\dot{Q}_c$ is the sink or source term due to coalescence and $\dot{Q}_b$ that due to breakup. Moments of order 0 and 1 of this probability density function are respectively the total number of inclusions per unit volume, $N(\mathbf{x},t)$, whatever their sizes, and the volume fraction of the dispersed phase α (Kocamustafaogullari & Ishii, 1995),

$$m_0(\mathbf{x},t) = \int_0^\infty n(v,\mathbf{x},t)\, \mathrm{d}v = N, \tag{1.4}$$

$$m_1(\mathbf{x},t) = \int_0^\infty v\, n(v,\mathbf{x},t)\, \mathrm{d}v = \alpha. \tag{1.5}$$

The coalescence and breakup rates read

$$\begin{aligned} \dot{Q}_c =& \frac{1}{2} \int_0^v \lambda_c(v-v',v')\, h_c(v-v',v')\, n(v-v',\mathbf{x},t)\, n(v',\mathbf{x},t)\, \mathrm{d}v' \\ & - \int_0^\infty \lambda_c(v,v')\, h_c(v,v')\, n(v,\mathbf{x},t)\, n(v',\mathbf{x},t)\, \mathrm{d}v' \end{aligned} \tag{1.6}$$

and

$$\dot{Q}_b = \int_v^\infty f(v',v)\, m(v')\, g_b(v')\, n(v',\mathbf{x},t)\, \mathrm{d}v' - g_b(v)\, n(v,\mathbf{x},t), \tag{1.7}$$

where $h_c(v,v')$ is the collision frequency between bubbles of volumes v and v'; $\lambda_c(v,v')$ is the collision efficiency between inclusions of volumes v and v'; $g_b(v)$ is the breakup or fragmentation frequency of bubbles of volume v; $m(v)$ the number of bubbles resulting from the fragmentation of inclusions of size v; and $f(v',v)$ the number probability density of daughter bubbles resulting from the fragmentation of a mother bubble of volume v'. In equation (1.6), the first integral term of the r.h.s. is a source term and the second one a sink term, both due to coalescence. Similarly, in equation (1.7) source and sink terms due to fragmentation participate to the PBE. Several closure laws and models for each of these terms are proposed in literature. Their validity is most often limited to given hydrodynamical regimes of breakup and coalescence enforced by turbulent agitation or by mean shear flow. Sometimes they also include the influence of physico-chemical properties of the liquid or of the interface. Large amount of information on the adopted models can be found in references such as Coulaloglou & Tavlarides (1977); Prince & Blanch (1990);

Chesters (1991); Martínez-Bazán *et al.* (2010) or in literature reviews such as Kolev (1993); Lasheras *et al.* (2002); Liao & Lucas (2009, 2010); Marchisio & Fox (2013).

The second Part of this Thesis is focused on the coalescence processes of bubbles leaving bubble breakage out of the scope of this work. Thus, main arguments for coalescence modeling in three-dimensional flows are recalled to figure out our guidelines. Models for coalescence are generally based on the idea that coalescence takes place in a swarm of bubbles if there is a high enough frequency of externally-driven collisions between bubbles and if the duration of the contact between the bubbles, t_{ext}, is greater than the duration necessary for the drainage of the internal thin liquid film, t_d. It is possible to find in literature relations for this frequency of collision and for the characteristic times depending on the way bubbles approach each other (see Prince & Blanch, 1990; Chesters, 1991; Tsouris & Tavlarides, 1994; Hibiki & Ishii, 2000; Kamp *et al.*, 2001; Liao & Lucas, 2010, among many others). Thus, bubble coalescence is commonly modeled as the product between a collision frequency times a coalescence efficiency (Martínez-Bazán, 1999),

$$g_c(v) = (\text{bubble} - \text{bubble collision frequency}) \times (\text{coalescence efficiency}), \tag{1.8}$$

The collision rate between bubbles of volume v_i with bubbles of volume v_j is given by Coulaloglou & Tavlarides (1977)

$$h_c(v_i, v_j)\, n(v_i) n(v_j) = \left(\frac{9\pi}{2}\right)^{1/3} \left(v_i^{2/3} + v_j^{2/3}\right) \left(u_{v_i}^2 + u_{v_j}^2\right)^{1/2} n(v_i) n(v_j), \tag{1.9}$$

where u_{v_i} and $n(v_i)$ are the velocity and the number of bubbles of volume v_i. As mentioned above, coalescence takes place if the residence time, t_{ext}, is longer than the coalescence time, t_d, estimating the coalescence efficiency as,

$$\lambda_c(v_i, v_j) \approx \exp\left[-\frac{t_d}{t_{ext}}\right]. \tag{1.10}$$

Concerning collision, it can be controlled by various generic mechanisms leading to contact (see Kocamustafaogullari & Ishii, 1995, for instance). They involve velocity difference between the considered bubbles that can come from: (i) random fluctuations of bubble velocities, generated by the agitation of the carrier fluid; (ii) size dependent rise velocity differences, when the considered bubbles have different sizes and adopt contrasted terminal velocities; (iii) wake entrainment, when a trailing bubble is accelerated in the wake of a leading one; (iv) shear layer velocity induced differences, when bubbles are driven by a sheared mean flow. In our case, turbulence cannot develop due to confinement, as revealed in a homogeneous swarm studied by Bouche *et al.* (2014), but the random agitation of the liquid may lead bubbles to collide and the other mechanisms may also be present. It is therefore important to primarily detect if one of them is dominant or if they co-exist.

Although direct measurements of bubble coalescence are shown in this dissertation, further analysis devoted to collision frequency and efficiency are planned later in the

present investigation. They should lead to original closure laws due to confinement effects. In fact, in first-level approaches, the collision frequency, h_c, can be considered as modeled in a simplified way. In three-dimensional flows, assuming that bubbles are and stay spherical during collision, that they have the same diameter D, and that they follow the relative motion imposed by the external flow without developing hydrodynamical interactions, it is possible to find the collision frequency from an effective volume where contact can take place that is crossed by the relative approach motion. For a swarm including n bubbles per unit volume it is thus possible to propose (Chesters, 1991),

$$h_c n^2 = k U_r D^2 n^2, \tag{1.11}$$

where h_c is per unit time, per bubble number and per unit volume, k is a prefactor of order one, and U_r is the characteristic velocity of the motion of approach when bubbles are separated by a distance equal to the diameter D. The challenge will be to estimate relative velocities U_r involved in collisions depending on the dominant mechanisms. For turbulence-induced collisions, one may consider that (Prince & Blanch, 1990),

$$U_r \approx (\varepsilon D)^{1/3} \tag{1.12}$$

or (Friedlander, 1977; Kocamustafaogullari & Ishii, 1995),

$$U_r \approx (\varepsilon/\nu)^{1/2} D, \tag{1.13}$$

depending on the size of the bubbles, where ε is the turbulent kinetic energy dissipation rate, ν the kinematic viscosity of the liquid. Relation (1.12) is used for bubbles whose size is in the inertial range of turbulence, while relation (1.13) is applied for bubbles with diameters comparable to the smallest scales of turbulence.

In a flow with a mean shear rate $\dot{\gamma}$ the relative velocity during approach U_r may write (Friedlander, 1977),

$$U_r \approx \dot{\gamma} D, \tag{1.14}$$

and when buoyancy effects are dominant (Clift *et al.*, 1978; Wang *et al.*, 2005),

$$U_r \approx \left| U_{\infty 1} - U_{\infty 2} \right|, \tag{1.15}$$

where $U_{\infty i}$ with $i \in 1, 2$ are the terminal velocities of both bubbles.

Finally, when bubbles enter the wake region of a leading one, U_r is related to the liquid velocity behind the leading bubble. Although several models have been proposed (see Kalkach-Navarro *et al.*, 1994; Wu *et al.*, 1998; Colella *et al.*, 1999; Hibiki & Ishii, 2000; Wang *et al.*, 2005, among others), this mechanism appears as the most ambiguous one, being each proposed method quite different from the others. Thus, further investigations results indispensable.

Duration of contact between bubbles, t_{ext}, also varies depending on the way they approach. The models that are reported hereafter are written in a very simple way in order to give a first approach to the reader. Their domain of validity is thus limited and their extend requires deep investigations, in particular for two-dimensional flows where they have never been investigated. One can find, for example in Liao & Lucas (2010), different models reported in recent researches for the various ways of approach, but which generic character will have to be checked. We can, for example, consider that in a turbulent flow or in a mean shear flow, duration of contact t_{ext} imposed by the *external* flow is,

$$t_{ext} \approx \varepsilon^{-1/3} D^{2/3} \tag{1.16}$$

or, depending on the size of the bubbles with respect to turbulent structures,

$$t_{ext} \approx (\varepsilon/\nu)^{-1/2} \tag{1.17}$$

or

$$t_{ext} \approx \dot{\gamma}^{-1}. \tag{1.18}$$

Duration of film drainage t_d has been most often determined by theoretical or numerical solution of the thin film flow considered in the lubrication approximation, drainage strongly depending on the boundary condition applied at the interfaces and on the way the relative motion of the interfaces is imposed (models consider either approaches at constant relative velocity or at constant imposed force). In three-dimensional flows, bubble interfaces have been represented as spherical or deformable during drainage, and a slip or no slip boundary condition was applied to represent either a clean mobile interface or a rigid one. There is thus a great variety of possible flow configurations, and also a great impact of the chemico-physical properties of the liquid on this characteristic time that contributes to the efficiency of coalescence. Chesters & Hofman (1982) have nevertheless shown that liquid film drainage between two bubbles with mobile interfaces in inertial regime develops a strongly localized dimple that amplifies so rapidly that the liquid film does not become thinner as a whole but instead will be broken due to the dimple development. Growth of dimple is so rapid, that determination of the time of breakup does no longer depend on intermolecular forces and t_d is determined by the time at which the dimple appears, t_{dimple}. This time writes,

$$t_d \approx \rho_l U_r D^2/(32\sigma), \tag{1.19}$$

where ρ_l is the liquid density and σ is the surface tension (Chesters & Hofman, 1982; Chesters, 1991).

In the present research, we did not investigate this *internal* stage of the coalescence process in the confined flow and cannot provide an estimation of t_d in our experimental

conditions. This would be another part of the work to be performed to analyze the impact of the confinement on the drainage of the film. The absence of knowledge about t_d is however compensated by a possible direct measurement of the coalescence efficiency in the set-up.

1.3 Outline of the dissertation

The present dissertation is organized in two different parts. On the one hand, Part I is focused on the controlled formation of bubbles. In particular, the forced breakup of planar water-air-water streams by harmonic stimulation of the liquid flow rate is presented in Chapter 2, while Chapter 3 is devoted to report the performance of a forcing system for cylindrical co-flowing air-water jets by periodic modulation of the air feeding pressure. On the other hand, Part II focuses on the dynamics of a two-dimensional bubble swarm. Therefore, Chapter 4 analyzes the downstream evolution of the population of bubbles within a confined swarm of bubbles rising at high-Reynolds numbers, describing the coalescence process of bubbles which drives the changes of the size distribution. Finally, in Chapter 5 the main conclusions of this dissertation are summarized and some ideas on future perspectives are outlined.

Part I

Controlled formation of bubbles

CHAPTER
TWO

Controlled formation of bubbles in a planar co-flow configuration

2.1 Introduction

Many techniques have been developed in the last decades to massively generate small monodiperse bubbles. One of the most extended methods is the co-flow configuration, in which the gas flow discharges inside a laminar liquid stream that flows in the same direction. The cylindrical co-flow geometry has been extensively studied (Chuang & Goldschmidt, 1970; Oğuz & Prosperetti, 1993; Gordillo *et al.*, 2001; Sevilla *et al.*, 2002, 2005*a*; Gordillo *et al.*, 2007) and is widely used nowadays, playing a relevant role in microfluidics (Stone *et al.*, 2004; Gañán-Calvo, 2004; Gordillo *et al.*, 2004). The formation of bubbles in a planar co-flow configuration has also been studied (Bolaños-Jiménez *et al.*, 2011; Gutiérrez-Montes *et al.*, 2013, 2014; Bolaños-Jiménez *et al.*, 2016). As a result, it has been found that the transverse pressure gradient established at the injector exit is the mechanism leading to the bubble formation; a scenario similar to that reported by Gañán-Calvo (2004) in a cylindrical flow focusing configuration. The results of these works, devoted to the experimental, theoretical and numerical study of the bubble formation process, reveal that the periodic bubbling regime that is naturally established in the planar case produces bubbles of much larger volume than in the cylindrical geometry. Indeed, in the planar case the quasi-two-dimensional dynamics of the flow provides bubbles of pancake-like shape whose spanwise length is determined by the corresponding dimension of the air nozzle. Therefore, finding ways to decrease the size of the bubbles and increase their formation frequency is crucial for the practical application of the planar co-flow device.

Several forcing methods have been investigated in the past to control the formation of bubbles by actuating on the gas stream. For instance, the use of pulsed acoustic pressure waves in the gas phase (Shirota *et al.*, 2008; Abe & Sanada, 2015; Makuta *et al.*, 2013) or the direct actuation over the feeding gas stream (Ohl, 2001). The use of mechanical vibrations of the injector has also been explored (Vejrazka *et al.*, 2008). In contrast, only a few studies can be found on the forcing of the liquid phase, mainly in the field of bubble columns to improve their performance by low-frequency pulsations of the liquid (Krishna

& Ellenberger, 2003), and in microbubble generation by applying an external ultrasonic field to the liquid phase (Makuta *et al.*, 2006).

The configuration studied in the present work represents a promising route to increase the efficiency of industrial-scale water aeration operations. The method proposed consists of forcing the liquid flow rate by harmonic stimulation. Although, to the best of our knowledge, this technique has not been explored before to control the bubble formation process in co-flow devices, it is a widespread technique to control the breakup of cylindrical liquid jets (Chaudhary & Maxworthy, 1980*a*; Meier *et al.*, 1992; Eggers & Villermaux, 2008; Guerrero *et al.*, 2012) and sheets (Lozano *et al.*, 1998; Mehring & Sirignano, 2001; Sirignano & Mehring, 2000). Therefore, we have developed a system to control the generation of bubbles in a planar water-air-water sheet by harmonically modulating the flow rate of the water stream, although it could easily be implemented in other types of configurations.

The Chapter is organized as follows. Section 2.2 is devoted to the description of both the experimental and numerical work: the experimental facility and techniques are detailed in Sect. 2.2.1, while the numerical method and procedure are described in Sect. 2.2.2. Next, in Section 2.3, the experimental results are presented, where the effectiveness of the forcing is first characterized in Sect. 2.3.1, followed by Sect. 2.3.2, where the conditions for effective stimulation are characterized through the critical forcing amplitude and the length of the intact air ligament that remains attached to the injector once a bubble is formed. Next, in Section 2.4, the forcing effect is described by means of a theoretical one-dimensional model. Finally, Section 2.5 is devoted to conclusions.

2.2 Experimental and numerical methods

2.2.1 Experimental set-up

The experimental facility described by Bolaños-Jiménez *et al.* (2011) and Gutiérrez-Montes *et al.* (2013) has been used in the present work to create a planar air sheet of outer half thickness $H_o = 0.455$ mm surrounded by a pair of symmetrical parallel water streams that discharge into a stagnant air atmosphere, with a thickness $h_0 = H_w - H_o = 1.945$ mm, being $H_w = 2.4$ mm the distance from the outer interface to the central plane (figure 2.1a). The set-up basically consists of two parallel thin walls placed at a distance $2\,H_i \simeq 0.47$ mm that confine the air stream, and two exterior nozzle-shaped walls for the co-flowing water streams separated by a distance $2\,H_w$ at the outlet. The spanwise length of the injector, perpendicular to the plane sketched in figure 2.1(a), is $b = 41.75$ mm, two orders of magnitude larger than the air sheet thickness, providing a quasi-two-dimensional configuration. For the purposes of the present work, the facility was modified to incorporate a forcing system, sketched in figure 2.1(b). The design of the inner channel of the whole nozzle assures that, at the exit of the injector, the velocity profile is fully developed in the air stream and nearly uniform in the water one (figure 2.1a). The pressure

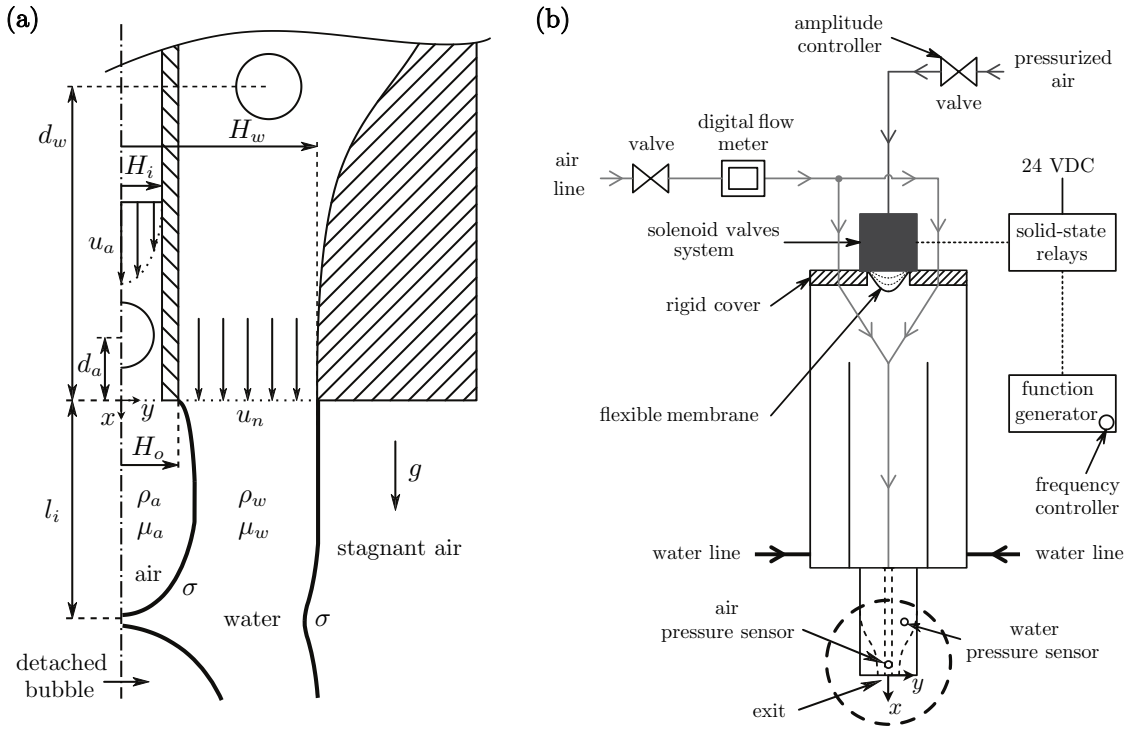

Figure 2.1: (a) Sketch of the air-water co-flowing streams at the exit of the nozzle in the side plane (x, y), showing the natural bubble formation and indicating the main geometrical characteristics, the dimensional parameters of the unforced problem, and the position of both the air and water gauge pressure sensors. (b) General sketch of the experimental facility, including the forcing device. The region highlighted with a dashed circle corresponds to the exit of the nozzle, sketched in (a).

drop along the air channel was always much larger than the pressure fluctuations inside the forming bubble, ensuring thus a constant air flow supply (Gordillo *et al.*, 2007). The water was supplied to both outer nozzles from a feeding vessel placed above them, minimizing the transverse velocity components. Both the feeding air and water flow rates, Q_a and Q_n, were controlled through precision valves and measured with digital mass flow meters. The average velocities at the nozzle exit, calculated by dividing the flow rate by the corresponding cross section, were varied from $u_a \simeq 13$ m/s to $u_a \simeq 19$ m/s and $u_n \simeq 1.5$ m/s to $u_n \simeq 2.5$ m/s, for the air and the water streams respectively. The remaining parameters involved in the unforced problem (figure 2.1a) are the air-water surface tension coefficient, σ, the water and air viscosities, μ_w and μ_a, the water and air densities, ρ_w and ρ_a, and the gravitational acceleration, g. Viscous effects can be neglected in both the water and air flows downstream of the nozzle outlet, since the corresponding Reynolds number ranges are $3000 \lesssim Re_w = \rho_w u_n h_0/\mu_w \lesssim 5000$, and $300 \lesssim Re_a = \rho_a u_a H_o/\mu_a \lesssim 500$ (Bolaños-Jiménez *et al.*, 2011; Gutiérrez-Montes *et al.*, 2013). In addition, the gas-to-liquid density ratio was constant in all experiments, $S = \rho_a/\rho_w \simeq 0.0012$. Finally, the Froude number based on the length of the intact ligament, l_i, which is the lump of air

that remains attached to the nozzle exit after the pinch-off of a bubble (see figure 2.1a), is $Fr = u_n^2/(gl_i) \gg 1$, so that the effect of gravity can be neglected. Therefore, there are only two dimensionless parameters governing the unforced bubbling configuration, namely the Weber number, $We = \rho_w u_n^2 H_o/\sigma$, and the water-to-air velocity ratio, $\Lambda = u_n/u_a$, that were varied in this work within the ranges $14 \lesssim We \lesssim 40$ and $0.08 \lesssim \Lambda \lesssim 0.16$. The bubbling regime can be experimentally induced by properly setting the values of We and Λ, as described by Bolaños-Jiménez *et al.* (2011). According to the range of values of We and Λ considered in the present work, the obtained natural bubble formation frequencies varied from $f_n \simeq 100$ Hz to $f_n \simeq 200$ Hz.

To register the pressure variations inside the air and water streams, two gauge pressure sensors were placed at distances $d_a = 3$ mm and $d_w = 65$ mm upstream from the nozzle exit (figure 2.1a). The temporal evolution of the gauge pressure registered inside the air channel, $p_a(t)$, provides a convenient description of a bubble formation event (Gutiérrez-Montes *et al.*, 2013), while the water gauge pressure, $p(t)$, allows to characterize the forcing process of the water flow. The forcing device is placed on top of the feeding water vessel (figure 2.1b), and its performance is based on the deformation of a flexible silicone membrane that induces a variation of the water flow rate. To induce an oscillatory deformation of the membrane, its upper side is pushed and pulled through the alternative injection and suction of pressurized air, controlled by a system of high-speed pneumatic solenoid valves (MATRIX model number 821NC2/2). These valves are driven by electric on/off signals (24-0 VDC) from solid-state relays which are excited by a square signal from a tunable-frequency function generator (YOKOGAWA model number FG110), that allows to select the forcing frequency, f_f. The forcing amplitude is set by a precision valve that controls the pressurized air flow rate feeding the stimulation system (figure 2.1b).

The forcing device induces a modulation of the water flow rate. Thus, to characterize the velocity modulation at the exit of the injector it is necessary to translate the pressure signals, recorded by the pressure sensor, into velocity. The liquid volume conservation equation requires the deformations of the membrane to instantaneously induce a variation of the water flow rate at the exit of the nozzle, $Q(t)$, that differs from its unforced value, Q_n. Hence, the disturbance results in a modulation of the water flow rate at the exit,

$$Q(t) = Q_n + Q'(t), \tag{2.1}$$

where $Q'(t) \ll Q_n$ represents the flow rate disturbance, which can be obtained from the signal registered by the water pressure sensor, $p(d_w, t) = p_n(d_w) + p'(d_w, t)$. Here, p_n represents the unforced gauge pressure and $p'(d_w, t)$ the pressure disturbance, which can be approximated by a harmonic signal, as shown in figure 2.2(a, c)

$$p'(d_w, t) = \zeta \cos(\omega t + \varphi), \tag{2.2}$$

where ζ is the amplitude of the water pressure disturbance, $\omega = 2\pi f_f$ the angular frequency, and φ the phase with respect to the pinch-off event associated with the formation of the

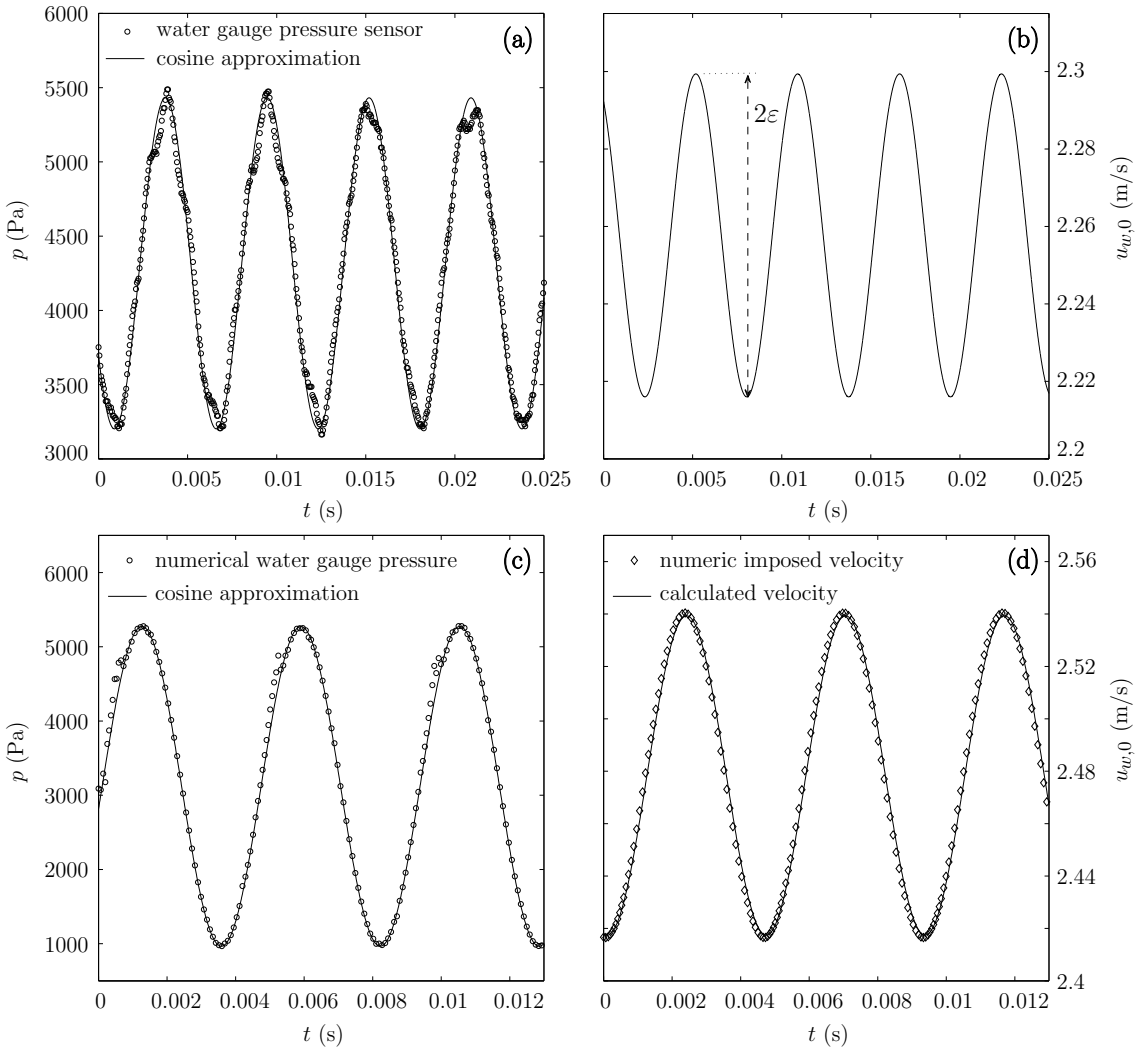

Figure 2.2: Time series of water pressure and velocity extracted from the experiments (a, b, corresponding to $We = 32.2$, $\Lambda = 0.152$, $f_f = 175$ Hz and $\epsilon = 0.018$), and the simulations (c, d, for $We = 38.8$ and $\Lambda = 0.147$, $f_f = 216$ Hz and $\epsilon = 0.025$). (a) Experimental gauge pressure together with a cosine fit. (b) Velocity at the nozzle exit obtained with Eq. (2.5), from which ε is obtained. (c) Numerical gauge pressure at a distance from the nozzle exit equal to d_w together with a cosine fit. (d) Comparison of the imposed velocity and the calculated one using Eq. (2.5).

previous bubble. It can be seen in figure 2.2(a) that the experimental water pressure signal can be well described by Eq. (2.2). Moreover, since $Re_w \gg 1$, the inviscid momentum equation for the water in the streamwise direction inside the nozzle can be expressed as

$$\frac{\partial u_w}{\partial t} + u_w \frac{\partial u_w}{\partial x} = -\frac{1}{\rho_w}\frac{\partial p}{\partial x} + g, \tag{2.3}$$

being u_w the streamwise component of the water velocity. According to Eq. (2.1), if Eq. (2.3) is linearized and taking into account that the lowest value of $f_f\, L$ in the experiments performed here was much larger than u_n, being $(f_f\, L)_{min} = 11.5\, u_n \gg u_n$, we obtain

$$\frac{1}{A(x)}\frac{dQ'(t)}{dt} = -\frac{1}{\rho_w}\frac{\partial p'}{\partial x}, \tag{2.4}$$

where $A(x)$ is the cross section of the water channel and $L = 150$ mm is the length of the water nozzle. Integrating Eq. (2.4) between d_w and the exit of the nozzle, $x_0(x = 0)$, where the pressure inside the water sheets is the atmospheric one (Bolaños-Jiménez *et al.*, 2011), the modulation of the water flow rate and, thus, of the water velocity, $u'_w(t)$, can be obtained as,

$$Q'(t) = \frac{1}{\rho_w K}\int_{t_0}^{t} p'(d_w, t)dt \rightarrow u'_w(t) = Q'(t)/A(x_0), \tag{2.5}$$

where $K = \int_{d_w}^{x_0}[1/A(x)]dx \simeq 300$ m^{-1} is a constant which depends on the water channel geometry. Equation (2.5) has been integrated with the initial condition $Q'(t_0) = 0$, being t_0, according to Eq. (2.2), the time in which the disturbance $p'(d_w, t_0)$ reaches a local maximum. Therefore, the forcing process can be described as a modulation of the water velocity at the nozzle exit of the form $u_{w,0}(x = 0, t) = u_n + u'_w(t)$. Considering that $p'(d_w, t)$ in Eq. (2.5) is given by Eq. (2.2), the water velocity at the outlet can be expressed as

$$u_{w,0}(t) = u_n + \varepsilon \sin(\omega t + \varphi), \tag{2.6}$$

where $\varepsilon = \zeta/[\rho_w \omega K A(x_0)]$ is the amplitude of the water velocity fluctuations as shown in figure 2.2(b), which depends on the amplitude and the frequency of the induced pressure disturbances, ζ and ω. Thus, the value of ε, together with the forcing frequency, $f_f = \omega/(2\pi)$, constitute the two parameters that define the stimulation of the water flow. In dimensionless terms, the forcing process can be characterized by the Strouhal number, defined as $St = f_f h_0/u_n$, and the dimensionless velocity amplitude, $\epsilon = \varepsilon/u_n$.

The experiments were conducted by firstly setting an unforced bubbling regime, identified by a given value of both u_n (or We) and u_a (or Λ), with an associated natural bubble formation frequency, f_n. After a periodic bubble generation process was achieved, a forcing frequency, $f_f > f_n$, was imposed with a function generator, and the forcing amplitude was smoothly and monotonically increased. In addition, to investigate the existence of hysteresis, the amplitude was also decreased in the same way, but no hysteresis was detected. The forcing frequency was varied from $f_f \simeq 150$ Hz to $f_f \simeq 250$ Hz, being the latter value given by the maximum air flow rate that the solenoid valve system was able to supply. Finally, the spanwise (x, z) view of the sheets was recorded using a Photron high-speed camera at frame rates between 15 000 s^{-1} and 20 000 s^{-1}, with an acquisition box of 256 $\times$ 304 pixels. A spatial resolution of around 100 μm/pixel was achieved using a Sigma 105 mm macrolens and backlighting technique. The high-speed movies were synchronized with the readings of the two gauge pressure sensors through a data logger system. Figure 2.3 shows several snapshots extracted from the high-speed movies, corresponding to a natural

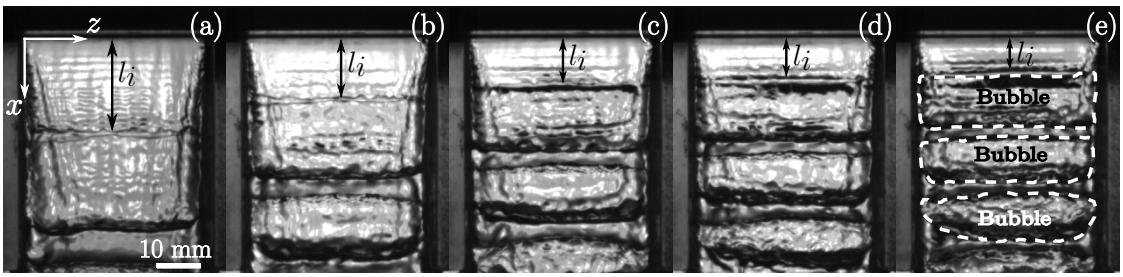

Figure 2.3: Experimental images in the spanwise (x, z) plane corresponding to $u_n = 1.8$ m/s ($We = 21.6$) and $u_a = 13.9$ m/s ($\Lambda = 0.133$), (a) in the natural bubbling regime with $f_n = 118$ Hz, and $(b$-$e)$ for different cases of effective forcing with $\epsilon = \epsilon_c$ at (b) $f_f = 150$ Hz, (c) $f_f = 175$ Hz, (d) $f_f = 200$ Hz and (e) $f_f = 225$ Hz. In each panel l_i indicates the associated intact ligament, which decreases as f_f increases. As example, the individual formed bubbles are highlighted in panel (e).

bubbling regime (figure 2.3a) and different forced cases (figure 2.3b-e) at $We = 21.6$ and $\Lambda = 0.133$. All the images correspond to the pinch-off time, at which the upper bubble detaches from the injector at a distance l_i indicated in the images. The panels show the periodic formation of nearly monodisperse, elongated bubbles in the spanwise plane (x, z), as highlighted in figure 2.3(e). It is worth noticing that the intact length, l_i, and the bubble size decrease as the forcing frequency increases, as will be described in detail later on.

2.2.2 Numerical simulations

In addition to the experiments described in Sect. 2.2.1, two-dimensional, planar numerical simulations of the bubbling process were also conducted using the numerical models already documented and validated by Gutiérrez-Montes *et al.* (2013, 2014). The main purpose of these simulations was to describe the time evolution of the interface in the (x, y) plane, since this view was not available in the experiments but is crucial to investigate the physical mechanisms governing the bubble generation process. The simulations were performed with the open source code OpenFOAM (http://www.openfoam.com), through the solver *interFOAM*, which implements a Volume of Fluid (VOF) interface-capturing technique assuming an unsteady, incompressible, laminar flow, as described by Gutiérrez-Montes *et al.* (2013, 2014). A detailed description of the governing equations and numerical techniques can be found in Rusche (2003); Berberović *et al.* (2009); Gutiérrez-Montes *et al.* (2013), among others, and the reader is referred to them for further information.

The computational domain includes the whole 150 mm long injection nozzle, as well as a 100 mm long region of the discharging atmosphere. No slip conditions were imposed at the walls, atmospheric pressure at the air boundaries and the flow velocity at the inlets. In the case at hand, to simulate the forcing process in accordance with the experimental conditions, the sinusoidal water velocity given by Eq. (2.6) was set as velocity inlet up-

stream of the nozzle exit, as illustrated in figure 2.2(d). Finally, to validate the procedure described by Eqs. (2.2-2.6) to determine the experimental water velocity signal from the water pressure measurements, the numerical pressure signal, which can be also fitted to Eq. (2.2) (figure 2.2c), was used in Eq. (2.5) to calculate the water velocity. As can be seen in figure 2.2(d), a very good agreement was achieved between the time evolution of the velocity obtained from the pressure signal and the one provided by the simulations, validating the experimental procedure followed to obtain the water velocity signal.

2.3 Experimental characterization of the forcing process

In the present section, the experimental results on the forced planar bubbling regime are described. The performance of the forcing process is first discussed and characterized, followed by a detailed description of the main physical mechanisms involved.

2.3.1 Performance of the forcing process

To explore the conditions under which the bubbling regime is controlled by the imposed disturbance, the capability of the forcing system was assessed by analyzing both the high-speed movies of the bubbling process (figure 2.3) and the time evolution of the air pressure at the injector outlet (figure 2.4). In the unforced case, illustrated in figure 2.3(a), the natural bubbling frequency, f_n, was obtained from images recorded with a high-speed camera, by processing the temporal evolution of the normalized mean grey level (NGL) along a spanwise line placed at a given downwards position, as described by Gutiérrez-Montes *et al.* (2014). Indeed, when the process was periodic, the time series of the normalized mean grey level of a spanwise monitoring line exhibited an associated power spectral density (PSD) with a clear peak at f_n.

However, in the forced cases, due to optical uncertainties, the measurements of the air pressure, complemented by the high-speed recordings, were used to obtain the bubbling frequencies. Note that the air pressure registered in the natural bubbling regime (figure 2.4a) closely follows the one obtained numerically by Gutiérrez-Montes *et al.* (2013), including a stage of negative values (figure 2.4a,b). The experimental pressure signals were thus used herein to determine the bubble formation frequencies, provided that they show a characteristic peak in their associated PSD, as shown in figure 2.4(c).

The forcing of the natural bubbling regime was firstly explored and classified as *effective*, if the bubbles were formed at the forcing frequency, or *ineffective*, if they did not. On the one hand, for large enough values of the disturbance amplitude, ϵ, the effective forcing regime takes place, characterized by periodic bubbling events at the forcing frequency, f_f, featuring the release of a periodic train of monodisperse bubbles from the injector outlet, as shown in figure 2.3(b-e) for increasing forcing frequencies, and in figure 2.5(a) for one particular case. As can be observed in figure 2.5(b), under effective forcing conditions the

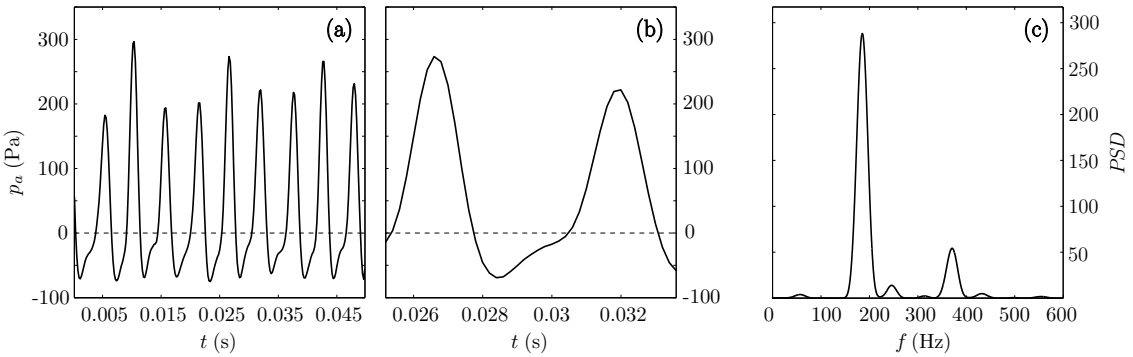

Figure 2.4: The natural bubbling regime for $u_n = 2.1$ m/s ($We = 26.6$) and $u_a = 17.4$ m/s ($\Lambda = 0.118$), resulting in a bubble formation frequency of $f_n = 185$ Hz. (a) Experimental air gauge pressure, (b) detail of the air gauge pressure during a bubbling event, showing a period of negative pressure after the formation of a bubble, and (c) Power spectral density of the air gauge pressure signal exhibiting a peak at the natural bubble formation frequency, f_n.

air pressure signal is purely periodic and shows constant amplitude events, with a power spectral density exhibiting a single peak at the forcing frequency f_f (figure 2.5c). Note that, in addition to the bubble formation frequency, the bubble volume, V_b, also varies since $V_b = Q_a/f_f$. On the other hand, if ϵ is smaller than a critical value, ϵ_c, the forcing is not effective and cannot control the bubble formation process. In this case, an irregular generation of non-uniform bubbles is observed, the air pressure does not follow the characteristic time evolution associated with the periodic bubbling regime (figure 2.5e) and the corresponding power spectral density does not show clear peaks neither at f_f nor at f_n (figure 2.5f).

Therefore, for each pair of values (u_n,u_a), that determines a particular bubbling regime with an associated natural bubbling frequency, f_n, the *critical forcing amplitude*, ε_c, required to achieve the bubble formation at a given forcing frequency, $f_f > f_n$, i.e. an effective forcing regime, was experimentally determined. Specifically, the value of ε_c was obtained as the minimum amplitude of the water velocity modulation needed to reach an effective forcing process. In dimensionless terms, the controlled bubble formation process, defined by the values of St and Λ, is reached for dimensionless amplitudes at least equal to the critical value $\epsilon_c = \varepsilon_c/u_n$. In fact, for $\varepsilon > \varepsilon_c$ the forcing remains effective and the bubble volume is given by $V_b = Q_a/f_f$. Thus, it can be said that the critical amplitude represents a minimum and energetically optimal value.

2.3.2 Results of the effective forcing regime

In the present section, the experimental results for the critical amplitude and the length of the intact ligament, l_i, under the effective forcing regime are presented for different values of u_n, u_a, and $f_f > f_n$.

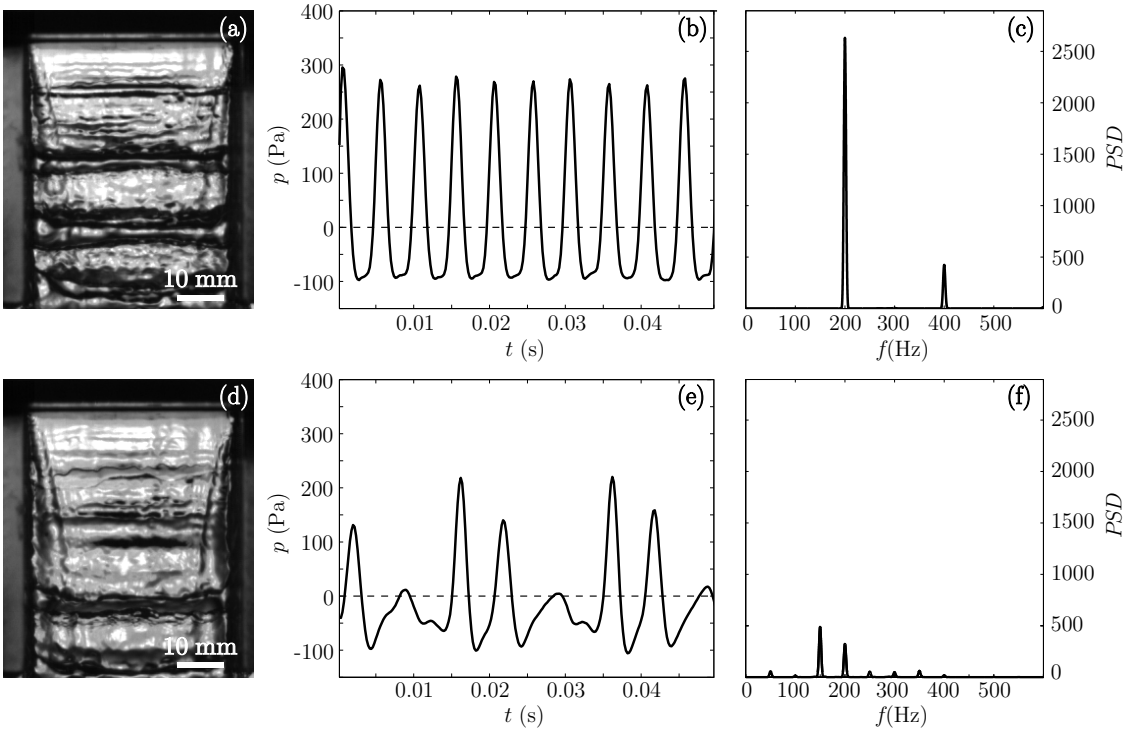

Figure 2.5: Experimental results for the forced bubbling regime at $f_f = 200$ Hz for $u_n = 1.8$ m/s ($We = 21.6$) and $u_a = 14.8$ m/s ($\Lambda = 0.125$) with $f_n = 131$ Hz. First row: effective forcing process with $\epsilon = \epsilon_c = 0.039$. Second row: ineffective forcing process for $\epsilon = 0.020 < \epsilon_c$. ($a$) and ($d$) Experimental images. ($b$) and ($e$) Gauge pressure in the air stream. (c) and (f) Power spectral density of the pressure signal.

Figure 2.3(b-e) show a sequence of effective forcing regimes for increasing values of f_f, and their corresponding critical amplitudes, ε_c, which increase with f_f. It is clear that smaller bubbles are generated at higher f_f, since $V_b = Q_a/f_f$ and Q_a is fixed. In addition, bubble detachment occurs closer to the nozzle as f_f increases, corresponding to smaller values of l_i. This type of analysis was extended to cover a wide range of values of u_n and u_a, determining ε_c for different values of f_f. Figure 2.6 summarizes the experimental results. In general, given the globally unstable nature of the bubbling regime (Bolaños-Jiménez *et al.*, 2011), the flow is insensitive to small perturbations and large disturbances are required for the forcing to prevail. Indeed, it has been found that $\epsilon_c \gtrsim 0.02$ under all the conditions herein explored. These relatively large values of ϵ_c indicate the importance of nonlinear effects in the forcing phenomenon (Meier *et al.*, 1992), as discussed in Sect. 2.4. Moreover, figure 2.6 clearly shows that, for each pair of u_n and u_a, the value of ε_c increases with f_f, as a consequence of the faster growth rate of the disturbance caused by the decrease of the bubble formation time, closely following a quadratic dependence $\varepsilon_c \propto f_f^2$, as revealed by figure 2.6(a). In the unforced case, the bubbling frequency is determined by the negative pressure established at the exit slit (Gutiérrez-Montes *et al.*, 2013) and, thus,

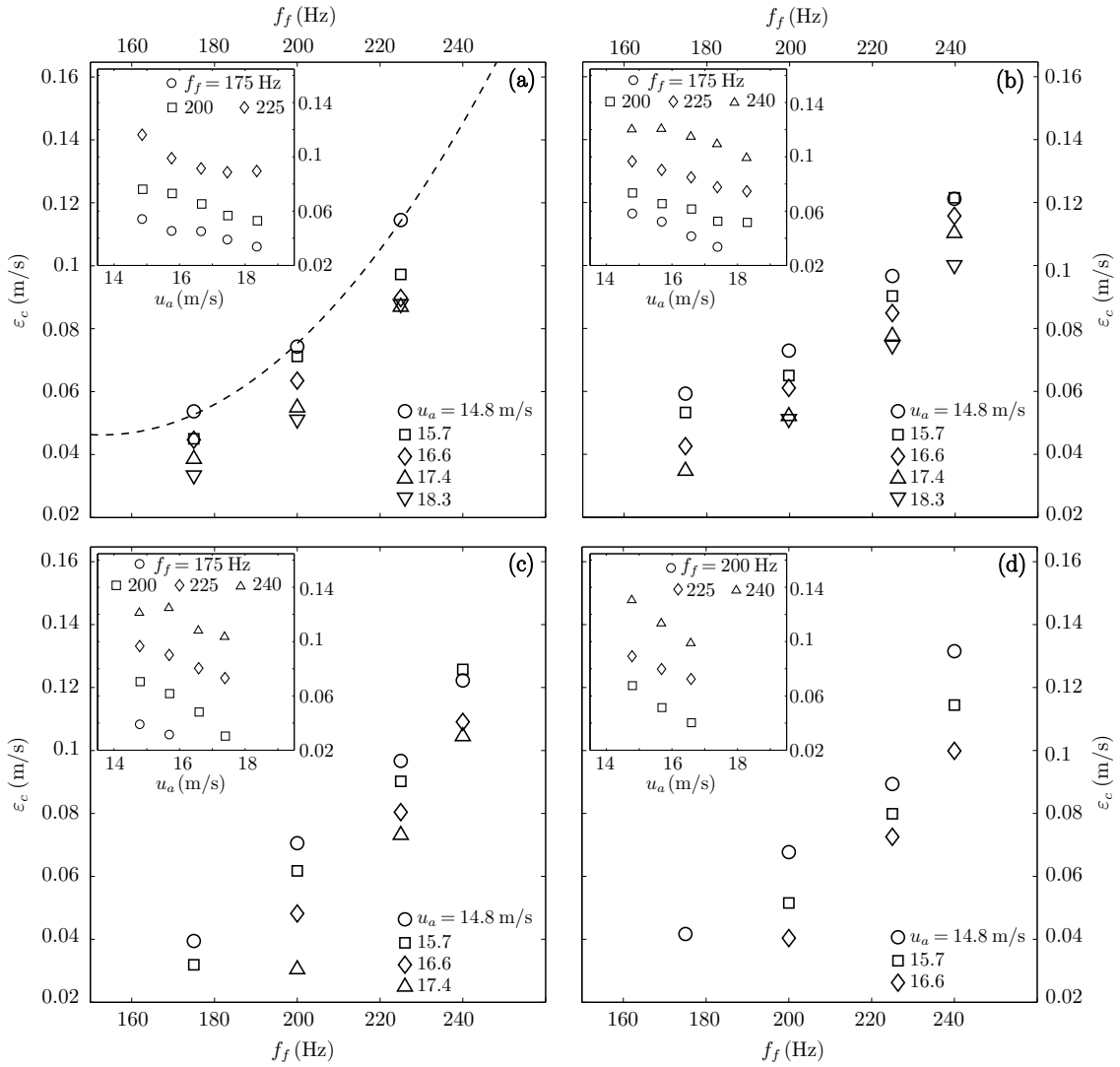

Figure 2.6: Evolution of the critical amplitude of the perturbations, ε_c, as a function of f_f for several values of u_a and (*a*) $u_n = 1.6$ m/s, (*b*) $u_n = 1.8$ m/s, (*c*) $u_n = 2.1$ m/s, (*d*) $u_n = 2.3$ m/s. In the panels, each data series corresponds to a given value of u_a. The insets show ε_c versus u_a for each value of u_n. The dashed line in (*a*) is a fit of the form $\varepsilon_c \propto f_f^2$, indicating the quadratic dependence. Although only one data series has been fitted for clarity, all of them follow the same trend.

the forcing acts as an additional mechanism that allows to increase the bubble formation rate. Since the time during which the mechanism acting in the unforced case is reduced when the forcing frequency is increased, a larger forcing amplitude is required to achieve an effective forcing regime. As shown in the next section, the forced bubbling process can be understood as a kinematic effect that modifies the natural bubbling regime.

In addition, figure 2.6 also reveals that, for a fixed values of u_n and f_f, the critical amplitude decreases as the air velocity increases, a result that can be clearly observed in the insets included in each panel. This behavior is also related to the negative pressure

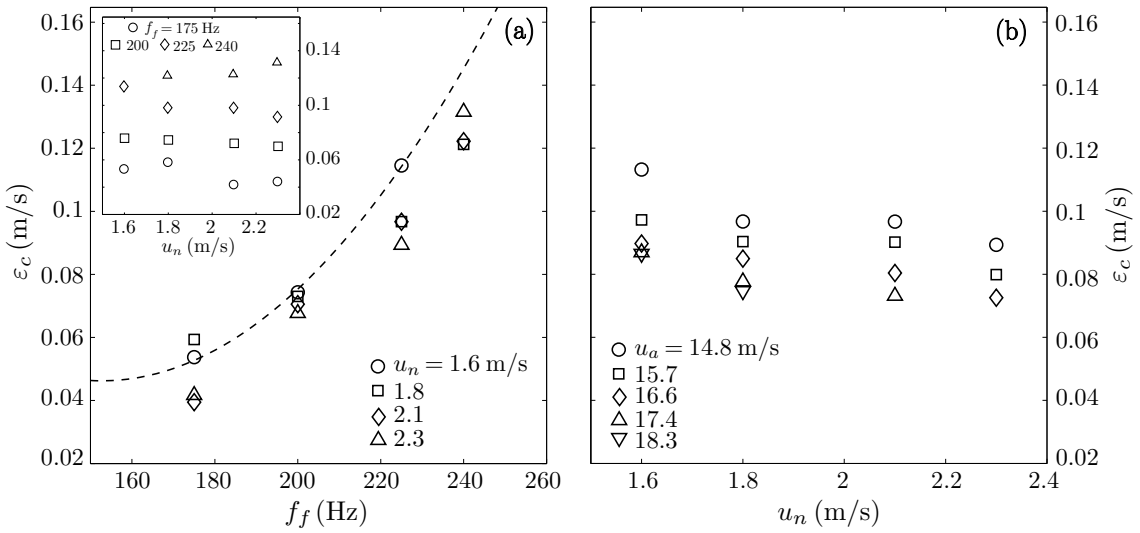

Figure 2.7: Critical amplitude (a) as a function of the f_f for different values of the water velocity and for a fixed air velocity, $u_a = 14.8$ m/s, and (b) as a function of the water velocity for different values of the air velocity and for a fixed forcing frequency $f_f = 225$ Hz. The dashed line in (a) is a quadratic fit, of the form $\varepsilon_c \propto f_f^2$, to the data corresponding to $u_n = 1.6$ m/s.

induced by the expansion of the air stream when it discharges from the air injector into the forming bubble (Gutiérrez-Montes *et al.*, 2013), $\Delta p = -\rho_a u_a^2 \beta(1-\beta)$, with $\beta = H_i/H_o$ the dimensionless thickness of the air injector. Since this effect becomes more important for increasing air velocities, a smaller forcing amplitude is required to impose a given effective forcing frequency when the air velocity grows. Nevertheless, the latter effect is likely to become weaker for values of $f_f \gg f_n$ outside the range explored herein.

To analyze the effect of u_n on ε_c, several results can be extracted from figure 2.6 and presented in figure 2.7. In particular, the value of ε_c for a fixed air velocity of $u_a = 14.8$ m/s is plotted as a function of f_f in figure 2.7(a), where the trend $\varepsilon_c \propto f_f^2$ explained before is again observed. However, unlike what happens with the air velocity, it can be observed that the value of ε_c is barely affected by u_n. Notice that, for a fixed forcing frequency, figure 2.7(b) shows a very weak effect of u_n on ε_c, compared with the effect of u_a displayed in figure 2.6 and discussed above. Therefore, it is concluded that the effect of the air velocity, u_a, on ε_c is more relevant than that of water velocity, u_n.

To have a better idea of the effects of the governing parameters, it proves convenient to represent the dependence of ε_c on f_f, u_a, and u_n, in compact form using their dimensionless counterparts. To this end, figure 2.8(a) shows that the nondimensional perturbation amplitude, ϵ_c, increases linearly with Λ for a constant value of St, consistent with the dependence of the critical forcing amplitude on the air and water velocities previously described. Moreover, figure 2.8(b) reveals that ϵ_c increases with St for a fixed value of Λ, again reflecting the dimensional result discussed above. Finally, the dependence of ϵ_c on both Λ and St can be obtained taking into account the facts that i) the critical amplitude

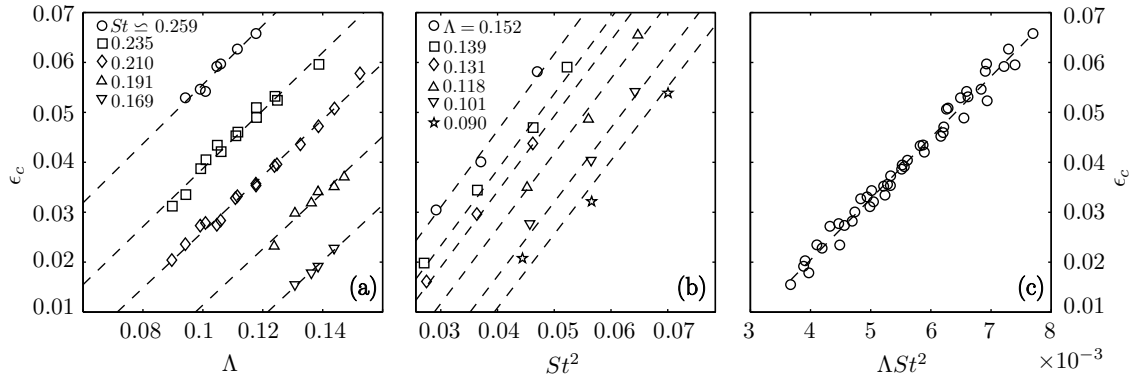

Figure 2.8: Experimentally determined dimensionless critical amplitude, ϵ_c. (a) ϵ_c as a function of Λ for different values of St, and (b) ϵ_c as a function of St^2 for several values of Λ. The dashed lines in (a) and (b) are linear fits. (c) ϵ_c as a function of $\Lambda\, St^2$, showing the collapse of all the data points, with the dashed line being the linear fit given by $\epsilon_c = 12.24\,\Lambda\, St^2 - 0.028$.

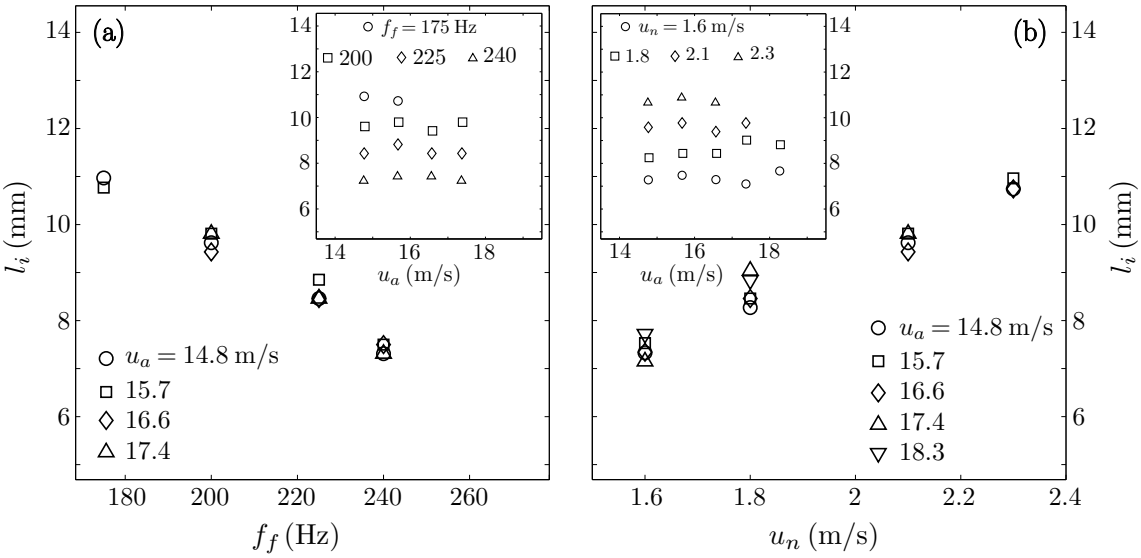

Figure 2.9: Length of the intact ligament under effective forcing regime, with $\epsilon = \epsilon_c$, (a) as a function of the forcing frequency for different values of the air velocity and for $u_n = 2.1$ m/s and (b) as a function of the water velocity for different values of the air velocity and for $f_f = 200$ Hz. The insets in (a) and (b) represent the effect of the air velocity for different forcing frequencies and different water velocities, respectively.

increases quadratically with the forcing frequency, ii) decreases with the air velocity and iii) barely depends on the water velocity, i.e. $\varepsilon_c \propto f_f^2/u_a$. Indeed, figure 2.8$(c)$ demonstrates that all the experimental data for ϵ_c collapse on a single curve when plotted as a function of $\Lambda\, St^2$, with the linear trend $\epsilon_c \propto \Lambda\, St^2$, indicating that $\varepsilon_c/u_n \propto u_n/u_a f_f^2 h_0^2/u_n^2$, and therefore $\varepsilon_c \propto f_f^2/u_a$.

As already commented above, the change in the bubbling frequency affects the bubble volume, $V_b = Q_a/f_f$, and modifies the length of the intact ligament, l_i, which can be

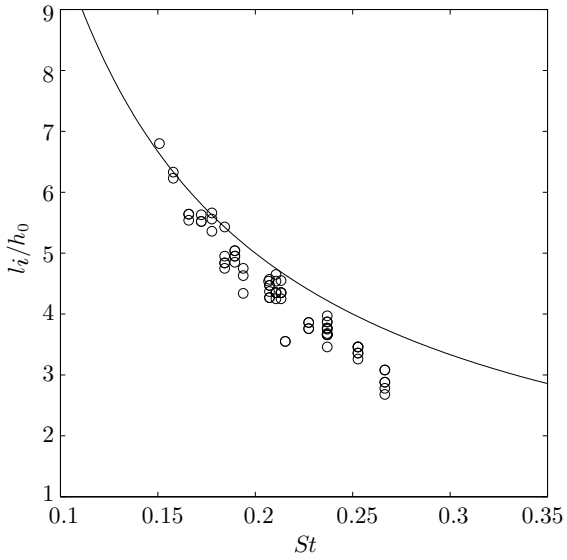

Figure 2.10: Dimensionless intact length as a function of the Strouhal number for all the experiments. The solid line represents the function $l_i/h_0 = 1/St$.

estimated as $l_i = u_d/f_f$, being u_d the downstream velocity of the initial deformation that finally causes the breakup. In fact, an inspection of figure 2.9, suggests that $u_d \simeq u_n$, providing $l_i \simeq u_n/f_f$. In particular, figure 2.9(a) shows that, for a given value of the water velocity, l_i decreases with the forcing frequency and barely depends on the air velocity (see inset in figure 2.9a). Moreover, it should be noted that, for a given forcing frequency, l_i increases linearly with the water velocity, and independently of the air velocity, being the slope nearly $1/f_f$ (see figure 2.9b). Nevertheless, for increasing forcing frequencies it has been observed that the slope becomes slightly smaller than $1/f_f$, and shorter intact lengths are obtained. This results could be associated to three dimensional instabilities triggered at higher forcing frequencies, which make the bubble separate closer to the injector tip. Similar results were reported by Gutiérrez-Montes *et al.* (2013), who observed that the intact ligaments obtained from two-dimensional numerical simulations, where three dimensional effects are not taken into account, were slightly larger than those measured experimentally (see figure 13 in Gutiérrez-Montes *et al.* 2013). Furthermore, if the intact length extracted from all the experiments is plotted in dimensionless form, namely l_i/h_0, as a function of St, the data almost collapse onto a single curve that closely follows the function $1/St$, as shown in figure 2.10. Therefore, $l_i/h_0 \simeq u_n/(f_f\, h_0)$, in agreement with the conclusion that $l_i \simeq u_n/f_f$. This result has also been corroborated by the theoretical model described in Sect. 2.4, where neither three dimensional nor air stream effects have been taken into account.

2.4 Analysis of the forcing effect

In the present section, we will describe the evolution of the perturbations on the water interface based on the models provided by Meier *et al.* (1992) and Mehring & Sirignano (1999), translating the origin of coordinates from $y = 0$ to the liquid sheet centerline position, $y = y_c = (H_o + H_w)/2$, and considering varicose perturbations. As stated in Sect. 2.2.1, the forcing process in the water streams produces a modulation of the water velocity at the nozzle exit (Eq. 2.6), complementary to the dynamic effects induced by the inner air stream, which accelerates the bubble formation mechanism. Moreover, as already pointed out in Sect. 2.3, the required critical amplitudes of the imposed monochromatic perturbations for effective forcing processes are found to exceed the validity of linear analyses (Eggers & Villermaux, 2008; Mehring & Sirignano, 1999; Meier *et al.*, 1992). To study the direct effect of the forcing process, the water stream can be simplified and considered in a first approximation as a planar sheet with free surfaces, i.e. neglecting the inner and outer aerodynamic effects, and modulated by velocity perturbations at the nozzle exit. In this case, the variations of the water velocity at the nozzle outlet generate kinematic waves in the water stream which grow downstream, inducing unsteady deformations of the liquid sheet (Meier *et al.*, 1992; Mehring & Sirignano, 1999). Specifically, the liquid velocity increases and decreases periodically in time, and the portions of liquid that exit the nozzle faster end up reaching the previous slower ones, resulting in the formation of a liquid cluster per cycle. These spatially growing fluid agglomerations present the convective nature of harmonic dilational waves generated at the nozzle exit, which result in bulges interspaced by almost a wavelength (Mehring & Sirignano, 1999). According to the experimental results, the breakup lengths are found to be closely equal to the perturbation wavelengths (figure 2.10), being much longer than the liquid sheet thickness. Thus, considering this long-wavelength assumption, an accurate description of the behavior of the free surfaces can be assured by a one-dimensional unsteady formulation (Eggers & Villermaux, 2008; Zhu *et al.*, 2000).

Assuming a two-dimensional incompressible, inviscid water stream in the (x, y) plane emerging from a nozzle into a gaseous atmosphere, and neglecting aerodynamic and gravitational effects, the mass conservation and momentum equations for the water sheet write,

$$\frac{\partial u_w}{\partial x} + \frac{\partial v_w}{\partial y} = 0, \tag{2.7}$$

$$\frac{\partial u_w}{\partial t} + u_w \frac{\partial u_w}{\partial x} + v_w \frac{\partial u_w}{\partial y} + \frac{1}{\rho_w} \frac{\partial p_w}{\partial x} = 0, \tag{2.8}$$

$$\frac{\partial v_w}{\partial t} + u_w \frac{\partial v_w}{\partial x} + v_w \frac{\partial v_w}{\partial y} + \frac{1}{\rho_w} \frac{\partial p_w}{\partial y} = 0, \tag{2.9}$$

where v_w is the fluid velocity in the y-direction. Following a derivation similar to that proposed by Mehring & Sirignano (1999), which results in an equivalent inviscid simplification of the one-dimensional formulation for cylindrical viscous jets by Eggers & Dupont (1994),

the system (2.7-2.9) can be reduced to a one-dimensional approximation. A normal stress balance at the interfaces eliminates the pressure from the formulation keeping the surface tension effects (Lee, 1974). This leads to a more realistic representation than the analytic solution proposed by Meier *et al.* (1992), where the surface tension is neglected and the sheet local thickness blows up to infinity, specially for large Strouhal numbers.

If the local liquid sheet thickness and its centerline position are denoted by $h = h(x,t)$ and $y_c = y_c(x,t)$, respectively, the dependent variables (u_w, v_w, p_w) can be expressed by a power-series expansion in terms of $(y - y_c)$ (Mehring & Sirignano, 1999). Taking h_0 and u_n as the reference magnitudes, we introduce the dimensionless quantities, $\hat{u} = u_w/u_n$, $\hat{h} = h/h_0$, $x^* = x/h_0$ and $t^* = t/(h_0/u_n)$. In addition, considering that the velocity modulation just induces dilational perturbations on the liquid sheet, only variations of $\hat{h}$ and $\hat{u}$ appear, while the central plane location is constant, $y_c = (Ho + Hw)/2$, (Meier *et al.*, 1992; Mehring & Sirignano, 1999; Kim & Sirignano, 2000). Therefore, the system (2.7-2.9) is reduced to the dimensionless leading order one-dimensional equations,

$$\frac{\partial \hat{h}}{\partial t^*} = -\frac{\partial}{\partial x^*}(\hat{u}\hat{h}), \tag{2.10}$$

$$\frac{\partial \hat{u}}{\partial t^*} = \frac{\partial}{\partial x^*}\left\{\frac{1}{2We_w}\left[1 + \frac{1}{4}\left(\frac{\partial \hat{h}}{\partial x^*}\right)^2\right]^{-3/2}\frac{\partial^2 \hat{h}}{\partial x^{*2}} - \frac{\hat{u}^2}{2}\right\}, \tag{2.11}$$

where $We_w = \rho_w u_n^2 h_0/\sigma$ represents the Weber number evaluated using the characteristic magnitudes of the unforced water sheet. Equations (2.10) and (2.11) define a closed hyperbolic system in the conservative form for $\hat{h}$ and $\hat{u}$. The initial conditions are given by the steady solutions, i.e. the unforced case, and the boundary conditions at the nozzle outlet ($x^* = 0$) are

$$\hat{h}(0,t^*) = 1, \tag{2.12}$$

$$\hat{u}(0,t^*) = u_{w,0}(t)/u_n, \tag{2.13}$$

where $u_{w,0}(t)$ is the modulated velocity given by Eq. (2.6). The system has been solved as an initial and boundary value problem by means of an explicit finite-difference scheme, using the Richtmyer splitting of the Lax-Wendroff method. Equations (2.10) and (2.11) are discretized on a uniform staggered grid, where the spatial derivatives of $\hat{h}$ in Eq. (2.11) are obtained by the second-order central-difference scheme for first derivatives and the first-order one for second derivatives. The time integration involves a two-step scheme with a first-order Lax predictor and a second-order leapfrog corrector (Hirsch, 2007). The accuracy of the numerical scheme has been checked by successive refinement of the mesh size and time step. A number of grid points per wavelength of 125 and a dimensionless time step of 0.001 was found to be appropriate for a grid-independent solution.

As described in Gutiérrez-Montes *et al.* (2013), the dynamic phenomena induced by the inner air stream triggers the bubble formation process in the unforced case. However,

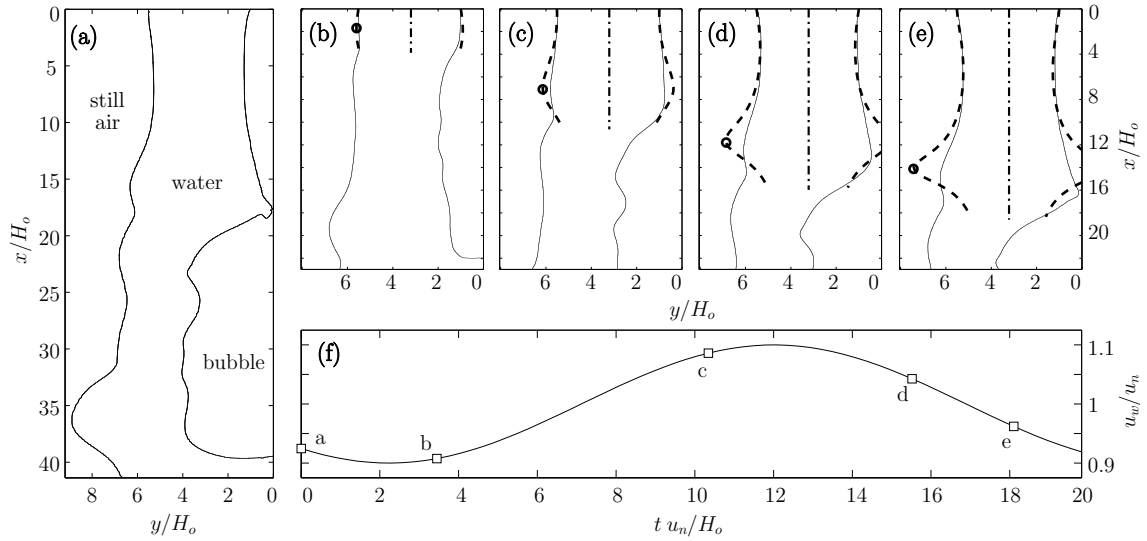

Figure 2.11: (*a-e*) Inner and outer water interfaces at different instants during a forced bubble formation cycle corresponding to $We = 38.8$ and $\Lambda = 0.147$, with $f_f = 294$ Hz, where the solid lines represent the results given by numerical simulations and the dashed lines are the prediction of the one-dimensional model (Eqs. 2.10-2.13) with $We_w = 176.1$ and $\epsilon = 0.1 > \epsilon_c = 0.065$, the dashed-dotted lines indicate the centerline position, y_c. (*f*) Time evolution of the numerical modulated water velocity at the nozzle exit during the whole event, where the instants showed in (*a-e*) are indicated.

when the forcing amplitude is sufficiently large, the water sheets are mainly destabilized by the external perturbations and the one-dimensional approach defined by the system (2.10-2.13) can qualitatively describe the evolution of the imposed disturbances, giving a good prediction for the location of the maximum amplitude, i.e. the external cluster crest formed from the previous pinch-off event. Thus, in order to assess the prediction of Eqs. (2.10-2.13), since the experimental images do not show the (x, y) view, the evolution of the water interface is compared in figure 2.11 with that given by the numerical simulations performed with OpenFOAM during a bubble formation cycle. For the sake of clarity, the value of the imposed disturbance analyzed in figure 2.11 is larger than the critical one to better appreciate its effect on the water sheet. Solutions of Eqs. (2.10-2.13) have been plotted from the nozzle outlet ($x = 0$) to a position slightly larger than $x_d(t^*)$, being x_d the streamwise location of the maximum deformation, at different instants over a whole cycle to clearly identify the position where the calculated cross section reaches a local maximum. Specifically, figure 2.11(a) corresponds to a pinch-off event obtained from the numerical simulations, showing the formed bubble as well as the intact ligament, which starts to inflate due to overpressure generated during the bubble collapse. At this moment, a new cycle begins, in which the liquid leaves the nozzle with low velocity (figure 2.11f), while a small bump (incipient neck) starts to form towards the air stream in the inner interface, close to the nozzle exit, due to the sudden decrease of pressure in the air sheet. As the water velocity at the exit increases (figure 2.11b), the one-dimensional model predicts a

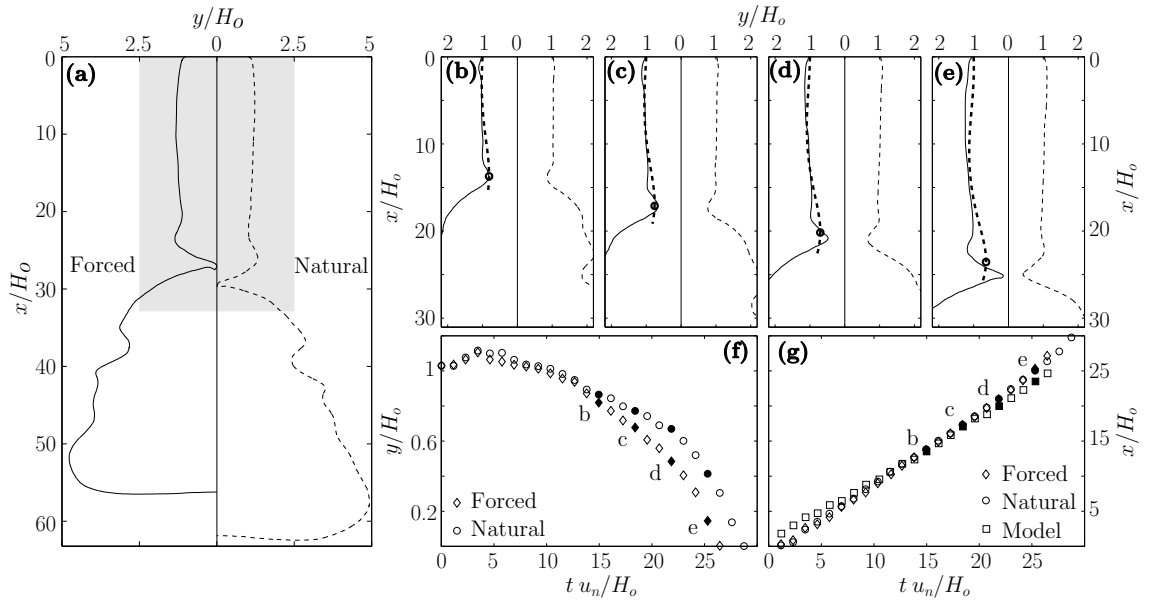

Figure 2.12: Comparison of a natural bubbling process, corresponding to $We = 38.8$ and $\Lambda = 0.147$, $f_n = 196$ Hz, with the effectively forced one at $f_f = 216$ Hz and $\epsilon = 0.025 \simeq \epsilon_c = 0.022$. ($a$) Inner interface obtained by means of numerical simulations for the forced case (left side, solid line) and for the unforced process (right side, dashed line) at the pinch-off moment. (b-e) Same as (a) but in a region around the narrowest section (denoted neck), and together with the inner interface calculated with the one-dimensional approach for the forced case (thick dashed line), at different instants during the bubbling cycle. A circle has been used to indicate the maximum deformation given by the model. (f) Time evolution of both the forced and natural protuberances given by the simulations along the y-direction. (g) Time evolution of the forced and natural numerical protuberances along the x-direction, together with that given by the model.

slight increment of thickness in the water sheet, which grows downstream as time evolves (figure 2.11c-e). It can be observed that the amplitude of the perturbation is larger than that obtained numerically. This might be because the model considers a free water sheet and does not take into account any effect of the air stream or coupled effects between the two water sheets. In fact, notice that, in figure 2.11(e) the amplitude of the perturbation in the inner interface is considerably larger than the outer one, corroborating that there is an influence of the fast stream of air that flows between the two water sheets in the growth rate of the perturbations. An additional effect that has not been included in the model is the influence to the forming bubble in the development of the perturbation. Thus, as the forming bubble grows, the liquid stream around it accelerates, stretching the outer air-liquid interface and, consequently, inhibiting the growth of the perturbation. Nevertheless, it can be observed in figure 2.11(b-e) that the downstream longitudinal position of the maximum deformation, indicated by a circle, is well predicted by the model (Eqs. 2.10-2.13), particularly in the outer interface.

Since the critical amplitude ε_c is the minimum one which properly controls the bubble formation at the desired frequency $f_f > f_n$, the maximum of the liquid bulge produced

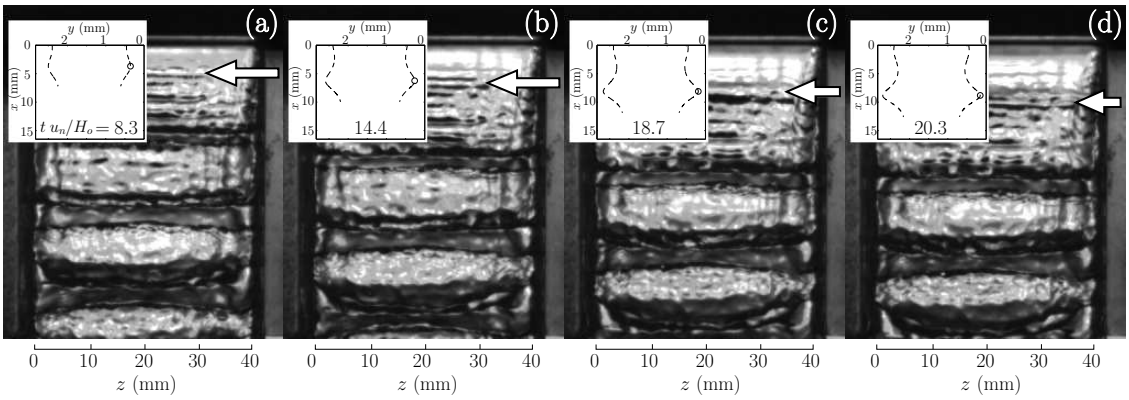

Figure 2.13: Experimental images showing the spanwise view of the sheets, (x, z), of some instants during a forced bubble formation cycle corresponding to $We = 21.5$ and $\Lambda = 0.125$, with $f_n = 131$ Hz, under a forcing frequency equal to $f_f = 200$ Hz, and for $\epsilon = \epsilon_c = 0.039$. Each snapshot includes a panel in which the corresponding transverse view, (x, y), of the water stream thickness, provided by Eqs. (2.10-2.13), is represented with the same x-coordinate scale as in the experimental image. A circle is used to indicate the position of the maximum thickness given by the model. The horizontal arrows have been added to point the downstream position of the maximum deformation of the water interface in each panel.

by the forcing effect must be located in the vicinity of the initial protuberance that is generated at the beginning of the cycle, i.e. the naturally induced incipient neck, adding its growth to the aforementioned dynamic effects. Moreover, it has been found that the maximum possible deformation for ε_c at each cycle and in a distance up to $u_{w,0}(t = 0)/u_n T^*$, being $T^* = u_n/(f_f h_0) = 1/St$ the period corresponding to the dimensionless forcing frequency, is reached when the forcing signal is in phase with the bubble pinch-off. In that case, the location of this local maximum results in $x_d(T^*) = u_n/f_f$, coinciding with the perturbation wavelength and in good agreement with the experimental results, as shown in figure 2.10. This fact can be explored in figure 2.12, where an effective forced case is compared with its unforced counterpart. In figure 2.12(a) it can be observed that, in accordance with the previous section, since u_n is kept constant in both cases, the increment in the bubble formation frequency leads to a reduction in the final bubble volume and, consequently, in l_i. Figure 2.12(b-e) shows a larger growth of the initial protuberance towards the symmetry plane in the forced case in comparison with the natural transverse evolution of the interface at the narrowest point, hereafter referred to as neck. Indeed, figure 2.12(f), which shows the time evolution of the air stream semi-thickness in the neck, indicates that its closure is faster in the forced case. In addition, it can be appreciated that the longitudinal evolution of the neck location is the same in both cases (figure 2.12g), with velocities nearly equal to u_n. Nevertheless, the x-position given by the model slightly differs from that obtained numerically (figure 2.12g), which indicates that the phase speed of the perturbation remains between the maximum and the minimum values of the modulated velocity (Zhu *et al.*, 2000). Note that, despite the differences, the

theoretical liquid cluster nearly coincides with the natural neck for most of the cycle (figure 2.12*b-d*). However, some discrepancies are observed at the beginning of the cycle, when the growth of the bulge is still very small, and during the last instants (figure 2.12*e*), when the effect of the air stream during the collapse event violently accelerates the neck towards the symmetry plane.

Finally, figure 2.13 compares the theoretical prediction of the water sheet thickness as well as the local maximum deformation (indicated by a circle) with the experimental visualizations. In the (x, z) plane view showed by the images, the downstream position of the maximum deformation corresponds to a dark horizontal stripe, highlighted by a white arrow for clarity, which is more evident in figure 2.13(*c-d*). It can be appreciated how the x-position of the bulge observed in the images is well predicted by Eqs. (2.10-2.13). Furthermore, the last snapshot (figure 2.13*d*) represents the pinch-off event, in which the air sheet appears completely broken in a position nearby the theoretical bulge crest, which corroborates the good agreement between the experiments and the one-dimensional model.

2.5 Conclusions

The present work reports a novel technique to control the bubbling process naturally established in a water-air-water planar co-flow configuration, with the aim of producing monodisperse bubbles of a prescribed volume at a constant rate. For such purpose, a forcing system that modulates the water flow rate has been designed and implemented. Thus, the water sheets are forced at the nozzle exit by a monochromatic perturbation of the form $u_{w,0}(t) = u_n + \varepsilon \sin(\omega t + \varphi)$, where u_n is the unforced water velocity and ε the forcing amplitude, which is experimentally obtained from measurements of the pressure variations inside the water stream upstream from the injector exit.

The experimental results indicate that the bubbling process can be controlled to obtain a periodic formation of monodisperse bubbles of volume $V_b = Q_a/f_f$ at a desired frequency, $f_f > f_n$. The controlled bubbling process of an otherwise unforced natural, bubbling regime, characterized by the Weber number, $We = \rho_w u_n^2 H_o/\sigma$, and the water-to-air velocity ratio, $\Lambda = u_n/u_a$, can be accomplished by forcing the water stream at a given frequency, f_f, with an amplitude, ε, larger than a certain critical one, ε_c. In fact, a wide range of natural bubbling regimes have been forced at different frequencies with the aim at establishing the corresponding values of ε_c. The results obtained show a dependence of the form $\varepsilon_c \propto f_f^2$, as a consequence of the faster growth rate of the disturbance that is required when the forcing frequency increases. Moreover, a relevant influence of the air velocity on ε_c has been observed within the analyzed experimental range, which is an effect related to the underpressure induced by the air stream at the nozzle exit (Gutiérrez-Montes *et al.*, 2013). Therefore, for a given forcing frequency, decreasing values of ε_c are needed as the air velocity increases. In contrast with the important influence of the air velocity,

a very weak dependence of ε_c on the mean water velocity, u_n, has been found. These dependencies have been confirmed when the dimensionless critical amplitude, $\epsilon_c = \varepsilon_c/u_n$, is expressed as a function of $\Lambda\, St^2$, showing that $\epsilon_c \propto \Lambda\, St^2$. In addition, the experimental measurements of the intact length, l_i, reveal a linear dependence on both the water velocity and forcing frequency and a negligible dependence on the air velocity. In particular, shorter values of l_i are found for increasing values of f_f, while increasing values of l_i have been observed for increasing water velocities. The results reported indicate that the air stream has an important influence on the transverse dynamics of the air-water interface, that is, on the growth and collapse of the neck through the induced inner underpressures and consequently on the required critical amplitudes. However, it has an almost negligible effect on the longitudinal dynamics, i.e. on the downwards traveling velocity of the deformation that finally causes the breakup. In fact, the inverse of the dimensionless breakup lengths linearly increases with the dimensionless forcing frequency, $h_0/l_i \simeq St$, resulting in $l_i \simeq u_n/f_f$.

Moreover, the effects of the forcing process over the water stream, which are complementary to the effects induced by the air stream, are found to be of purely kinematic nature. Indeed, the temporal fluctuations of the liquid velocity, induced by the imposed monochromatic perturbation, result in the formation of liquid bulges that grow transversely as they propagate downstream. Thus, a one-dimensional model has been implemented to describe the evolution of the air-water interface of the forced water sheet. It has been found that, for critical amplitudes, the position of local maximum deformation provided by the model closely follows the temporal evolution of the neck obtained both experimental and numerically, corroborating the applicability of the model. Furthermore, since the critical amplitude represents the minimum value required to reach an effective forcing process, the local maximum transverse deformation in a given cycle is achieved for a forcing signal in phase with the bubble pinch-off, resulting in a location of the bulge maximum equal to the perturbation wavelength. This result is in good agreement with the breakup lengths obtained from the experiments.

This Chapter is comprised, in part, in the paper: "Controlled formation of bubbles in a planar co-flow configuration", by Ruiz-Rus, J., Bolaños-Jiménez, R., Gutiérrez-Montes, C., Sevilla, A. & Martínez-Bazán, C., published in the International Journal of Multiphase Flow (Ruiz-Rus et al. *2017).*

CHAPTER
THREE

Formation of bubbles in forced cylindrical co-flowing air-water jets

3.1 Introduction

A common technique to produce bubbles is by injecting a jet of air surrounded by a liquid flow (see Chuang & Goldschmidt, 1970; Oğuz & Prosperetti, 1993; Tsuge *et al.*, 1997; Bhunia *et al.*, 1998; Sevilla *et al.*, 2005*a*; Gordillo *et al.*, 2007, among others). In particular, in these systems, the gas flow discharges inside a co-flowing laminar liquid stream. Compared with the case of injecting air in still liquids, the so-called co-flow technique enables the generation of smaller and monodisperse bubbles, allowing the injection of higher gas flow rates and preventing the bubble coalescence at the exit of the injector. Both the classical cylindrical (see Rodríguez-Rodríguez *et al.*, 2015, and references therein) and the alternative planar (Gutiérrez-Montes *et al.*, 2013; Bolaños-Jiménez *et al.*, 2016; Ruiz-Rus *et al.*, 2017) geometries have been studied, and the influence of the gas injection conditions on the bubbling processes has been described (Gordillo *et al.*, 2007; Gutiérrez-Montes *et al.*, 2014). However, in this case, the individual and precise control of the bubble volume and formation frequency results strongly conditioned by the geometric characteristics of the injector (Sevilla *et al.*, 2005*a*,*b*; Rodríguez-Rodríguez *et al.*, 2015; Gutiérrez-Montes *et al.*, 2014). Therefore, alternative techniques and devices to force the bubble detachment in a controlled way are required.

Thus, due to the relevance of the topic, a considerabe effort has been done during the last decades to develop new methods to generate controlled-size bubbles using different forcing techniques that act on the gas stream. The application of pulsed pressure waves to the gas phase (Shirota *et al.*, 2008; Najafi *et al.*, 2008; Makuta *et al.*, 2013), the movement or vibration of the gas injector (Grinis & Monin, 1999; Vejrazka *et al.*, 2008; Waghmare *et al.*, 2008; Wang *et al.*, 2016), the use of a rotational porous plate (Fujikawa *et al.*, 2003), the employment of elastic tubes (Sanada & Abe, 2013; Abe & Sanada, 2015) or a piston (Ostmann & Schwarze, 2018), or the application of electric fields (Di Bari & Robinson, 2013; Xu *et al.*, 2017; Wang *et al.*, 2018) constitute some of the methods used to control the bubble size when the air discharges into still liquid. Moreover, it can also be found other techniques that inject pulsed pressurized gas using a liquid cross-flow (Ohl,

2001; Palanchon *et al.*, 2003). Similarly, there is a vast literature on analogous forcing techniques to generate monodisperse on-demand droplets by means of similar methods, such as vibration, pressure fluctuations or ultrasound (see e.g. Zhu *et al.*, 2016*b*,*a*; Castrejón-Pita *et al.*, 2008, 2012; Frommhold *et al.*, 2014; Sauret & Cheung Shum, 2012). Alternatively to the co-flow configuration, the flow focusing technique also allows to generate monodisperse microbubbles using an outer liquid flow field (Gañán-Calvo & Gordillo, 2001; Gordillo *et al.*, 2004; Garstecki *et al.*, 2004; Evangelio *et al.*, 2015). Some studies can be found on forcing methods applied in this configuration, but acting over the surrounding liquid stream. For instance, a streaming flow in the liquid phase can be induced by means of ultrasound (Chong *et al.*, 2015) to control the bubble generation process.

However, to the best of the author's knowledge, a forcing technique that stimulates the air stream in a cylindrical co-flow configuration, as it is proposed in the present work, has not been explored yet. In particular, in Chapter 2 (see Ruiz-Rus *et al.*, 2017, in addition), the modulation of the external liquid flow rate in a planar co-flow configuration has been shown to represent a new and effective technique to control both the generation frequency and the bubble size independently. In this Chapter, we present a different method that, instead of forcing the liquid phase, acts over the gas stream, using a cylindrical configuration, which is more extended in industrial applications than the planar configuration.

Consequently, the purpose of the present study is to describe the performance of a new method to effectively and easily control both the size and frequency of the bubble generation when employing a cylindrical co-flow configuration. Thus, we experimentally analyze the mechanisms that are involved in the bubble formation dynamics in an axisymmetric co-flow configuration under the influence of harmonic pressure perturbations induced in the gas feeding line. To investigate this method we performed experiments in a cylindrical gas-liquid co-flow device with a varying gas flow rate, which is produced by means of a monochromatic pressure modulation of the gas stream. The technique performance is determined by characterizing the minimum pressure amplitude which is required to achieve an effective forcing process, as a function of the control parameters. The resulting characterization allows the users to enhance the control of the bubble generation process by incorporating the proposed forcing system.

The Chapter is organized as follows. Section 3.2 describes the experimental facility and techniques used in the present work while Sect. 3.3 includes the results of the bubbling process obtained imposing the effective forcing amplitude, where two different bubbles modes have been observed. Next, Section 3.4, focuses on the characterization of the intact ligaments observed in each bubbling mode and the determination of the transition from one mode to the other. Next, in Section 3.5, the forcing effect has been modelled to determine the physical mechanisms driving the bubble neck formation and Section 3.6 is devoted to conclusions.

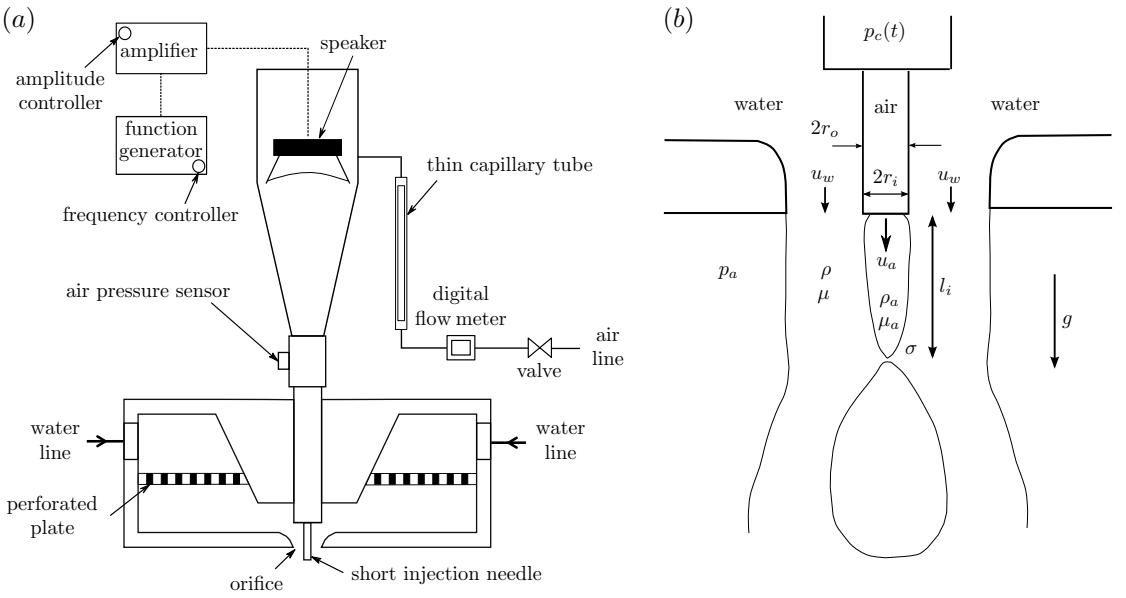

Figure 3.1: (a) Schematic representation of the experimental facility, showing the feeding systems of both the water and the air streams. A continuous water jet is emitted through an orifice at the bottom of a cylindrical reservoir. The air forcing device is fed through a thin capillary tube to achieve a constant air flow rate. Air pressure perturbations are induced by means of a loudspeaker. A short needle is used to inject the air from the forcing device toward the center of the water jet. (b) Sketch of the analyzed flow configuration, including the relevant physical parameters. The bubble pinch-off instant is depicted, showing the intact ligament attached to the needle, as well as the newly formed bubble.

3.2 Experimental approach

In this section, the experimental setup, the flow conditions and the experimental techniques used to obtain the results are described in detail.

3.2.1 Facility and flow conditions

The experimental set-up used in the present work, schematized in figure 3.1(a), consists of a gas-liquid co-flow device adapted from a previous set-up (Gordillo *et al.*, 2007), which has been modified to incorporate a forcing system to stimulate the air stream. In the co-flow device, a gas stream is coaxially injected at the core of a free liquid jet at large Reynolds and Weber numbers (Gordillo *et al.*, 2005; Sevilla *et al.*, 2005b,a; Gordillo *et al.*, 2007; Rodríguez-Rodríguez *et al.*, 2015). In particular, the experimental facility described by Gordillo *et al.* (2007) was used to generate an axisymmetric air-water co-flowing jet. It consists of a liquid reservoir from which a continuous water jet discharges vertically through an orifice of radius $r_w = 4$ mm. A constant water flow rate, Q_w, was supplied to the reservoir, being its value controlled and measured by means of a high-precision valve and a flow meter, respectively. To attenuate undesired liquid disturbances, a perforated

plate and a piece of foam were placed inside the water vessel. Moreover, the orifice was shaped as a contraction, to ensure a nearly uniform water velocity profile at the exit (Gordillo *et al.*, 2007). The air flow was injected at the centerline of the water jet through a needle. In particular, in this work we used a needle that corresponded to the experimental set X reported in Gordillo *et al.* (2007), with inner and outer radii $r_i = 0.4$ and $r_o = 0.6$ mm, respectively. Besides, a short needle length, $L = 17$ mm, was used to minimize the associated pressure losses. In addition, a short needle length reduced the damping of the pressure perturbations introduced upstream of the needle, reaching the bubble with a large enough amplitude to effectively force the air-water stream. It is important to emphasize that, due to the use of a short air injection needle, the air flow rate feeding the bubble does not remain constant during the bubble formation process. In fact, the associated pressure drop along the needle is lower than the characteristic pressure fluctuations inside the forming bubble, causing the instantaneous air flow rate feeding the bubble, $Q_a(t)$, to vary during the formation cycle, even in the unperturbed bubbling cases (Gordillo *et al.*, 2007).

The co-flow system described above was modified by including a forcing device into the gas line that supplies the air flow to the injection needle and induces a controlled pressure modulation to the air stream (figure 3.1*a*). It consists of a loud speaker (SP-45/8, MONACOR) placed inside an inverted horn-shaped vessel that includes an air inlet and a needle holder at its outlet. The inner shape of the air chamber allows an optimal performance of the speaker, minimizing the attenuation of the induced pressure perturbations. Contrary to the concept proposed by Shirota *et al.* (2008), the present device is continuously fed with a constant air flow rate, Q_c. Therefore, in the work at hand, a train of bubbles of controlled volume could be generated at the forcing frequency, rather than a single bubble produced by a pair of pulsed acoustic waves (Shirota *et al.*, 2008; Abe & Sanada, 2015; Rodríguez-Rodríguez *et al.*, 2015). The air flow was supplied to the chamber from a compressed air bottle, controlled with a pressure regulator and a high-resolution valve, and measured by means of a digital mass flow meter. Moreover, a long capillary tube was placed upstream the chamber, imposing a pressure drop much larger than the characteristic pressure variation inside the chamber (see Corchero *et al.* 2006), thus ensuring a constant air supply to the air chamber, Q_c. Finally, the speaker was excited by means of periodic sinusoidal electric signals provided by a tunable-frequency function generator (FG110, YOKOGAWA), which allowed an easy selection of the forcing frequency, f_f. These signals, previously amplified by a power amplifier (PA-702, MONACOR), drive the speaker, whose motion induces a periodic perturbation of the air pressure. To fully characterize the induced perturbation, the temporal evolution of the air pressure inside the chamber, $p_c(t)$, was measured by means of a pressure sensor placed at the chamber exit (figure 3.1*a*). The pressure signals were registered during the speaker performance showing sinusoidal shapes with the forcing frequency, f_f, and amplitude, Δp_c, accurately

adjustable through the amplifier.

Figure 3.1(b) shows a schematic representation of the bubble pinch-off instant, including the relevant physical parameters involved in the problem, where p_a denotes the atmospheric pressure, g is the acceleration of gravity, σ is the air-water surface tension coefficient, μ and μ_a are the water and air viscosities, respectively, ρ represents the water density while ρ_a stands for the air density, and u_w and u_a are the mean water and air velocities at the exit, respectively. Regarding the geometrical parameters, r_i and r_o stand for the inner and the outer air injector radii, L is its length, and r_w is the water jet radius. Besides, l_i indicates the intact length, which is the length of the air lump that remains attached to the needle tip after the bubble detachment. In this work, the water jet velocity was varied in the range $1 < u_w = Q_w/A_w < 2$ m/s, being $A_w = \pi(r_w^2 - r_o^2)$ the water exit cross-section. Since $Q_a(t) \neq Q_c$ in all the experiments reported here, the average air velocity at the needle exit is defined as $u_a = Q_c/(\pi r_o^2)$, being its experimental range $0.5 < u_a < 8$ m/s. In addition, the forcing frequency was varied in the range of $250 \leqslant f_f \leqslant 500$ Hz, being the lower limit imposed by the natural bubbling frequency, f_n, while the upper value depends on the maximum response of the loud speaker at the selected frequency. Using r_o and u_w as the characteristic scales for length and velocity, respectively, the dimensionless parameters describing the problem are the following. As mentioned before, the Reynolds and Weber numbers, $Re = \rho u_w r_o/\mu \gg 1$ and $We = \rho u_w^2 r_o/\sigma \gg 1$, respectively, are both large. Therefore, the inertia of the liquid dominates over viscous and surface tension forces in the experiments reported herein. Finally, the Froude number based on the intact length, $Fr = g l_i/u_w^2 \ll 1$, indicating that gravity effects are negligible in all the experiments. The value of the air Reynolds number, $Re_a = \rho_a u_a r_o/\mu_a$, was always sufficiently large for viscous effects to be negligible within the bubble. In addition, the air flow inside the needle was not fully developed (Gordillo *et al.*, 2007). Therefore, the dimensionless control parameters of the problem are reduced to the forcing Strouhal number, $St = f_f r_o/u_w$, and the liquid-to-gas mean velocity ratio, $\Lambda = u_w/u_a$. The experimental range of both parameters covered in the present work was $0.05 \lesssim St \lesssim 0.23$ and $0 < \Lambda < 2.3$. At this point, it is important to mention that the unperturbed experiments reported here lead to well defined natural bubbling regimes with periodic generation of monodisperse bubbles (Sevilla *et al.*, 2005a; Gordillo *et al.*, 2007). In fact, these flow conditions give rise to natural bubble generation frequencies in the range $125 < f_n < 300$ Hz. However, larger values of Λ lead to the transition from periodic bubbling to jetting, as reported by Sevilla *et al.* (2005b) for constant air flow rate conditions. Although a totally developed jetting regime is still not present in these particular cases, the generated bubbles show slightly lower monodispersity with weak fluctuations of the bubbling frequency (Sevilla *et al.*, 2005a,b).

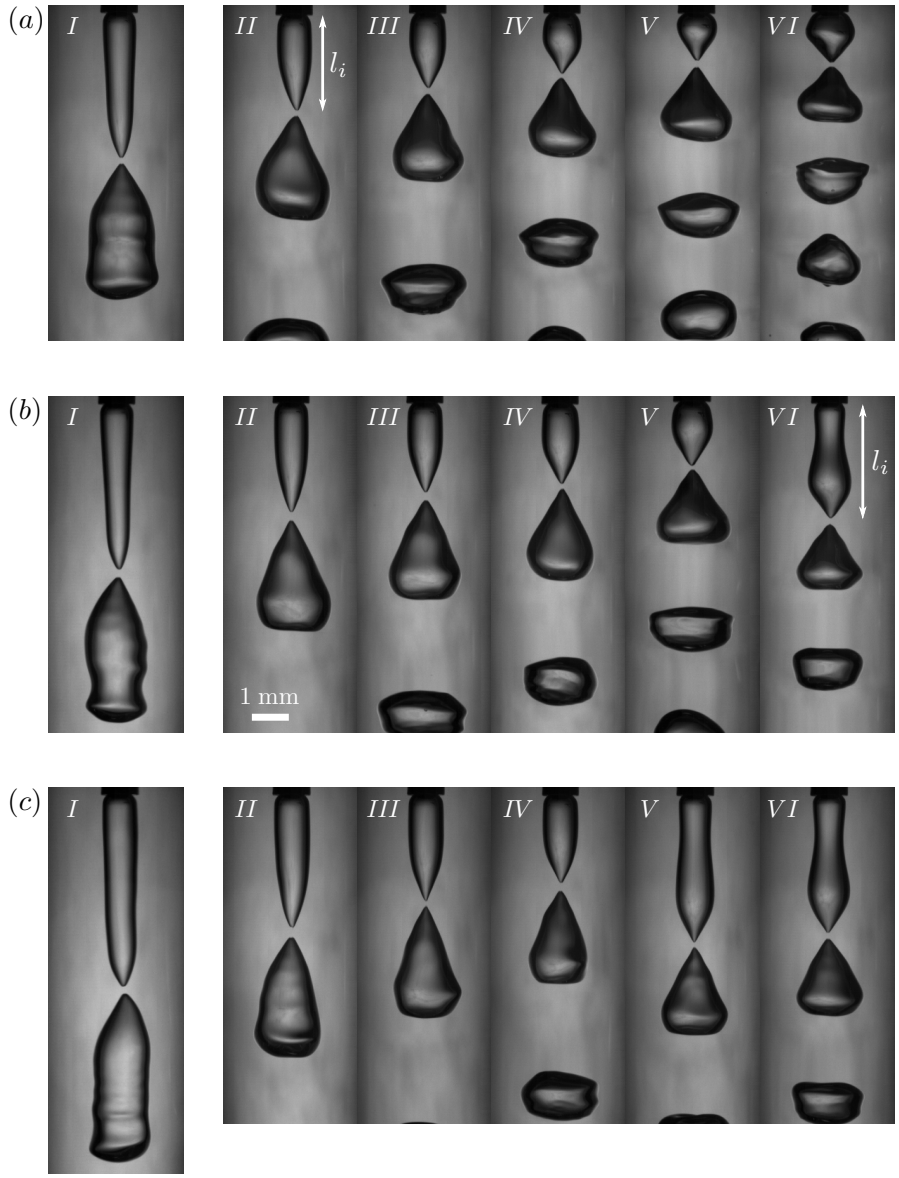

Figure 3.2: Snapshots of different bubbling regimes just after bubble pinch-off. The selected flow conditions, u_a = 2.22 m/s and (*a*) u_w = 1.53 m/s, (*b*) u_w = 1.70 m/s and (*c*) u_w = 1.86 m/s, give rise to the natural bubbling frequencies f_n = 182; 186 and 195 Hz, respectively, corresponding to the unperturbed case represented in the first image of each row (*I*). The rest of the images show forced cases of the corresponding natural regime, (*II*) f_f = 250 Hz, (*III*) f_f = 300 Hz, (*IV*) f_f = 350 Hz, (*V*) f_f = 400 Hz and (*VI*) f_f = 450 Hz. The scale bar is 1 mm long, indicating the spatial resolution of all the shown snapshots.

3.2.2 Experimental methods

The experiments were conducted following a procedure similar to that described in Ruiz-Rus *et al.* (2017). Firstly, the unperturbed axisymmetric air-water co-flowing jet was generated by setting both the mean air and water flow velocities, u_a and u_w. This gives

rise to a natural bubbling regime generating bubbles at a certain frequency, f_n, from the pinch-off position, l_i (see snapshots *I* in figure 3.2). Then, each natural case was forced by imposing a pressure modulation at a desired forcing frequency, larger than the natural one, $f_f > f_n$. For each value of f_f, the forcing amplitude was slowly and monotonically increased until a synchronized and periodic bubble generation at the forcing frequency was achieved (see snapshots *II-VI* in figure 3.2), attending to the criteria established in Sect. 3.2.3. The same procedure was followed for increasing values of f_f and all the natural cases investigated. Finally, measurements were performed by combining high-speed visualizations with a backlighting technique. To that aim, images of the whole growing bubble interface were recorded with a Photron high-speed camera at frame rates from 37 500 f.p.s. with a resolution of 192 × 576 pixels to 45 000 f.p.s. with a 192 × 480 pixel resolution. A shutter speed of around 8.5 μs was sufficiently fast to avoid blurred profiles even at the extremely fast bubble pinch-off event. Spatial resolutions between 23 and 40 μm/pixel were achieved using a Sigma 105 mm macro lens, depending on the size of the field of view used to simultaneously capture both the entire intact air ligament and the whole detached bubble silhouette at the pinch-off instant. In addition to the recorded high-speed images, the instantaneous air pressure inside the chamber, $p_c(t)$, was registered with an acquisition rate ten times larger than the image recording frame rate. The images and the pressure signal were synchronized through a data logger system.

Each registered image of the forming bubble was digitally analyzed using an in-home developed two-step interface detection routine, similar to that described by Hijano *et al.* (2015). Firstly, a rough detection of the edges of the needle tip and of the attached forming bubble is performed at the pixel level. Given the non-uniformity of the background gray level (see e.g. figure 3.2), the global binarization-threshold methods resulted inadequate (González & Woods, 2002). Therefore, an edge detection method based on the local gray level gradient was developed. More precisely, the location of the pixels probably corresponding to the water-air interface were obtained by means of the Canny algorithm (Canny, 1986). Secondly, the accuracy of the detected contour was improved to the sub-pixel level. To that aim, a local threshold criterion was implemented by fitting a sigmoid function to the gray intensity level along the axis normal to the edge at each point of the interface (Song & Springer, 1996). More detailed information regarding the local threshold selection and the smoothing of the obtained interface can be found in Vega *et al.* (2009).

The bubble contour detected in each frame allowed to obtain the instantaneous volume of the growing air cavity attached to the injector, under the assumption of axisymmetry, as $V(t) = \int_0^{z_t} \pi D^2(z,t)/4 \, dz$. Here, $D(z,t)$ denotes the diameter of the interface obtained from the image, z is the axial coordinate measured from the injector tip, and z_t represents the bubble tip, defined as the downstream position at which the interface diameter becomes zero. Figure 3.2 represents the time evolution of the growing cavity volume obtained from

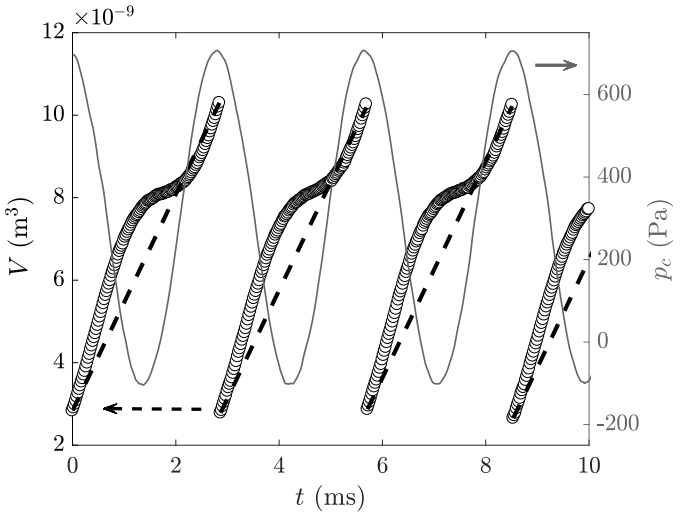

Figure 3.3: Time evolution of the bubbling process established for u_a = 2.22 m/s and u_w = 1.70 m/s, forced at f_f = 350 Hz, corresponding to figure 3.2*bIV*. (left vertical axis) Symbols represent the instantaneous volume of the forming bubble extracted from the image analysis. The bubble detachment appears as an abrupt decrease of the detected volume between two time steps. Notice that, due to the induced pressure variations at the feeding chamber, the measured volume substantially differs from that corresponding to the unperturbed constant flow rate conditions (dashed line). (right vertical axis) The solid line indicates the pressure registered at the feeding chamber, showing a nearly sinusoidal shape at the selected forcing frequency, f_f.

the images (left vertical axis), together with the synchronized chamber pressure signal (right vertical axis), for the experimental flow conditions u_a = 2.22 m/s and u_w = 1.70 m/s, forced at f_f = 350 Hz. The symbols in figure 3.2 show the experimental volume growing from the initial air lump that remains attached to the injector once the previous bubble pinches-off, referred to as the *intact ligament*. It can be observed that, as an effect of the forcing process, the volume evolution during the bubbling cycle is quite different from that which would take place under constant air flow rate conditions, depicted by dashed lines in figure 3.2. A detailed account of the natural bubbling process at constant flow rate conditions can be found in Sevilla *et al.* (2005*a*); Gordillo *et al.* (2007). At the end of the bubbling cycle, the volume of the detected cavity attached to the injector, abruptly decreases to reach the volume of the intact ligament, indicating the detachment of a bubble and the beginning of a new cycle. The axial position at which the pinch-off occurs is the *intact length*, l_i, defined as the value of z_t at the first frame of each cycle. Under periodic bubbling conditions, the time elapsed between two consecutive bubble detachments is just the inverse of the bubbling frequency f_b. In addition, the volume of the generated bubble, V_b, is obtained as the difference between the volume measured at the last frame of the cycle and that of the corresponding intact ligament. Moreover, the amplitude of the induced chamber pressure variation Δp_c, has been obtained by computing the mean value of the pressure signal envelope obtained through a Hilbert transform, as

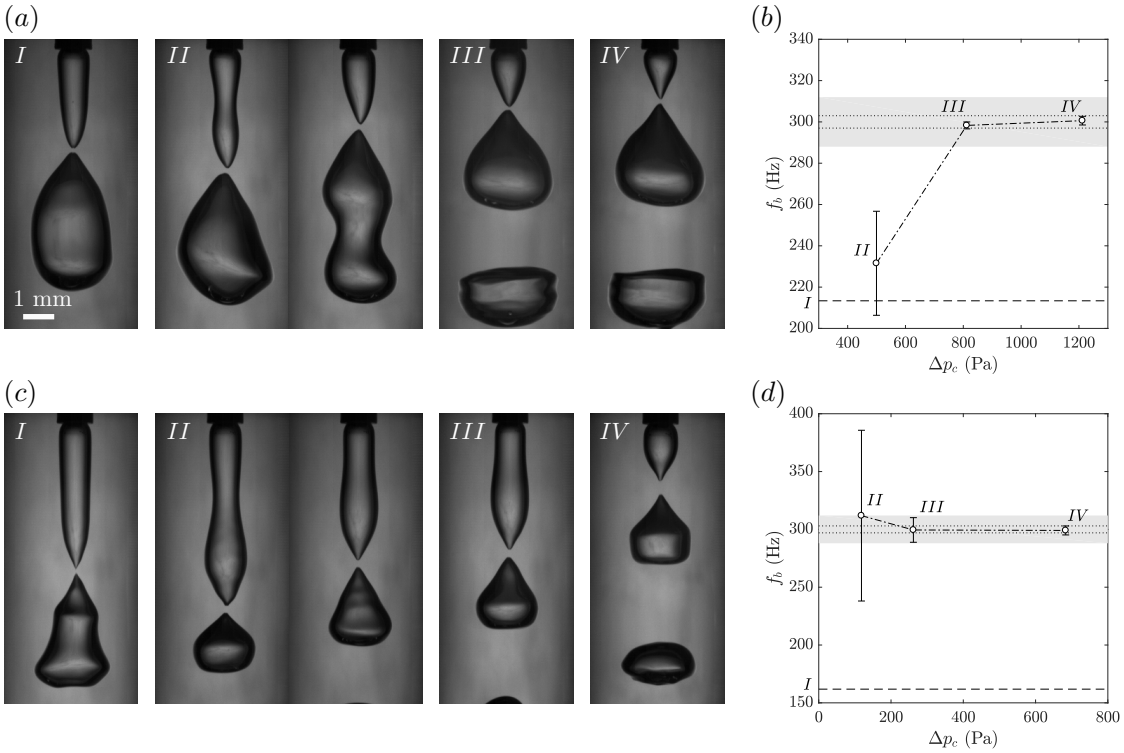

Figure 3.4: (a) Experimental images of the instant just after the bubble pinch-off for the flow conditions $u_a = 3.80$ m/s and $u_w = 1.36$ m/s corresponding to the natural case, $f_n = 213$ Hz (I), and forced cases with increasing pressure amplitude at 300 Hz $(II\text{-}IV)$. (b) Mean bubbling frequency of forced cases in (a) as a function of the pressure amplitude measured in the chamber, whose associated standard deviation is plotted with error bars. The natural bubbling frequency is indicated with a dashed line. The range of admissible values of the mean bubbling frequency and its standard deviation, attending to the effectiveness criteria, are depicted as dotted lines and as a shaded region, respectively. The snapshots in (II) correspond to two consecutive bubble detachments of an experiment that is forced with a non-effective amplitude. Effective forcing processes under the present conditions exhibit the so-called breakup mode M1, being the corresponding critical amplitude represented in (III), while a larger value is shown in (IV). (c, d) Same as (a, b) but for a case with $u_a = u_w = 1.36$ m/s, $f_n = 162$ Hz. Under these conditions, the critical pressure amplitude leads to an effective forcing process which responds in the breakup mode M2 (III). For amplitudes larger than the critical one, although effective, the forcing process departs from M2 (IV).

described in Jiménez-González & Huera-Huarte (2017). Finally, the averaged values of l_i, f_b and V_b, as well as their standard deviation, were obtained by analysing a minimum of 20 bubbling events for each selected value of the forcing amplitude Δp_c.

3.2.3 Experimental procedure: criteria to determine the effective forcing amplitude

The experimental procedure described in the previous section implies that only those forced cases leading to synchronized bubble generation at the selected frequency, are considered in the present work. Those situations, denoted as *effective* from now on, are

achieved if the forcing amplitude is sufficiently large, a value that depends on the unperturbed flow conditions as well as on the forcing frequency. The minimum pressure amplitude required to achieve an effective forcing process will hereinafter be called the *critical amplitude*. For amplitudes smaller than the critical one, the forcing is not able to properly control the bubble generation process. Therefore, to clearly distinguish between both situations, the bubbling regimes established for each selected value of Δp_c, were analyzed following an effectiveness criterion based on the measured bubbling frequency, as described in detail below. At this point, it should be mentioned that, depending on the flow conditions and on the forcing frequency, two different forced bubbling regimes were found, that were called breakup modes M1 and M2, respectively (see e.g. snapshots (a)*II-VI*; (b)*II-V* and (c)*II-IV* for M1, as well as (b)*VI* and (c)*V-VI* for M2, in figure 3.2). Briefly stated, mode M1 is characterized by the periodic formation of bubbles at a distance from the injection needle smaller than one perturbation wavelength, while mode M2 is characterized by the formation of bubbles at a larger distance, featuring the presence of more than one local maximum of the interface diameter at the instant of pinch-off. Both modes are effective for amplitudes larger than the corresponding critical ones, giving rise to the emission of monodisperse bubbles at the selected forcing frequency. However, their characteristic features, as well as the way in which the bubble pinch-off takes place, differ substantially. A detailed description of the dynamics involved in each mode can be found in Sect. 3.3.1.

Figure 3.4 illustrates the procedure followed to find the critical amplitude. To that end, the effectiveness criterion explained in the previous paragraph was applied to different forcing processes with equal forcing frequency, f_f = 300 Hz, and increasing pressure amplitude. Two different flow conditions, u_a = 3.80 m/s, u_w = 1.36 m/s (figure 3.4a, b) and $u_a = u_w$ = 1.36 m/s (figure 3.4c, d), will be discussed. For amplitudes above the critical one, the former case generates bubbles under mode M1 (see snapshot *III* in figure 3.4a) while, in the latter case, the bubbling regime is M2 (see snapshot *III* in figure 3.4b). As anticipated above, for a forcing condition to be considered effective, the values of the mean bubbling frequency and its standard deviation obtained for each selected pressure amplitude, should be within the limits established by the effectiveness criterion. More precisely, a variation of $\pm 1\%$ around the target forcing frequency is accepted for the mean bubbling frequency, while a standard deviation less than 4% results acceptable. It is worth pointing out that the ranges of admissible values established for the criteria have been selected attending to the characteristic fluctuations observed under natural bubbling conditions. Figure 3.4(b, d) represents with symbols the mean bubbling frequency obtained under the imposed pressure amplitude, being the standard deviation plotted as error bars. The initial unperturbed bubbling frequency is marked with a dashed line, corresponding to the natural case (see snapshots *I* in figure 3.4). The ranges established by the effectiveness criteria for the values of the target bubbling frequency and the acceptable standard deviation

are depicted as dotted lines and as a shaded region, respectively.

Specifically, the critical pressure amplitudes for all the experimental flow conditions, forced at different frequencies, were found following the steps described below for the conditions presented in figure 3.4(a, b). We started from the flow conditions $u_a = 3.80$ m/s and $u_w = 1.36$ m/s, establishing the unperturbed bubbling regime (figure 3.4aI), which leads to a natural bubbling frequency of $f_n = 213$ Hz. Then, we set the desired forcing frequency, $f_f = 300$ Hz in this case, and the critical forcing amplitude was searched by increasing the pressure amplitude in small steps. If the forcing amplitude is not sufficiently large, the imposed pressure fluctuations lead to an ineffective forcing that is not able to impose the forcing frequency for the bubbling process, producing polydisperse bubbles, as can be seen in figure 3.4(aII). This ineffective amplitude, $\Delta p_c = 500$ Pa, induces a bubbling frequency out of the ranges established by the effectiveness criteria (point II in figure 3.4b). If the amplitude is slowly increased, it reaches a certain value, $\Delta p_c = 812$ Pa in the case at hand, for which both the mean bubbling frequency and the standard deviation satisfy the effectiveness criteria, leading to the periodic emission of monodisperse bubbles at the forcing frequency (figure 3.4$aIII$). This pressure amplitude corresponds to the critical one, and the associated breakup mode can be identified from the images, according to the intact ligament characteristics that shall be defined in Sect. 3.3.1. If the amplitude is further increased (figure 3.4aIV), the forcing remains effective, presenting a forced bubbling regime similar to that obtained at the critical amplitude, but generating bubbles closer to the needle exit.

Generally, the steps describe in the previous paragraph were followed for all the forced experimental cases, including the conditions leading to forced bubbling regimes under the M2 breakup mode (see figure 3.4c, d). However, as explained in detail below, the M2 regime is characterized by slender intact ligaments, similar to those obtained in the natural cases with high values of Λ. This fact turns the bubbling process more susceptible to noise disturbances in the liquid stream (Sevilla *et al.*, 2005b), leading to weak fluctuations of the bubbling frequency. The latter fact is confirmed by the slightly larger standard deviation obtained for the point (III) in figure 3.4(d). However, for amplitudes larger than the critical one, although still effective, the forcing process becomes more energetic and the fluctuations disappear as the bubbling regime experiences a transition from the M2 mode to the M1 mode (figure 3.4bIV), due the shortening of the intact length.

All the results presented hereafter were obtained for effective forcing processes at the critical pressure amplitude, since they represent the energetically optimal values of interest for possible applications.

3.3 Results for the effective forcing process

3.3.1 Description of the forced bubbling process within M1 and M2

The periodic bubble generation, naturally established under the unperturbed flow conditions, is driven by the inertia of the outer liquid stream (Rodríguez-Rodríguez *et al.*, 2015). In fact, it has been proven that the velocity at which the growing bubble interface is transported during the bubbling cycle, is imposed by the co-flowing liquid (Sevilla *et al.*, 2005*a*). Moreover, the characteristics of the air feeding system used in this study, induce a bubble formation process with an air flow rate from the constant pressure chamber to the forming bubble that varies with time, in the absence of the speaker actuation (Kumar & Kuloor, 1970; Gordillo *et al.*, 2007). Under these particular feeding conditions, the flow resistance, i.e. the pressure drop along the injection needle, plays an essential role during the initial stages of the bubble formation (Oğuz & Prosperetti, 1993; Gordillo *et al.*, 2007), being the latest ones characterized by the decrease of the air pressure inside the bubble (Sevilla *et al.*, 2005*a*). The main aspects of the unforced bubbling cycle are briefly described as follows. Further details about the dynamics of the bubble formation under constant pressure feeding conditions can be found elsewhere (Gordillo *et al.*, 2007). The overall natural bubble formation process involves two different stages, namely the *expansion* and the *collapse* stage, respectively. Once a bubble detaches from the intact ligament, a large pressure pulse inside the ligament induces radially outward velocities to the surrounding liquid, starting the expansion stage of a new bubble. As the bubble rapidly grows, its pressure decreases with time decelerating the liquid surrounding the bubble. In fact, at the end of the expansion stage, the bubble pressure has dropped below that of the liquid, inducing an inward acceleration of the liquid toward the axis and causing the formation of a neck at the interface. At this moment, the collapse stage begins, which eventually results in the bubble pinch-off. The very latest instants of the collapse, with part of the air feeding area flowing through the neck, has been observed to be governed by the Bernoulli suction effect (Gordillo *et al.*, 2005; Dollet *et al.*, 2008; Bergmann *et al.*, 2009; Gekle *et al.*, 2010).

On the other hand, under the effective forcing process, the pressure inside the feeding chamber varies during the bubbling cycle (see e.g. figure 3.3). This effect can be interpreted as an active actuation on the feeding line flow resistance which induces an artificial modulation of the air flow rate towards the bubble, $Q_a(t)$, boosting the natural mechanisms that drive the bubble formation process and, thus, imposing the desired bubble formation frequency, f_f. Figure 3.5 shows the temporal evolution of the growing bubble interface for a complete bubbling cycle under the effect of the critical pressure amplitude for two different flow conditions, i.e. $u_a = 3.80$ m/s and $u_w = 1.36$ m/s in figure 3.5(a) and $u_a = u_w = 1.36$ m/s in figure 3.5(b), both forced at $f_f = 300$ Hz. The figure shows that the bubbling process in figure 3.5(a) responds to the breakup mode M1 while that in fig-

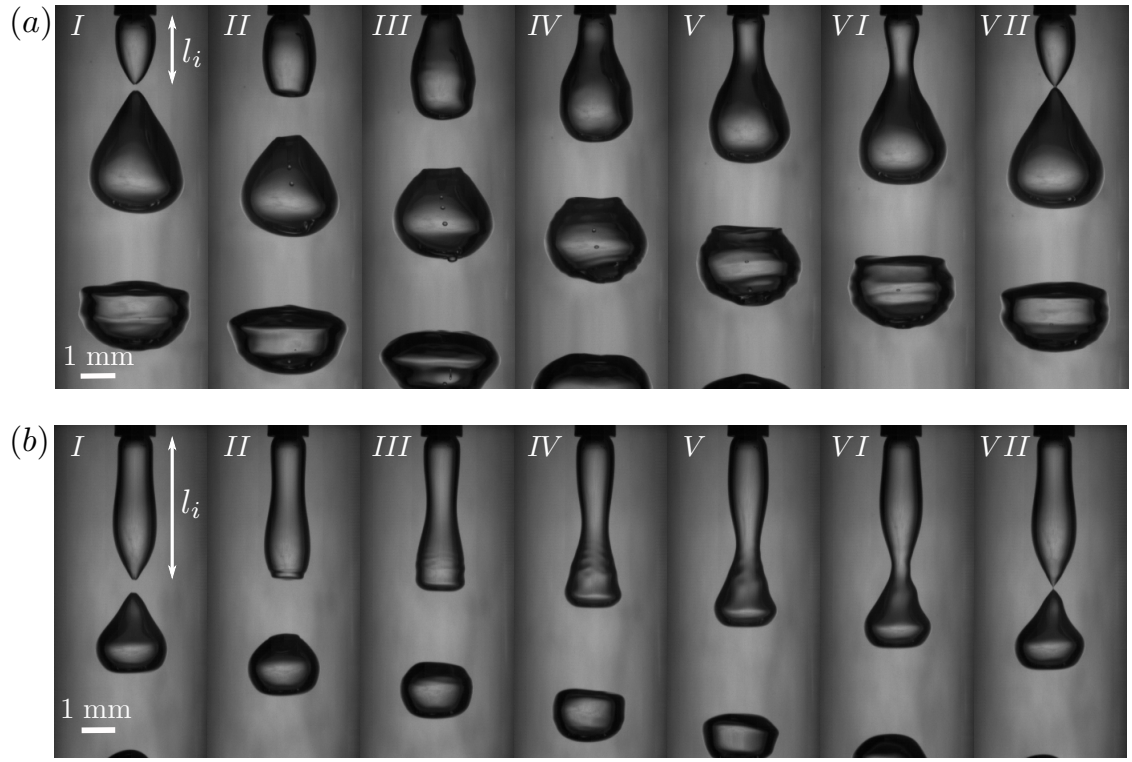

Figure 3.5: Sequence of experimental images showing the temporal evolution of the growing bubble during an effective forcing cycle. The represented cases include the same flow conditions as in figure 3.4(a, c), respectively, forced at f_f = 300 Hz under the corresponding critical pressure amplitude. The obtained forced bubbling regimes exhibit two different breakup modes, (a) mode M1 and (b) mode M2, respectively. The time interval between the snapshots is 0.56 ms for both cases.

ure 3.5(b) exhibits the mode M2. As mentioned in the previous section, it can be inferred from the temporal evolution of the bubble interface in both modes, that the mechanisms leading to the formation of the neck which eventually collapses, result different, as shall be described below.

The bubble formation within the so-called breakup mode M1 (figure 3.5a) clearly resembles that previously described for the natural bubbling regime. Indeed, it exhibits an expansion stage during which the intact ligament rapidly inflates (figure 3.5aII). It is important to notice that, during this initial stage, the growing air cavity is not convected downstream by the outer co-flowing liquid stream, remaining attached to the needle tip, as occurs during the formation of bubbles in a quiescent liquid pool (Oğuz & Prosperetti, 1993). However, as the bubble pressure decreases, the surrounding liquid is radially decelerated. Eventually, the pressure difference induces an inward acceleration of the liquid, reducing locally the outward radial velocity of the bubble interface and giving rise to the collapse stage (figure 3.5$aIII$). At this moment, the interface at the injector exit becomes parallel to the needle, and the growing air cavity begins to move downstream, gener-

ating an incipient neck between the new growing air ligament and the forming bubble (figure 3.5*aIV*). During this collapse stage, the neck travels downstream approximately at the water velocity and, at the same time, it accelerates towards the symmetry axis (figure 3.5*aV, VI*). At the end of the cycle (figure 3.5*aVII*), the neck collapses, detaching a bubble from the tip of the intact ligament, whose final length is l_i (figure 3.5*aI*). The effective nature of the forced bubbling implies that the time at which the pinch-off occurs is imposed by the forcing frequency, $1/f_b = 1/f_f < 1/f_n$. Taking into account that the intact ligament moves downward at the water velocity only after the end of the expansion stage, the intact length in the forced case, $l_f = l_{i,f}$, results shorter than the induced perturbation wavelength, $l_f < u_w/f_f$, as shall be carefully checked in the next section. A similar behaviour is observed in the natural cases, being the intact length in these cases, $l_n = l_{i,n}$, smaller than the corresponding naturally induced perturbation wavelength, $l_n < u_w/f_n$. Therefore, it can be stated that the forced bubbling process within mode M1 is essentially an enhanced counterpart of the natural case, being both stages assisted by a pressure modulation that results in a faster bubbling process.

With respect to the forced bubbling regime established under the breakup mode M2 (figure 3.5*b*), the involved dynamics results completely different from that described for both the natural regime and mode M1. The main aspect that can be observed in the time evolution of the growing interface, concerns the time taken by the neck to form and to grow until it collapses. In fact, when a bubble is detached (figure 3.5*bI*), the interface of the intact ligament is already perturbed, showing a deflection between the injector and the tip of the ligament, which corresponds to the forming neck. Although, similarly to the other situations, such neck travels downstream at the water velocity while it grows toward the axis (figure 3.5*bII-IV*). However, in mode M2, as it will be shown later, the intact length results larger than the induced perturbation wavelength, $l_f > u_w/f_f$. It is worth highlighting that, although the initial expansion stage does not take place in mode M2, the interface perturbs itself, induced by an inflation of the ligament. This perturbation leads to the formation of the neck (figure 3.5*bII*) and a subsequent local inward acceleration until it pinches off (figure 3.5*bIII-VI*). This implies that, contrary to what happens in mode M1 and the natural cases, the overpressure leading to the interface expansion in mode M2 is not related to the previous bubble pinch-off, but it is induced by the pressure perturbation created by the forcing process. Therefore, although the bubbles are emitted at the selected frequency, they take more than a forcing wavelength to grow up and detach. That is, in mode M2 there are more than one perturbation wavelength acting in the air ligament simultaneously. In addition, as shall be analyzed in detail in the following sections, the necessary conditions for bubble production within mode M2 typically involve lower air flow rates than those required within mode M1 for equal demanded frequencies under similar co-flowing liquid velocities. These particular conditions lead to smaller values of the required critical pressure amplitudes, as can be checked in figure 3.4(b, d), even

considering that the obtained forced bubbling frequencies result much larger than those naturally established.

3.3.2 Intact length and bubble volume

It has been stated from previous sections that the position at which the bubble pinch-off occurs, generically denoted as l_i, represents the distance traveled by the neck from the needle tip until the position at which it collapses. Since for the natural and mode M1 cases, it has been shown that the intact ligament does not grow axially during the expansion stage, the time elapsed between both positions coincides therefore with the duration of the collapse stage. However, in the breakup mode M2 the neck is formed during the previous bubbling cycle, leading to a larger travel time, and thus, increasing the intact length. Therefore, in the natural case and in both forced regimes, l_i highly depends on the bubbling frequency, f_b, and on the travel velocity, which corresponds with the co-flowing water velocity u_w. These dependencies can be seen in figure 3.6(a, c, e, g), where the measured intact lengths for the natural cases as well as for both forced regimes are represented as a function of the air velocity for the different experimental values of the velocity of the co-flowing water stream and forcing frequencies.

Let firstly focus on the natural bubbling regimes, represented by black stars (★). It can be observed that, for a constant value of the analyzed water velocities, the intact length decreases as the air velocity increases. In these cases, the bubble pinch-off takes place closer to the injector exit due to the increment of the naturally established bubbling frequency, as already reported by (Sevilla *et al.*, 2005a) for constant flow rate feeding conditions and (Gordillo *et al.*, 2007) for constant injection pressure conditions. On the other hand, an increase of the intact length with the water velocity is also observed (see, in addition, snapshots I in figure 3.2). For the range of water velocities studied in the present work, the effect of the convective velocity at which the neck is transported downstream is more relevant than the slight increment in the breakup frequency, resulting in an increase in the intact ligament (for details about this outer velocity-induced frequency increment see Rodríguez-Rodríguez *et al.* 2015 and references therein).

Regarding the results for the forced bubbling regime within mode M1 (hollow symbols), it is worth remembering that each unperturbed bubbling regime is forced at frequencies higher than the natural one, $f_f > f_n$, resulting therefore in smaller intact ligaments, $l_f < l_n$. In addition, for a given value of the surrounding water velocity, a slight decrease of l_f is observed with the air velocity for a constant imposed frequency. Moreover, since the mechanism driven the forced bubble detachment within mode M1 has been described as an accelerated process of the natural case, the pinch-off position decreases as the forcing frequency increases due to the reduction of the bubbling time, leading to shorter intact ligaments (see also figure 3.2a). Finally, the effect of the water velocity on the length of the intact ligament is simply associated to its effect on the neck traveling velocity, since

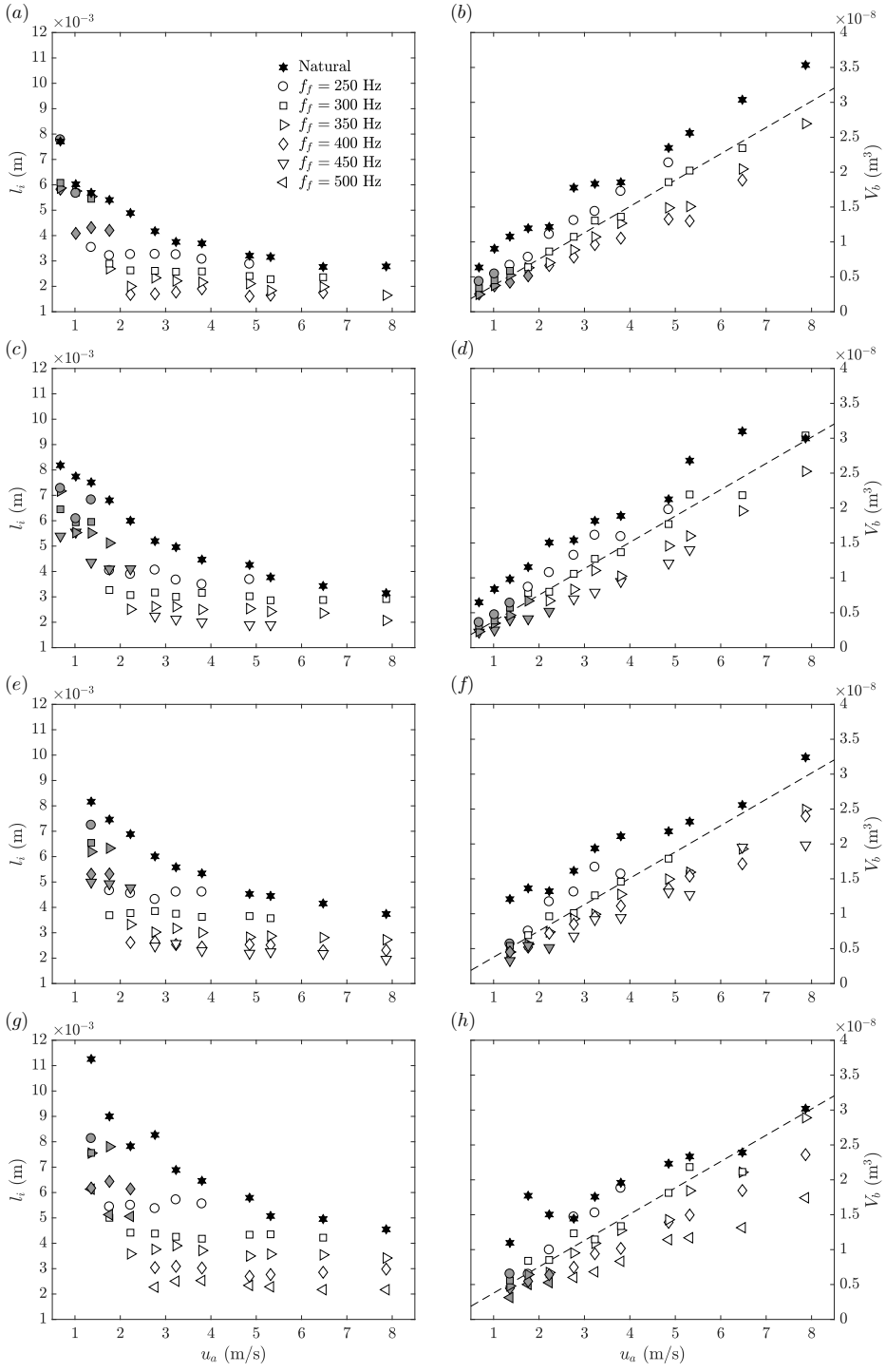

Figure 3.6: (a, c, e, g) Experimental intact length and (b, d, f, h) bubble volume obtained for forced bubbling regimes under the corresponding critical pressure amplitude as a function of the air velocity for different forcing frequencies and (a, b) $u_w = 1.36$ m/s, (c, d) $u_w = 1.53$ m/s, (e, f) $u_w = 1.70$ m/s, (g, h) $u_w = 1.86$ m/s. For clarity, only some forcing frequencies have been represented for each water velocity. Hollow symbols correspond to breakup mode M1, while gray ones are the results for breakup mode M2. Black stars represent the natural bubbling cases. The dashed line is the function $V_b = \pi r_o^2 u_a / f_f$, being thus the slope of the line $\pi r_o^2 / f_f$ with $f_f = 300$ Hz.

the bubbling frequency is prescribed by the forcing process (see also snapshots *II*, *III* and *IV* in figure 3.2).

Regarding mode M2, a different behaviour is observed in the intact lengths, although trends similar to those observed in mode M1 are found. Generally, the intact ligament increases with the water velocity (see, in addition, snapshots *VI* in figure 3.2b, c), decreases with the bubbling frequency (see, in addition, snapshots *V* and *VI* in figure 3.2c), being the influence of the air velocity nearly negligible. However, as explained before, the M2 intact lengths are substantially larger than those obtained within mode M1 for the same forcing frequencies (see, in addition, snapshots *I* in figure 3.5), since the neck is already formed in the previous forcing cycle and, as already mentioned, there is not expansion stage. It is important to notice that the forced intact lengths, even for mode M2, are always smaller than those corresponding to the natural, unforced cases.

The evolution of the volume of the bubbles generated under the natural bubbling regimes with the injected air velocity for the four experimental water velocities is displayed in figure 3.6(b, d, f, h) with black stars. In this figure the bubble volume, V_b, has been obtained analyzing digitally the images of the forming bubbles using the experimental procedure described in Sect. 3.2.2. An increase of V_b with the air velocity, u_a, is observed, according to $V_b = \pi r_o^2 u_a / f_b$ (Rodríguez-Rodríguez *et al.*, 2015), since the bubbling frequency increases more slowly than the air velocity at a constant water velocity (Sevilla *et al.*, 2005a). Taking into account the reduced range explored in the present work, the dependence with the water velocity is barely observed. In addition, the volume of the generated bubbles under both forced regimes at different frequencies, is plotted in the same figure (hollow symbols for M1 and gray ones for M2). Given the synchronization of the bubble generation with the air flow rate modulation, periodically induced by the forcing process (see Sect. 3.2.3), a linear dependence with the air velocity is obtained for constant values of the water velocity. This linear dependence with the air velocity can be confirmed through the dashed lines plotted in figure 3.6(b, d, f, h), which represent the function $V_b = \pi r_o^2 u_a / f_f$ for $f_f = 300$ Hz. The good agreement between the experimental data measured at $f_f = 300$ Hz (hollow squares) and the linear function, confirms that $V_b = Q_c / f_f$, being Q_c the air flow rate constantly injected in the feeding chamber. Moreover, since the bubbling frequency is imposed by the forcing process, the obtained bubble volume is not influenced by the water velocity. In order to fully confirm the previous statements for all the forcing frequencies, figure 3.7(a) shows the experimentally obtained values of the bubble volume as a function of the control parameters, Q_c and f_b, made dimensionless with πr_o^3. Here, the bubbling frequency f_b represents both forced and natural frequencies, $f_{b,n} = f_n$ and $f_{b,f} = f_f$, respectively, since the results for the natural cases (colored stars) have been included as well. The natural bubbling frequency has been extracted from the image analysis. Only the results for the lowest and the largest values of the experimental water velocities, $u_w = 1.36$ and 1.86 m/s respectively, are plotted for

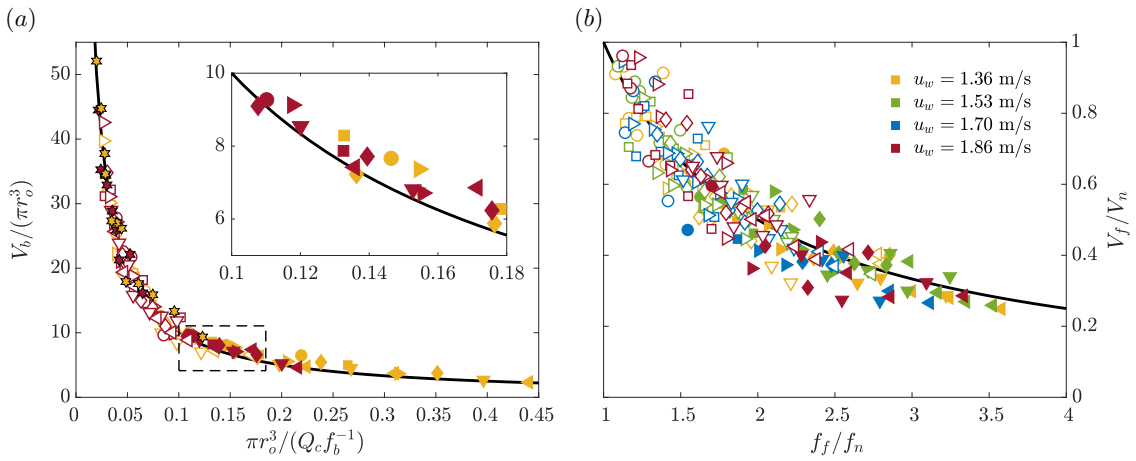

Figure 3.7: (a) Dimensionless bubble volume obtained from the image analysis as a function of the dimensionless total volume injected to the feeding chamber under a constant flow rate in the bubbling cycle. The stars denotes the results for the natural cases, the rest of the symbols indicate the different forcing frequencies. (b) Forced-to-natural bubble volume ratio as a function of the forcing frequency ratio for all the experimental forced cases. The solid line represents the function $V_f/V_n = f_n/f_f$. Forced bubbling events corresponding to mode M1 are represented by hollow symbols, while those associated to mode M2 are plotted with solid one. Different colors indicates the experimental water velocities. For the sake of clarity, in (a) only the results for the lowest and the largest values of the water velocities, $u_w = 1.36$ and 1.86 m/s, respectively, are shown. The inset in (a) is a zoomed representation of the region highlighted by the dashed frame, in which only data from mode M2 has been plotted, showing the values at which M2 appears for each water velocity condition.

clarity. It can be observed that the dimensionless bubble volume for all the natural and the forced cases decreases with the dimensionless frequency. In fact, they are inversely proportional, and all the experimental measurements are confirmed to collapse on the curve $V_b = Q_c/f_b$, represented by a solid line. An important feature which can be clearly seen in figure 3.7(a) is that the forced bubbling events corresponding to mode M2 (solid symbols) lead to much smaller bubble volumes than those corresponding to mode M1 (hollow symbols), since M2 typically involves flow conditions associated to lower air velocities. Indeed, mode M2 allows the production of very uniform bubbles even smaller than the smallest ones achieved in the natural regime, whose lower air velocity values are constrained by the transition to the jetting regime (Sevilla *et al.*, 2005*b*). This fact, together with the low values of the critical pressure amplitude required for the effective bubbling process (see Sects. 3.2.3 and 3.3.1), make the mode M2 highly interesting for practical applications.

As happens to the intact length, the forcing process always increases the bubbling frequency over the natural one, reducing the volume of the generated bubbles (figure 3.6b, d, f, h) while keeping, or even increasing, the degree of the monodispersity (see Sect. 3.2.3). In this sense, the performance of the present forcing mechanism over the experimental range covered in this work, is summarized in figure 3.7(b), in terms of the achieved bubble volume reduction, V_f/V_n, under the imposed frequency ratio, f_f/f_n. Here, $V_f = V_{b,f}$ and

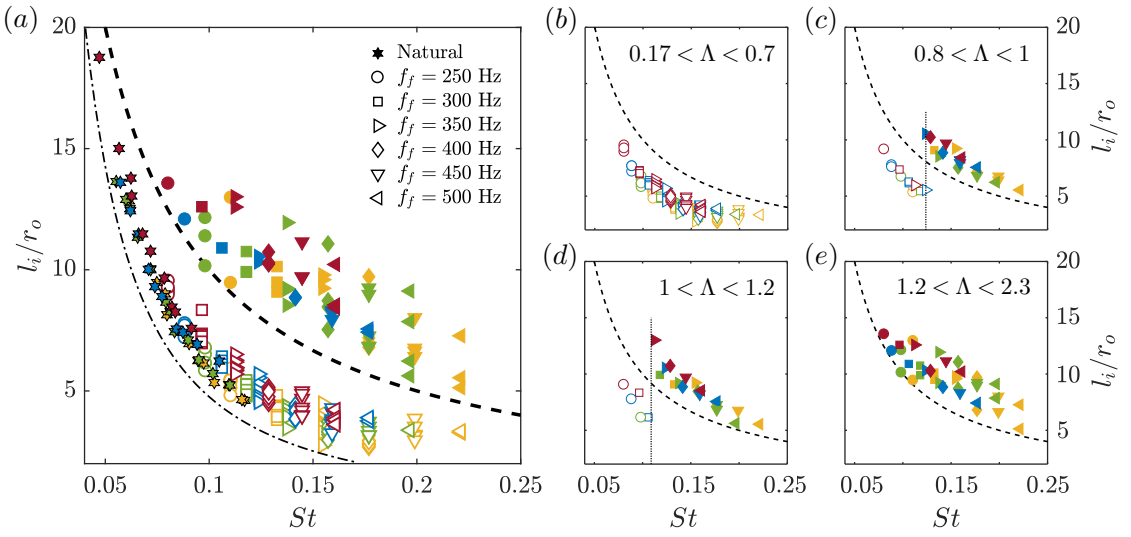

Figure 3.8: Dimensionless intact length as a function of the dimensionless bubbling frequency, defined as the Strouhal number, $St = f_b r_o/u_w$. Different colors indicate the experimental water velocities, as indicated in figure 3.7. Results for the natural bubbling regimes are represented as colored stars and the experimental data from the breakup modes M1 and M2 as hollow and solid symbols, respectively. The dashed line represents the dimensionless perturbation wavelength, defined as the dimensionless intact length that would result if the neck would appear just at the beginning of the cycle and it would travel downstream at the water velocity during the whole bubbling cycle, $l_i/r_o = St^{-1}$. (*a*) Results for all the experimental data, including the natural cases. The thinner dashed-dotted line is a function $l_i/r_o \sim St^{-8/5}$ (see main body in Sect. 3.4). (*b-e*) Results for different ranges of Λ. The thinner, vertical, dotted lines point out the approximate value of St at which the transition between the modes takes place.

$V_n = V_{b,n}$ represent the bubble volume of the forced and natural cases, respectively. It can be observed that the volume reduction is equivalent to the frequency ratio, confirming the results previously shown. In addition, depending on the value of the established unperturbed flow conditions and according to the forcing frequency, the volume of the generated bubbles can be reduced up to 80% of the initial natural ones. As mentioned above, the maximum reduction is accomplished by the forced bubbling regimes within mode M2.

3.3.3 Necessary conditions for the forced bubbling process corresponding to mode M2

In order to qualitatively explore the conditions under which the forcing process leads to bubble production within the breakup mode M2, it can be firstly stated from the experimental images shown in figure 3.2, that they depend on the air and water velocities, as well as on the demanded forcing frequency. More precisely, the frequency at which mode M2 is triggered varies with the unperturbed flow conditions. Therefore, it proves convenient to represent its dependence in compact form using dimensionless variables, namely Λ and St. In addition, it has been shown that M1 is characterized by the forced

intact length, l_f, shorter than the corresponding so-called perturbation wavelength, u_w/f_f, while in M2, $l_f > u_w/f_f$ (see Sect. 3.3.1). In this sense, figure 3.8(a) presents the measured dimensionless intact length, l_i/r_o, as a function of the dimensionless bubbling frequency, defined as the Strouhal number, $St = f_b r_o/u_w$, for all the experiments performed in this work, including the natural and the forced cases. It is worth mentioning again that, under the critical pressure amplitude, the bubbling frequency coincides with the forcing one, $f_f = f_{b,f}$. Although it shall be deeply analyzed in Sect. 3.4, we can anticipate that the intact length for the unperturbed cases monotonically decreases as a function of St with the same trend for all the analyzed values of the water velocity, distinguished in series with different colors in figure 3.8. Moreover, as stated before, the mechanisms leading to the neck formation are equivalent for both the M1 and the natural bubbling regimes, thus the forced intact lengths obtained for the mode M1 (hollow symbols) follow the same behaviour as that for the natural cases (stars). In fact, similar values of St give rise to similar intact lengths in both cases, confirming that M1 behaves as a natural case artificially assisted. Some data dispersion is observed due to the effect of the water velocity. An additional data dispersion appears for each forcing frequency showing the slight decrease of the forced intact length with u_a, previously noticed in figure 3.6(a, c, e, g). A clear distinction of the two different breakup modes can be seen in this figure. Indeed, intact lengths obtained from the natural bubbling regimes and from the break mode M1, lie below the dimensionless perturbation wavelength, $(f_b r_o/u_w)^{-1} = St^{-1}$, depicted as a dashed line. The difference reflects the fraction of the bubbling cycle spent on the initial expansion stage. On the other hand, intact lengths of forced bubbling events corresponding to mode M2 are larger than the perturbation wavelength, since the neck is formed during the previous bubbling cycle. Greater data dispersion is noticed for the M2 events, due to the slenderness of the ligament and the larger receptivity to noise disturbances. Therefore, it can be concluded that breakup mode M2 takes place under flow conditions which lead to intact ligaments longer than the induced perturbation wavelength, $l_n > \alpha u_w/f_f$, being $\alpha > 1$.

It is well known that the periodic bubble formation, naturally established for gas-liquid co-flowing jets, is associated with an absolute instability (Monkewitz & Sohn, 1988; Sevilla *et al.*, 2005*b*). However, as the water-to-air velocity ratio, Λ, increases, the absolute wavelength becomes larger, giving rise to bubble pinch-off further downstream from the injector. Therefore, larger values of Λ lead to larger intact ligaments, promoting the appearance of the breakup mode M2 under short enough forced perturbation wavelengths. This can be confirmed through figure 3.8(*b*-*e*), where the experimental forced results have been classified in different ranges of Λ. Notice that for the lowest range of Λ shown in figure 3.8(b), the bubbling events correspond to breakup mode M1 under the whole range of St analyzed (see, in addition, figure 3.2a). In this case, where the air velocity is considerable faster than the liquid velocity, the air stream is stopped by the co-flowing water stream when leaving the injector, expanding radially to accommodate the incoming

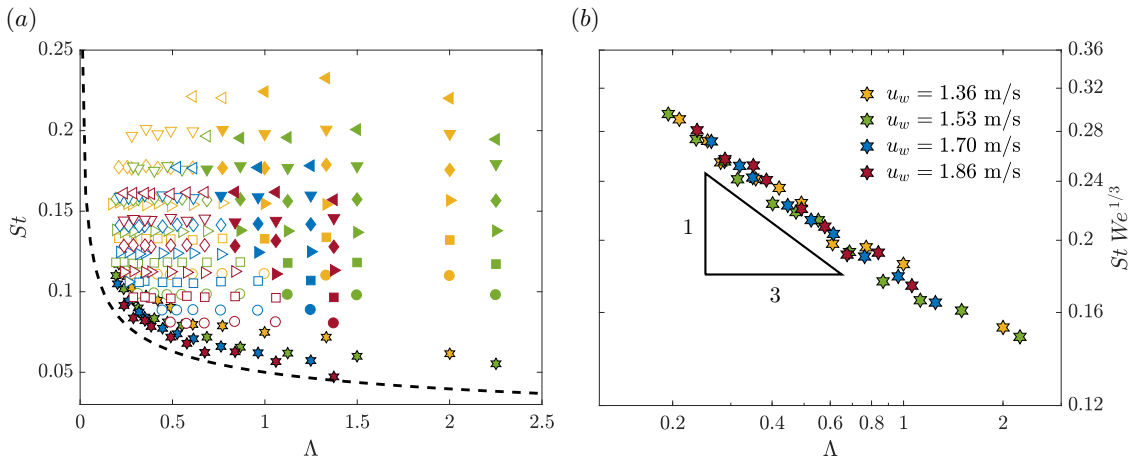

Figure 3.9: (a) Experimental bubbling events obtained in the present work in a $St - \Lambda$ plane. Results for the natural bubbling regimes are represented as colored stars and the rest of the symbols denote the different forcing frequencies, as indicated in figure 3.7. Hollow symbols indicate the results corresponding to breakup mode M1 and the solid ones to mode M2, respectively. The dashed line is a function $St \sim \Lambda^{-1/3}$ (see main body in Sect. 3.4). (b) Dimensionless bubbling frequency corrected by $We^{1/3}$ for the natural cases as a function of Λ represented in logarithmic scale.

gas flow rate. Thus, an expansion stage takes place before forming a neck near the needle exit, initiating the collapse stage. As Λ increases (figure 3.8c, d), the forced regimes respond either to mode M1 or mode M2, depending on the value of the induced St (see, in addition, figure 3.2b, c). In fact, there is a critical value of St, highlighted with vertical dotted lines in figure 3.8(c, d), at which a transition from mode M1 to mode M2 occurs. This critical Strouhal number decreases as Λ increases, confirming the previously mentioned relationship between the naturally established wavelength, associated to the water-to-air velocity ratio, and the forced perturbation wavelength, caused by the induced St. Finally, for large enough values of Λ (figure 3.8e), the forced bubbling process always takes place in mode M2 under the whole range of St analyzed here. In this case, the velocity of the water stream is similar than that of the air and, once it exits the injector, the gas flows parallel to the surrounding liquid, being the system convectively unstable. However, the gas jet breaks near the needle tip, but at distances from the exit larger than in the case of mode M1, due to the high amplitude perturbations introduced by the forcing system.

As mentioned above, figures 3.8(b-e), indicate that the critical frequency (or Strouhal number) for the transition between both forced breakup modes is a function of Λ. In fact, plotting all the experimental results in the $St - \Lambda$ plane (figure 3.9a), it can be seen that modes M1 and M2 occupy different regions in the parametric plane. Consequently, in order to clearly determine the transition between both modes, a detailed analysis of the results in figure 3.7(b) reveals the particular conditions at which the mode M2 is triggered. Indeed, noting that $\pi r_o^3/(Q_c f_f^{-1})$ can be rewritten as $St\Lambda$, the transition can be established as $St\Lambda \approx 0.1$, although the inset in figure 3.7(b) indicates that there is an

additional dependence on the water velocity, or similarly, on the Weber number, $We = \rho u_w^2 r_o/\sigma$, as shall be discussed in Sect. 3.4. Figure 3.9(b) shows the dimensionless frequency modified with the effect of the water velocity through We, as a function of Λ, as it shall be commented in next section.

3.4 Characterization of the air intact length and transition between breakup modes

The experimental results presented in the previous sections clearly demonstrate that, under the breakup mode M1, the bubble formation dynamics under forced conditions resembles the natural bubbling described in previous works in the absence of forcing (Sevilla *et al.*, 2005a; Gordillo *et al.*, 2007). Indeed, the bubbling time, imposed by f_f in the forced case, presents the same two consecutive stages observed in the natural bubbling process. Each stage establishes the conditions that periodically lead to the other one, being their duration dependent on the unperturbed flow conditions and, in the forced case, on both the imposed forcing frequency and amplitude. These dependencies imply that the imposed effective pressure modulation assists both stages, accelerating the process to achieve the forcing frequency. Moreover, it has been observed that the relative time spent on each stage can be characterized through the value of the intact length, that has been obtained experimentally (see Sect. 3.3). Therefore, similarly to the experimental forced-to-natural bubble volume ratio, both the natural and the forced M1 bubbling processes can be compared in terms of the ratio of the forced to natural intact lengths, l_f/l_n, for each imposed frequency ratio, f_f/f_n. Figure 3.10(a) shows that the experimental data nearly follows the function $l_f/l_n = f_f/f_n$, represented as a solid line. The latter result suggests that the mechanisms driving both forced stages are equivalent to those acting in the natural case, but working faster. Therefore, the intact lengths obtained in the forced cases can be characterized as a function of the control parameters through a comparison with their natural counterparts, making use of the relationship obtained in figure 3.10(a).

To that aim, let us first characterize the intact length obtained in the natural bubbling cases as a function of the unperturbed flow conditions. In dimensionless terms, as suggested by figure 3.9(a), for all values of the water velocity, the natural dimensionless bubbling frequency, $St = f_n r_o/u_w$, depends on Λ through a power law. Indeed, it has been found that, for each value of the water velocity (star symbols with different colors in figure 3.9a), St scales as $\Lambda^{-1/3}$, as evidenced by the dashed line in figure 3.9(a). The scatter observed among the data series associated with different water velocities may well reflect an influence of the Weber number (Sevilla *et al.*, 2005a; Gordillo *et al.*, 2007; Rodríguez-Rodríguez *et al.*, 2015). Indeed, the surface tension force contributes to accelerate the bubble neck collapse. Therefore, the dimensionless bubbling frequency obtained under the

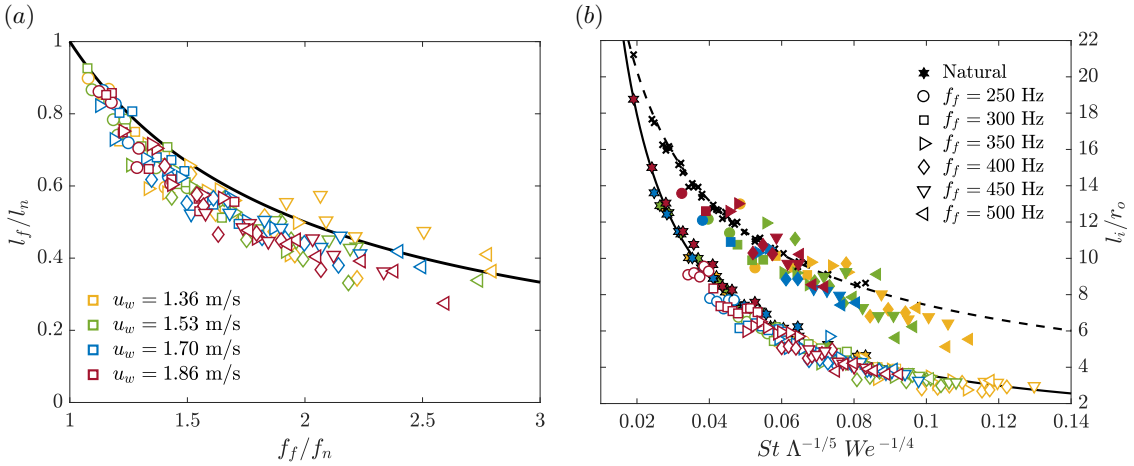

Figure 3.10: (*a*) Forced-to-natural intact length ratio as a function of the forced-to-natural frequency ratio for all the forced bubbling processes in the M1 breakup regime. The solid line represents the function $l_f/l_n = f_n/f_f$. (*b*) Dependence of the dimensionless intact length, l_i/r_o, on the dimensionless control parameters, namely the imposed frequency, St, and the flow conditions, specified by Λ and We, for all the experiments. The continuous line represents the dimensionless intact length obtained through equation (3.5). The black crosses denote the corresponding dimensionless wavelength of the natural cases, $u_w/(f_n r_o)$. The dashed line represents the dimensionless wavelength of an equivalent natural regime, given by Λ_q and We_q, such that the equivalent dimensionless frequency, St_q, is obtained through equation (3.4).

unperturbed flow conditions can be appropriately defined as

$$St \sim \Lambda^{-1/3}\mathscr{F}, \tag{3.1}$$

where $\mathscr{F} = \mathscr{F}(We)$ is an *a priori* unknown function of the Weber number. In a similar way, as previously mentioned in Sect. 3.3.3, the analysis of the dimensionless natural intact length, l_n/r_o, as a function of St, reveals a similar trend for each water velocity (star symbols with different colors in figure 3.8*a*), showing a weak dispersion among the different data series. In fact, it has been found that a power-law as a function of St with a exponent of $-8/5$ fits the experimental data fairly well for each value of the water velocity, as shown by the dashed-dotted line in figure 3.8(*a*). Thus, the dimensionless intact length can be conveniently expressed as

$$l_n/r_o \sim St^{-8/5}\mathscr{G}, \tag{3.2}$$

where $\mathscr{G} = \mathscr{G}(We)$ is an additional unknown function of the Weber number. A closer inspection of the experimental results leads to $\mathscr{G} \simeq We^{1/20}$, showing a very weak dependence of the intact length on the Weber number. In addition, the fact that the absolute value of the exponent of St is larger than unity, reflects the dependence of the relative time spent on both bubbling stages with the dimensionless bubbling frequency. Note that the latter result had been previously suggested by Sevilla *et al.* (2005*a*) and Gordillo

et al. (2007) for bubbling under constant air flow rate and constant feeding pressure conditions, respectively. For a given flow condition, defined by the values of Λ and We, as well as a dimensionless forcing frequency, $St = f_f r_o/u_w$, the dimensionless forced intact length, l_f/r_o can be characterized by including equations (3.1) and (3.2) into the expression $l_f/l_n = f_f/f_n$, deduced from figure 3.10(a). The resulting dimensionless intact length, either for the natural or the forced cases, scales as

$$l_i/r_o \sim St^{-1}\Lambda^{1/5}\mathscr{H}, \tag{3.3}$$

where $St = f_b r_o/u_w$ represents the dimensionless bubbling frequency, and f_b is either the imposed frequency, f_f, or the natural one, f_n, in the unperturbed case. In equation (3.3), $\mathscr{H} = \mathscr{F}^{-3/5}\mathscr{G}$ is a new unknown function which absorbs the dependence of l_n/r_o and of $St = f_n r_o/u_w$ on the Weber number, We. Applying a fitting procedure to the experimental results, it is deduced that $\mathscr{H} \simeq We^{1/4}$, and therefore that $\mathscr{F} \simeq We^{-1/3}$. Taking into account the obtained values for $\mathscr{F}$ and $\mathscr{H}$, equations (3.1)-(3.3) can be rewritten, obtaining the following scaling laws,

$$St_n\, We^{1/3} \sim \Lambda^{-1/3} \quad \text{with} \quad St_n = f_n r_o/u_w, \tag{3.4}$$

$$l_n/r_o \sim St^{-8/5} We^{1/20}, \tag{3.5}$$

$$l_i/r_o \sim St^{-1}\Lambda^{1/5} We^{1/4}. \tag{3.6}$$

To check the validity of these expressions, figure 3.9(b) shows, in a doubly logarithmic plot, the dimensionless natural bubbling frequency, corrected with $\mathscr{F}^{-1}(We) = We^{1/3}$, as a function of Λ for all the experimental water velocities, depicted with different colors. It can be observed that all the experimental results collapse onto a single curve with a slope of $-1/3$, as predicted by equation 3.4. Moreover, the latter result confirms the power-law exponents included in equations (3.1) and (3.2), as well as the validity of the fitted functions $\mathscr{H}(We)$ and $\mathscr{G}(We)$.

Moreover, figure 3.10(b) shows the dimensionless intact length as a function of the product $St\Lambda^{-1/5}We^{-1/4}$, for all the natural cases (colored stars) and the forced ones (open and solid symbols, corresponding to the breakup modes M1 and M2, respectively). It can be observed that the unforced results, as well as the forced ones within the M1 breakup regime, collapse onto a single curve, corresponding to the proposed scaling law (3.6). The small dispersion observed between both flow regimes is due to the slight deviation of the experimental data from the function $l_f/l_n = f_n/f_f$ deduced from figure 3.10(a). It is worth pointing out that in previous works devoted to forced breakup processes in planar co-flowing air-water streams (see Chapter 2 and Ruiz-Rus *et al.* 2017), as well as co-flowing liquid-liquid systems (Zhu *et al.*, 2016*b*), it has also been noticed that the intact length decreases as the inverse of the dimensionless forcing frequency. However, in the flow configuration at hand, the intact length includes an additional dependence on the flow conditions, reflected in the effects of Λ and We on the intact length. Indeed,

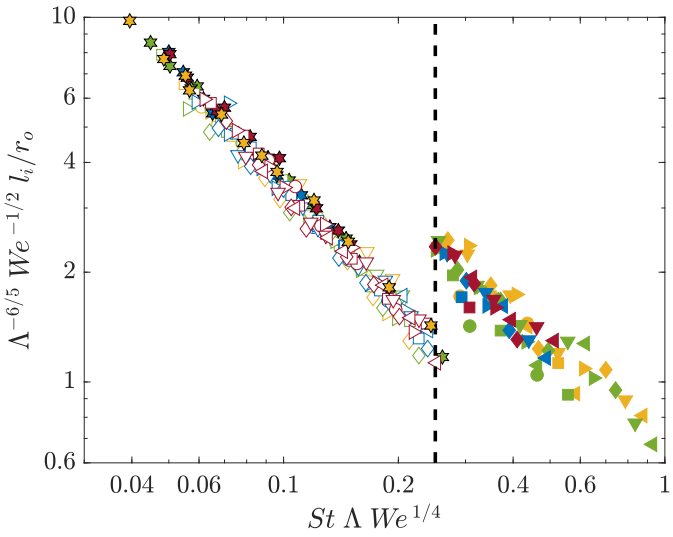

Figure 3.11: Doubly logarithmic plot of the compensated dimensionless intact length as a function of $St\Lambda We^{1/4}$. The sharp transition between the breakup modes M1 (open symbols) and M2 (solid symbols) is marked with a vertical dashed line. The results of the natural cases are included as colored stars. The different experimental values of We are plotted with different colors.

the latter parameters affect the duration of the expansion and collapse stages associated with the unforced bubbling process, which are also influenced by the imposed forcing frequency. In addition, the dimensionless intact length obtained with equation (3.5) is plotted as a solid line in figure 3.10(b). Notice that this function can be interpreted as the intact length that would be obtained for any other equivalent natural bubbling regime, established for the flow conditions Λ_q and We_q, assuming that the equivalent dimensionless bubbling frequency St_q is given by the expression (3.4). The good agreement obtained for the forced cases within the M1 regime confirms the fact that the mechanisms driving the forced bubble formation process are equivalent to those associated with the unforced case. Moreover, note that the dimensionless wavelength of the natural cases (black crosses), obtained as $u_w/(f_n r_o)$, are always larger than the intact length, reflecting the fact that a non-negligible fraction of the bubbling time is spent on the expansion stage. Similarly, the dimensionless wavelength of the equivalent natural cases, obtained as $St_q^{-1} \sim (\Lambda_q We_q)^{1/3}$ according to equation (3.4), is depicted as a dashed line in figure 3.10(b). As mentioned in previous sections, this equivalent dimensionless wavelength would coincide with the intact length in the absence of the expansion stage. It can be noticed that the experimental results for the forced cases within the breakup mode M2 (solid symbols) lie very close to the equivalent dimensionless wavelength (dashed line), although with a higher dispersion than the M1 bubbling cases, as expected from the higher receptivity to noise associated with the M2 regime.

Therefore, as evidenced by figure 3.10, the proposed scale for the dimensionless intact

length in equation (3.5), namely $l_i/r_o \sim St^{-1}\Lambda^{1/5}We^{1/4}$, accurately describes the parametric dependence for all cases, since it includes the effect of both the bubbling frequency, St, as well as the flow conditions, Λ and We. In addition, this scale can be used to determine the critical conditions associated with the transition between the M1 and M2 breakup modes. To that end, the results shown in figure 3.7(b) and figure 3.10(b) are reassembled in the doubly logarithmic plot shown in figure 3.11. Here, the dimensionless intact length l_i/r_o, compensated with the product $\Lambda^{-6/5}We^{-1/2}$, is represented as a function of $St\Lambda We^{1/4}$, as suggested by the scaling law (3.6). The compensated intact length is seen to monotonically decrease with $St\Lambda We^{1/4}$, until a sharp transition takes place from the breakup mode M1 (open symbols) to the breakup mode M2 (solid symbols). In particular, the critical conditions accomplish the condition $(St\Lambda We^{1/4})_t = 0.25$, as indicated by the vertical dashed line in figure 3.11. Beyond this critical value, the compensated intact length suddenly increases to a local maximum, and then monotonically decreases again, showing the emission of smaller bubbles from an air ligament of larger length than in the M1 regime. In addition, it can be noticed that the M2 mode allows the production of bubbles in ranges that cannot be reached within the unforced bubbling regime (colored stars). Thus, the production of bubbles within the M2 breakup mode overcomes the minimum bubble volume limitation imposed by the injector geometry associated with the natural bubbling flow, avoiding the lack of monodispersity.

3.5 Modelling of the forced bubbling process within breakup mode M1

It has been explained in previous sections that the forced bubbling regime is properly established at the selected forcing frequency only under the effect of a large enough pressure modulation amplitude, namely the *critical amplitude*. In fact, this pressure variation that is induced in the air feeding chamber, results in a modulation of the air flow rate toward the bubble, $Q_a(t)$, which is in turn coupled with the evolving air pressure inside the bubble, $p_b(t)$, driven by the dynamics of the growing process. The coupling between both the air pressure in the chamber and that inside the bubble is strongly conditioned by the pressure drop that takes place along the feeding line, being this a particular feature of the injector used in the facility. Therefore, in order to generically characterize the physical mechanisms driving the effective bubbling process, it proves convenient to analyze the forced bubble formation by means of the evolving air pressure inside the bubble, $p_b(t)$. To that aim, since it is not possible to experimentally measure that pressure, a simplified model, based on the transient incompressible air flow along the short injection needle from the feeding chamber to a spherically growing bubble, is proposed.

In a simplified manner, assuming a spherical shape of the bubble, the response of the growing interface radius to the pressure changes inside the bubble can be described

by means of the inviscid form of the spherical Rayleigh-Plesset equation (Gordillo *et al.*, 2007; Rodríguez-Rodríguez *et al.*, 2015),

$$p_b = \rho\left(R\ddot{R} + \frac{3}{2}\dot{R}^2\right) + \frac{2\sigma}{R}. \tag{3.7}$$

The l.h.s. of this equation represents the time-varying pressure inside the bubble relative to that in the surrounding water far away from the bubble, which is assumed to be the atmospheric one in this configuration (Sevilla *et al.*, 2005*a*). The terms in the r.h.s. stand for the inertial force and the surface tension, respectively, being $R = R(t)$ the radius of the growing spherical bubble. As mention above, the air pressure inside the bubble, $p_b(t)$, can be related to that measured in the air feeding chamber, $p_c(t)$, by means of an expression which considers incompressible mean air flows with large amplitude periodic oscillations through a circular tube of moderate length-to-diameter ratio, $L/(2r_i) = 21.25$. By retaining the unsteady term in the one-dimensional equation of motion (García *et al.*, 2014), a lumped parameter relationship between the pressure drop along the injection needle and the established air flow, which includes the influence of inertia and dissipation (Yellin & Peskin, 1975), has been obtained in the form,

$$p_b = p_c - \rho_a l\,\frac{\mathrm{d}u_i}{\mathrm{d}t} - \frac{1}{2}\rho_a K u_i\,|u_i|\,, \tag{3.8}$$

where $l = l(t)$ and $K = K(Re_i, 2r_i/L)$ stand for the inertial and the dissipative loss coefficients, respectively, with $Re_i = Re_a r_o/r_i$ the averaged inner Reynolds number. In addition, $u_i = u_i(t) \neq u_a$ is the instantaneous air velocity averaged over the needle inner cross sectional area. The absolute value of the instantaneous velocity is introduced in equation (3.8) to allow for possible flow reversal. Since the bubble growing from the needle tip is considered spherically shaped, the instantaneous air flow rate can be expressed in terms of the bubble radius R as

$$Q_a = \frac{\mathrm{d}}{\mathrm{d}t}\left(\frac{4}{3}\pi R^3\right) = 4\pi R^2\dot{R}\,. \tag{3.9}$$

Then, the instantaneous air velocity reads

$$u_i = \frac{Q_a}{\pi r_i^2} = \frac{4R^2\dot{R}}{r_i^2}, \tag{3.10}$$

and the acceleration can be obtained as

$$\frac{\mathrm{d}u_i}{\mathrm{d}t} = \frac{4}{r_i^2}\left(2R\dot{R}^2 + R^2\ddot{R}\right). \tag{3.11}$$

Therefore, a complete expression for the air pressure inside the bubble, coupled with equation (3.7), is obtained by introducing equations (3.10) and (3.11) into expression (3.8),

$$p_b = p_c - \frac{4\rho_a l}{r_i^2}\left(2R\dot{R}^2 + R^2\ddot{R}\right) - \frac{8\rho_a R^4\dot{R}|\dot{R}|}{r_i^4}\,K. \tag{3.12}$$

Here the inertial length $l(t)$ includes the lost-end correction l_o and an effective time-varying length which represents the equivalent length of the slug of fluid ejected under non-irrotational conditions (Cummings, 1986). Its value is obtained by the Cummings' empirical equation, properly adapted to a mean flow with periodic oscillations (Luong *et al.*, 2005), as

$$l(t) = l_o + \frac{3(l_o + L)}{3 + (\mathscr{L}/2r_0)^{1.585}}, \tag{3.13}$$

being the end correction $l_o \approx \pi r_o/4$ (Rayleigh, 1945; Howe, 1998) and the slug effective length,

$$\mathscr{L}(\tau) = \int_0^\tau u_i(t)\mathrm{d}t, \tag{3.14}$$

where τ is the time measured from the beginning of each cycle until the end of the expansion stage. Beyond this time, the bubble shape loses its sphericity. At this point, it is important to keep in mind that the present model is based on a spherically growing bubble. In this regard, it has been observed that at the end of the expansion stage, the growing interface is locally decelerated by the inward motion of the surrounding liquid near the injector. At this moment, the bubble begins to move downstream while the interface becomes parallel to the needle wall (see Sect. 3.3.1). Due to this loss of sphericity, the model is *a priori* not valid from this point. Moreover, given the geometric features of the injection needle, the ranges of the mean flow conditions and the characteristic frequencies and amplitudes of the oscillations, the dissipation coefficient $K(Re_i, 2r_i/L)$ represents a lumped loss coefficient accounting for the loss due to flow separation and reattachment at the inlet, together with the frictional viscous losses along the needle. In the present configuration, however, the length-to-diameter needle ratio does not assure a full development of a parabolic velocity profile. This fact, together with the oscillatory nature of the flow, implies that K might also vary with time. However, given the lack of published experimental data devoted to time-varying pressure loss coefficients, cycle-averaged values are adopted here. To that aim, for the injection needle used in this study, with $L/(2r_i) = 21.25$, an expression of K as a function of Re_i has been empirically obtained for the range of $Re_i < 1500$ analyzed here, $K \approx -50.46 \times 10^{-4} Re_i + 8.25$. The values of K determined by this expression result nearly similar to those calculated, for the same parameters, by extrapolation of the empirical expression for steady-state flow through short lines given by Lichtarowicz *et al.* (1965) for ranges of $L/(2r_i)$ from 2 to 10 and of Re_i from 10 to 20 000. Lichtarowicz *et al.* (1965) expression has been widely used for decades.

Therefore, the Rayleigh-Plesset equation (3.7) is numerically solved using MATLAB ODE solver (fourth order Runge-Kutta method) with the inside bubble pressure given by equation (3.12). The initial conditions $R(0)$ and $\dot{R}(0)$ are obtained from the experimental images, as explained below. The calculation is carried out during a whole bubbling cycle,

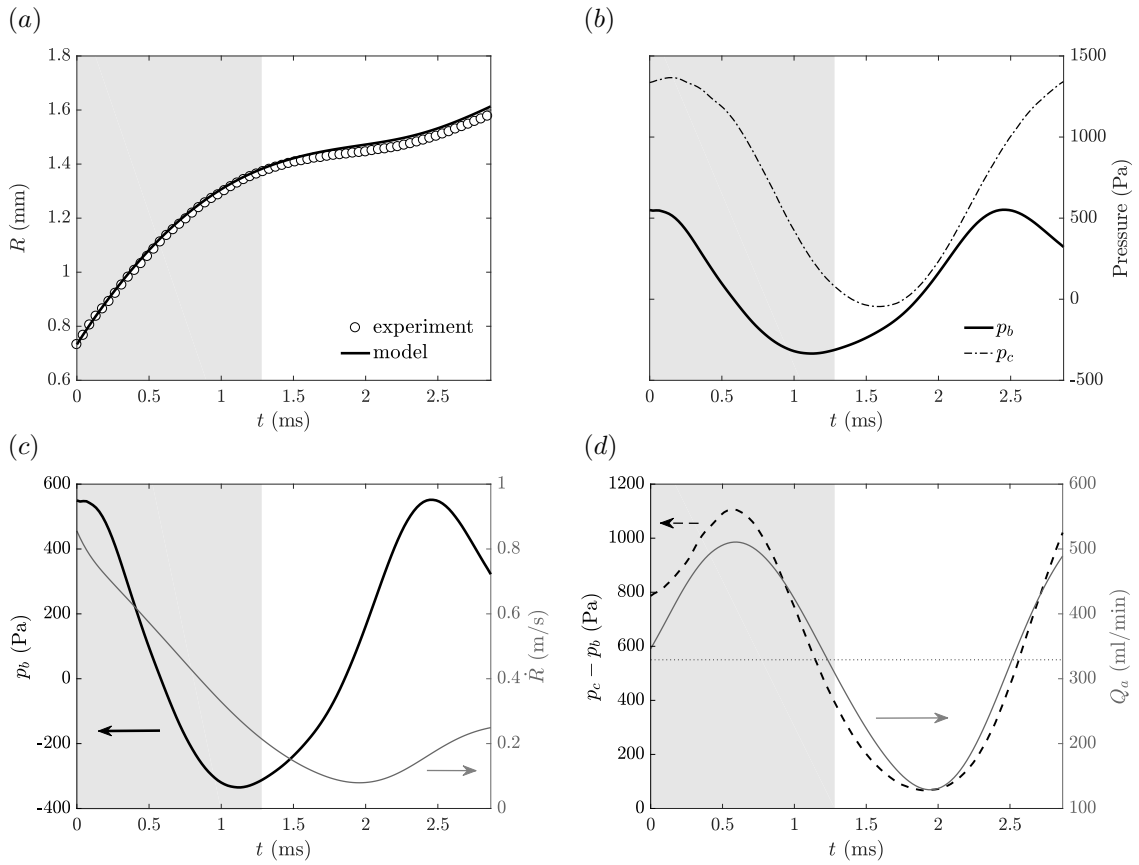

Figure 3.12: Results obtained from the model computed for a bubbling cycle of the effective bubbling process established for the flow conditions $u_a = 4.86$ m/s, $u_w = 1.36$ m/s ($\Lambda = 0.280, We = 15.38$); forced at $f_f = 350$ Hz ($St = 0.154$); with the corresponding initial conditions extracted from the experimental images (see main body). The shaded gray region marks the expansion stage, whose duration is roughly estimated as $1/f_f - l_i/u_w$.

finishing at the time at which the bubble pinch-off occurs, given by the experimental images analysis (see Sect. 3.2.2). In particular, from the bubble volume, $V(t)$, extracted from the images (see Sect. 3.2.2), the initial bubble radius $R(0)$ is obtained as the radius of an equivalent sphere whose volume is equal to that of the intact ligament, that is, the bubble volume detected in the first frame of the cycle, $V(0)$. In addition, the injected incompressible air flow rate is calculated as the time derivative of the detected volume, $Q_a = \dot{V}$. Therefore, the initial radial velocity of the interface is computed by evaluating equation (3.9) in the first frame as $\dot{R}(0) = \dot{V}(0)/[4\pi R^2(0)]$. Once the corresponding initial conditions are computed, equation (3.7) can be numerically integrated to obtain the time evolution of the bubble radius, $R(t)$, as well as that of the radial velocity, $\dot{R}(t)$, and acceleration, $\ddot{R}(t)$, together with the pressure inside the bubble, $p_b(t)$.

An example of the results given by the model is displayed in figure 3.12, showing a cycle of the effective bubbling process for the flow conditions $u_a = 4.86$ m/s, $u_w = 1.36$ m/s ($\Lambda =$

$0.280, We = 15.38$); forced at $f_f = 350$ Hz ($St = 0.154$). In particular, in figure 3.12(a), the evolution of the computed value of $R(t)$ (solid line) is compared with the equivalent bubble radius from the experimental images (symbols), obtained as $[3\,V/(4\pi)]^{1/3}$, exhibiting a good agreement during the expansion stage (shaded gray region). The time duration of the expansion stage has been roughly estimated as $1/f_f - l_i/u_w$, since the collapse stage has been previously shown to last approximately l_i/u_w. It can be noticed that the good agreement between the model and the experiments remains even beyond the expansion stage, that is, during the collapse stage, indicating that, despite the lack of sphericity, the model nearly reproduces the experimental evolution of the growing bubble volume.

Moreover, similarly to the natural case (Rodríguez-Rodríguez *et al.*, 2015), just after the previous bubble pinch-off, the new bubble rapidly expands to progressively decelerate giving rise to the collapse stage. The evolution of the pressure inside the bubble, $p_b(t)$, which drives the bubble dynamics is presented in figure 3.12(b), together with the externally modulated pressure in the feeding chamber, $p_c(t)$ (dashed-dotted line). The time evolution of the latter clearly presents a sinusoidal shape with the forcing frequency (see, in addition, figure 3.3). However, it can be observed that the calculated bubble pressure, $p_b(t)$, is indeed lower than the air pressure in the feeding chamber, but it does not follow a sinusoidal shape, even considering that the model estimation would not be valid during the collapse stage. This fact reveals that the inner bubble pressure is not only driven by the external modulation, but the growing bubble dynamics and the pressure drop along the needle play also an important role.

In addition, it has been observed for all the effective forced bubbling regimes in the breakup mode M1, that the bubble pinch-off is closely synchronized with the maximum of the modulated pressure registered in the air feeding chamber (see, in addition, figure 3.3). In that sense, the pressure increment externally induced in the chamber complements the ligament overpressure generated by the dynamics of the neck collapse (Sevilla *et al.*, 2005a; Gordillo, 2008; Gutiérrez-Montes *et al.*, 2013; Rodríguez-Rodríguez *et al.*, 2015), giving rise to the higher initial outward radial velocity, included in the initial condition $\dot{R}(0)$ (figure 3.12c). This rapid initial growth leads to a decrease of the bubble pressure (figure 3.12c), which results larger than in any other equivalent unperturbed case due to the air flow rate required to satisfy the continuity equation (3.9). This air flow rate is in turn controlled by the external modulation. In fact, given the synchronization of the process, the dynamics-induced pressure decrease coincides with the drop of the modulated chamber pressure, leading to a reduction of the air flow rate. This fact can be checked in figure 3.12(d), where it is shown that the pressure difference, $p_c(t) - p_b(t)$, always leads the flow rate. Notice that both the decrease of Q_a and the increase of R, contribute to the reduction of the characteristic radial velocity, $\dot{R}$, as indicated by the continuity equation, $\dot{R} = Q_a/(4\pi R^2)$. This fact induces a faster appearance of the local interface inward deformation leading to the collapse stage, what can be seen as an enhancement

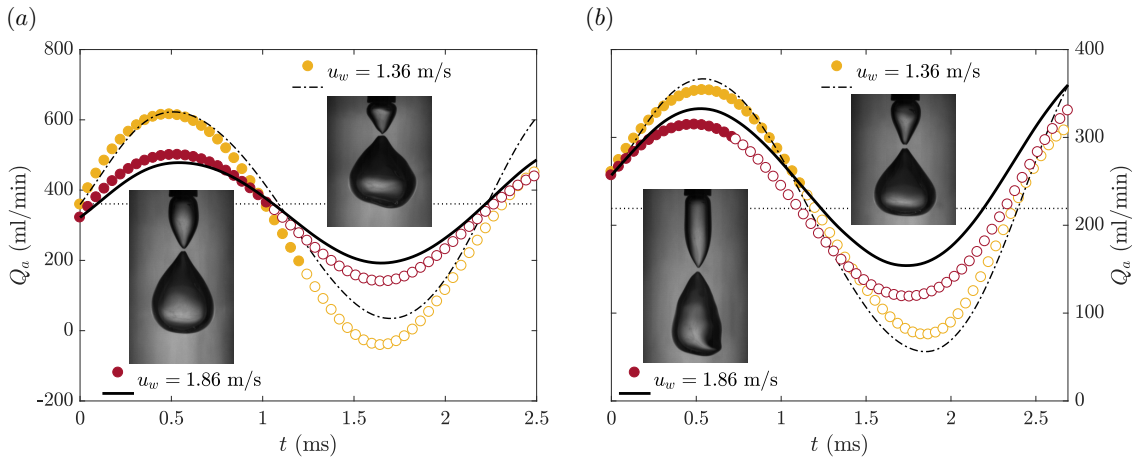

Figure 3.13: Comparison between the temporal evolution of the air flow rate obtained from the model (lines) and that extracted from the experimental images (symbols). Two different mean air velocities and forcing frequencies are shown, namely (*a*) $u_a = 4.86$ m/s; $f_f = 400$ Hz and (*b*) $u_a = 3.23$ m/s; $f_f = 350$ Hz. The horizontal dotted lines denote the corresponding constant air flow rate feeding the chamber Q_c. The time instants corresponding to the expansion and collapse stages are marked with solid and hollow symbols, respectively. Each color and line-style represent a different water velocity, as indicated, namely $u_w = 1.36$ m/s and $u_w = 1.86$ m/s, respectively. The snapshots reproduce the pinch-off instant corresponding to each analyzed case.

of the natural process under either constant air flow rate (Sevilla *et al.*, 2005*a*; Gordillo *et al.*, 2007) or constant pressure supply (Gordillo *et al.*, 2007). In the former, since Q_a remains constant, only the increment of R contributes to the pressure decrease. In the latter, an increase of Q_a appears as a response to the inner pressure decrease induced by the growing R, slowing down the $\dot{R}$ decrease and thus giving rise to larger bubbling times (Rodríguez-Rodríguez *et al.*, 2015). Finally, it has to be pointed out that this process does not occur in the same way during the breakup mode M2. In those cases, the initial ligament overpressure results so weak that the neck can be formed by another interface perturbation, induced by the forcing at a certain time previous to the pinch-off instant, with a growing rate large enough to overcome this natural overpressure (see Sect. 3.3.1).

The previous qualitative description of the mechanisms driving the neck formation at the end of the expansion stage is based on the Rayleigh-Plesset equation (3.7), under the assumption of a growing bubble with spherical geometry. In order to check the validity of the model, the air flow rate, obtained by evaluating equation (3.9) with the model results (lines), is compared in figure 3.13 with that extracted from the experimental images (symbols), computed as $Q_a = \dot{V}$. Snapshots of the pinch-off instants for the different analyzed cases are shown to examine the actual corresponding shapes of the intact ligaments. Generally, a very good agreement is obtained during the expansion stage, pointed out with solid symbols. However, for cases exhibiting very long ligaments (red solid symbols in figure 3.13*b*), corresponding to low values of St, the model shows a slight departure from

the experimental data, manifesting the more slender shape of the ligament. Nonetheless, the general evolution of the air flow rate is well estimated by the model. Something similar is found for the results obtained during the collapse stage, denoted with open symbols. As mentioned before, although the lack of sphericity is noticeable as the new ligament progressively grows in the axial direction during the collapse stage, the general trends of the evolution are fairly well reproduced by the model. Finally, regarding the effect of the water velocity, it can be clearly observed that the amplitude of the air flow rate oscillation, induced by the forcing mechanism, decreases as the water velocity rises. This effect of the water velocity was previously observed with the effective pressure amplitude measured in the feeding chamber.

3.6 Conclusions

This Chapter describes a new method to actively control the bubbling process in axisymmetric air-water co-flowing jets. The bubble generation frequency, as well as the volume of the obtained monodisperse bubbles can be independently controlled, substantially reducing the strong undesired influence of the injector geometry. To that aim, a forcing system based on a loudspeaker, which induces a periodic pressure modulation in the air stream, has been incorporated into the air feeding line of a cylindrical gas-liquid co-flow device. Its performance during the bubbling process has been experimentally analyzed by high-speed recordings of the growing bubble interface.

Large enough amplitudes of the pressure modulation have been found to control the bubble formation process, generating monodisperse bubbles of volume $V_b = Q_c/f_f$, at the forcing frequency f_f. Two different bubble breakup regimes, namely mode M1 and M2, have been observed depending on the unperturbed flow conditions and on the demanded frequency. More precisely, the breakup mode M1 has been identified as a bubbling regime similar to the unperturbed case in which the mechanisms leading to the bubble formation and detachment are accelerated to the forcing frequency by the induced air pressure modulation. On the other hand, the breakup mode M2 acts as a jetting regime in which an induced interface perturbation convectively grows, periodically forcing the detachment of monodisperse bubbles from the tip of a slender air ligament. It has been found that the mode M2 allows the production of very uniform bubbles under flow conditions which are not enabled for the corresponding unperturbed case, thus obtaining small monodisperse bubbles whose volume overcomes the limitation imposed by the geometry of the injector. Bubble volume reductions up to 80% of the corresponding volume obtained for the same unperturbed flow conditions, have been achieved in the parameters range analyzed in this work.

In addition, the established forced bubbling regimes have been characterized by means of the intact length, which is the distance at which the bubble pinch-off takes place. It

has been observed that this length properly describes the duration of both stages involved in the bubble formation process, assuming that the induced interface perturbation travels downstream at the outer co-flowing liquid stream velocity. A scaling law, $l_i/r_o \sim St^{-1}\Lambda^{1/5}We^{1/4}$, based on the dimensionless parameters of the problem, has been proposed. This result allows us to determine the particular conditions under which the breakup mode M2 is triggered.

Finally, the forced bubbling regime within the breakup mode M1 has been modelled by means of the inviscid form of the spherical Rayleigh-Plesset equation. For this purpose, the pressure drop along the air injection needle has been described through a lumped parameter expression for the one-dimensional momentum equation, including both the inertia and the dissipation effects. A very good agreement between the model results and the experimental images has been obtained, mainly during the first expansion stage at which the bubble remains attached to the injector tip and a nearly spherical growth of the interface can be assumed. The model allows us to understand the dynamics of the forced bubbling process, determining the physical mechanisms driving the neck formation which leads to the bubble pinch-off. More precisely, it has been found that the process is driven by the overpressure that appears at the beginning of the cycle, being the subsequent pressure drop inside the bubble induced by the rapid growth of the interface, and assisted by the decrease of the feeding air flow rate which is modulated by the external forcing effect.

Part II

Coalescence in confined two-dimensional bubble swarms

CHAPTER
FOUR

Evolution of two-dimensional bubble swarms driven by coalescence

4.1 Introduction

For industrial processes using dispersed gas-liquid flows such as bubble columns, prediction of bubble sizes is important because, for a large part, the size distribution governs the mass, momentum and energy transfers at the interfaces. In the present Chapter, we investigate the evolution of the bubble size distribution in a swarm of high-Reynolds number bubbles confined in a planar vertical thin-gap cell filled with liquid at rest. This flow configuration finds promising applications in chemical engineering as it is expected to be an alternative reactor of intermediate size that takes advantage of confinement to enhance mass transfer, as in monolith reactors, and of intense bubble-induced agitation to develop satisfactory in-plane mixing, as in large three-dimensional bubble columns (Roudet *et al.*, 2017; Alméras *et al.*, 2018). Some recent applications have been developed concerning light-activated reactions or cultivation of micro-algae in photo-reactors that need narrow geometries due to light absorption and attenuation, while keeping efficient mixing and mass transfer is still required (Oelgemoller, 2016; Pruvost *et al.*, 2017; Thobie *et al.*, 2017). Bubble sizes resulting from injector systems and from coalescence and breakup events in the flow govern the processes and it is crucial to develop knowledge about both interfacial mechanisms. For bubbles of size greater than the gap width, contacts between bubbles are favored by confinement as bubbles cannot avoid each other out of plane. Coalescence is thus strongly activated and in such flow configuration it is important to study the mechanisms leading to coalescence in order to control bubble sizes.

In the present confined flow configuration, all the models have to be re-built due to the original two-dimensional confined hydrodynamics. This is the ultimate goal of the investigation started during this PhD thesis that aims at a deep and accurate description of the bubble population evolution. Such description can be obtained as it is possible to directly detect all the bubbles in the two-dimensional swarm. Coalescence being the dominant mechanism in the present flow, even if some moderated breakup can be observed, this work will ultimately provide direct measurements of the various sink-source terms of the PBE, equation (1.3), and will try to propose closure laws reproducing these terms.

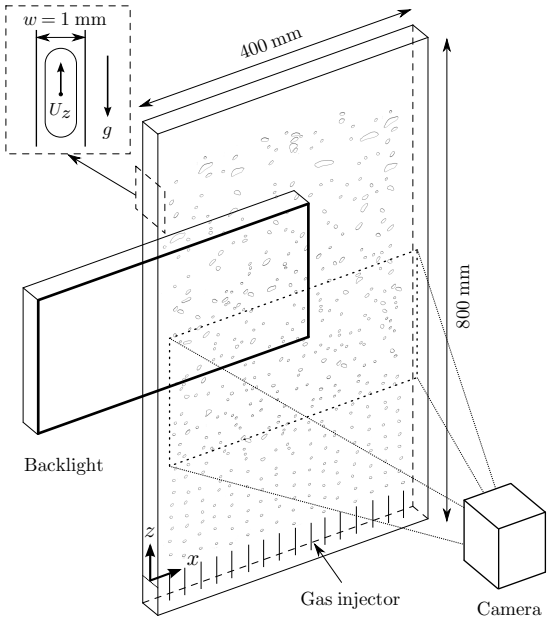

Figure 4.1: Sketch of the experimental set-up. One of the three different positions of the camera is depicted together with its field of view. The zoomed area schematizes the lateral view of the cell with a bubble flattened between the walls and both liquid films.

In order to obtain an estimation and a modeling of the characteristics of the coalescence process, two different types of experiments have been carried out, providing complementary results: low-frequency and high-frequency image acquisition of the coalescing confined bubble swarm. The first allows to obtain a statistical view of the coalescence process and a preliminary analysis of its characteristic features. It is detailed in Section 4.3. The second includes the tracking of the bubble paths and provides the spatial and temporal evolutions of the coalescence cascade. It aims at elaborating closure laws for the modeling of the evolution of a coalescing bubble swarm evolving in the confined configuration. Analysis of the rich information provided by the high-speed measurements is still in progress but a brief description of the analysis and some global results will be provided in Section 4.4.

This Chapter is organized as follows. Section 4.2 describes the experimental facility and the digital image analysis developed for the low-frequency image acquisition experiments while the statistics of their results are presented in Section 4.3. Next, the high-frequency image acquisition experiments as well as the methods developed to obtain the direct measurements of the rate of change of the bubble population are described in Section 4.4. Finally, Section 4.5 is devoted to conclusions.

4.2 Experimental aspects

4.2.1 Experimental set-up

The confined bubble swarm is generated within a quasi-bidimensional vertical cell filled with distilled water at ambient temperature, being its top side open to atmospheric pressure (Bouche *et al.* 2012, 2014). The cell consists of two parallel glass plates (800 mm high and 400 mm wide) confining a thin gap of $w = 1$ mm width (figure 4.1). Contrary to previous works related to confined bubble swarms (Bouche *et al.* 2012, 2013, 2014; Alméras *et al.* 2016), no electrolyte is added to the liquid phase, initially at rest, in order to allow the natural bubble coalescence taking place from hydrodynamic interactions. In addition, the distilled water was regularly renewed to prevent interface contamination.

Air bubbles of constant size are periodically injected at the bottom of the gap through an array of 16 capillary injectors of 0.6 mm inner diameter and 0.8 mm outer diameter (figure 4.1). The injectors are equally distributed along the bottom of the cell and they are connected to a controlled pressure air feeding chamber. The pressure drop along the injectors assures a constant air flow rate towards each emerging bubble (Gordillo *et al.* 2007). The bubble detachment frequency, f_b, can be accurately selected through the controlled pressure of the feeding chamber, p_g, and individually checked by means of a stroboscopic light at each injector tip.

The generated bubble swarm is registered using the shadowgraphy technique in a measuring zone comprising the whole spanwise of the cell. To that aim, a section of the cell is illuminated from behind with uniform, constant and diffused white light perpendicular to the cell plane (figure 4.1). Facing the light source on the other side of the cell, a camera (Photron APX) equipped with a 85 mm lens takes images of 1024×512 pixels using an exposure time of 1/2000 s. In order to analyze the evolution of the bubble population as they rise while maintaining the desired resolution, the backlight and the camera is placed at three different positions (figure 4.2). We shall describe in detail the image acquisition rate and resolution as well as the digital image processing techniques and the measurements spatial discretization and statistical convergence in Sect. 4.2.2.

The volume of the injected bubbles ensures that the bubble size is always larger than the gap width. Therefore, the bubbles result strongly flattened between the cell walls and both thin liquid films (see zoomed area in figure 4.1). Under this configuration, independently of the bubble size distribution of the swarm, no dewetting at the glass plates is observed and the bubble degrees of freedom are reduced, inducing a planar motion of the bubbles. Hence, a bidimensional approach can be assumed (Roig *et al.* 2012; Filella *et al.* 2015). The bidimensional equivalent diameter of the bubbles within the swarm is defined as $D = (4V/\pi)^{1/2}$, where V is the bidimensional volume of the bubble, obtained as the projected area onto the cell plane determined by processing the images. The injected gas volume fraction, α_0, is determined from the bidimensional volume occupied

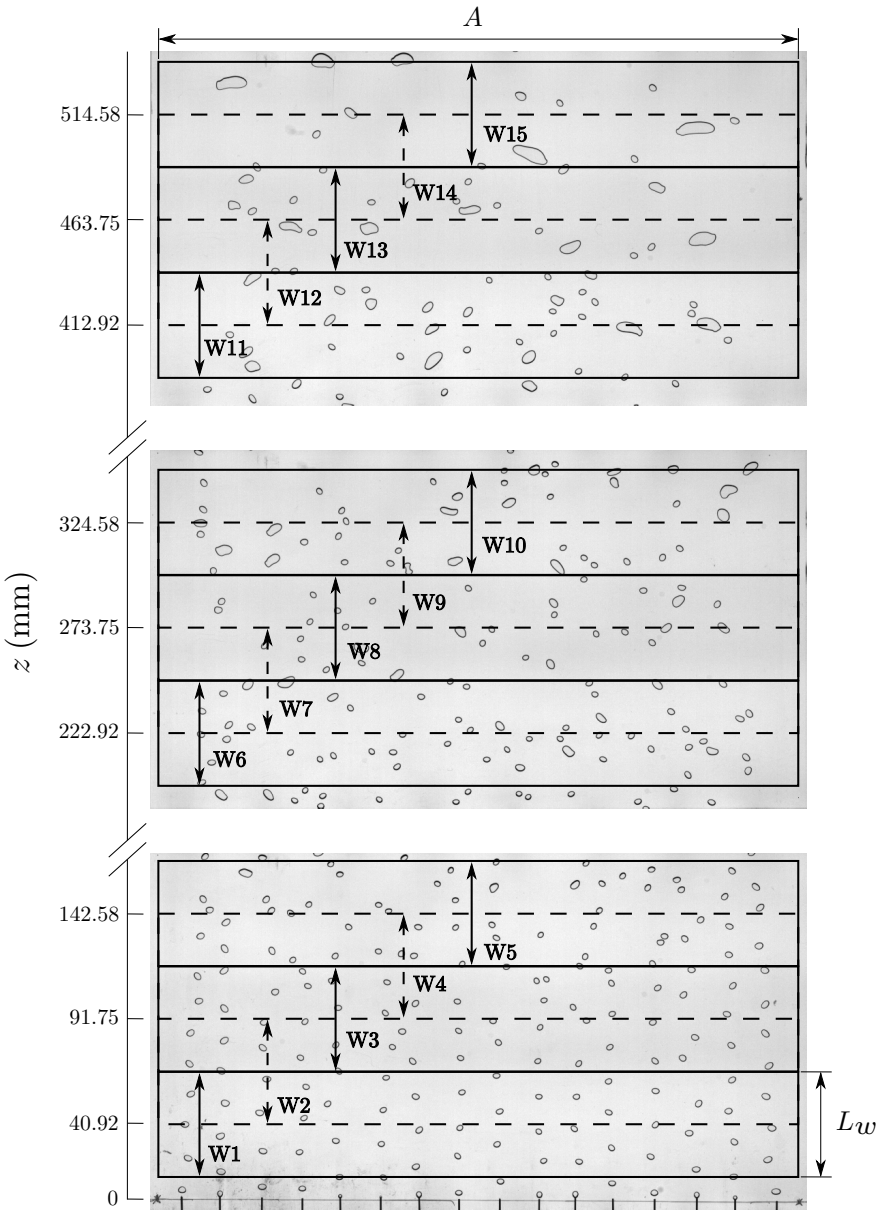

Figure 4.2: General overview of the whole space registered by means of shadowgraph images at three different positions for $\alpha_0 = 3.2$ %. The 15 equal windows used for the spatial discretization are superimposed over the pictures. The downstream length of each measuring window is $L_w = 50.83$ mm and the bidimensional cross-sectional area almost comprises the whole spanwise of the cell, $A = 350$ mm. The vertical axis denotes the middle point of some of these measuring windows.

by the bubbles in a measuring window a few millimeters above the capillary tubes ($W1$ in figure 4.2). In the current experiments, α_0 is varied between 2.4 % and 6.7 % by adjusting the bubble generation frequency. Figure 4.3 shows the mean equivalent diameter of the injected bubbles, D_0, corresponding to each injection condition. The variations reflecting

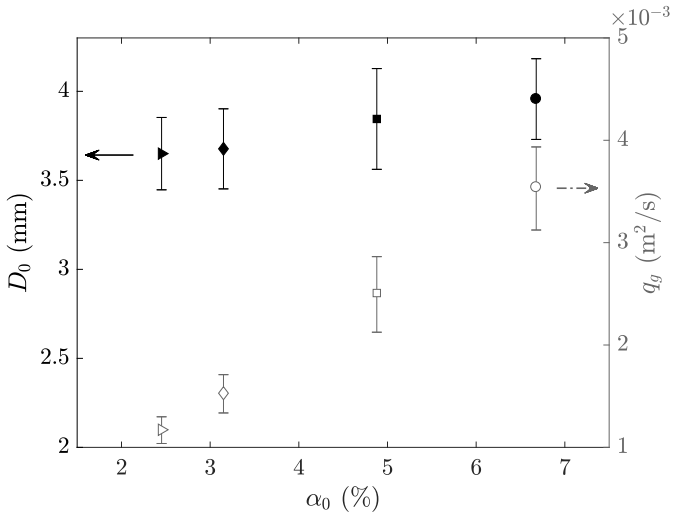

Figure 4.3: Mean injection bubble equivalent diameter as a function of the air volume fraction measured at a few millimeters above the injectors tip for each experimental set, with standard deviation as error bars (left vertical axis). Estimation of the total air flow rate per unit depth injected for each initial air volume fraction, obtained through the bidimensional volume of the bubbles and the generation frequency for each injector (right vertical axis).

the discrepancies between the injectors result negligible and initially monodisperse bubble swarms are assumed, similar to those studied in (Bouche *et al.* 2012, 2014). Moreover, the slight bubble size increment observed with the gas fraction, within the range explored in this work, does not have a significant effect compared to that of the bubble concentration (Bouche *et al.* 2012, 2014). Additionally, the total air flow rate per unit depth can be estimated as $q_g = 4\pi {D_0}^2 f_b$, showing a linear increase with the gas fraction, as can be seen in figure 4.3. Table 4.1 presents a summary of the experimental injection conditions selected in our study.

	α_0 (%)	D_0 (mm)	p_g (bar)	f_b (s^{-1})	q_g ($m^2 s^{-1}$) $\times 10^3$
Set 1	2.4	3.65 ± 0.20	0.6	7	1.18 ± 0.13
Set 2	3.2	3.68 ± 0.22	0.7	9	1.53 ± 0.19
Set 3	4.9	3.85 ± 0.28	0.8	13.5	2.51 ± 0.38
Set 4	6.7	3.96 ± 0.23	0.9	18	3.54 ± 0.42

Table 4.1: Experimental injection conditions: α_0, air volume fraction at the bottom of the cell; D_0, mean equivalent diameter of the injected bubbles; p_g, controlled pressure of the air feeding chamber; f_b, selected bubble generation frequency; q_g, estimated total air flow rate per unit depth.

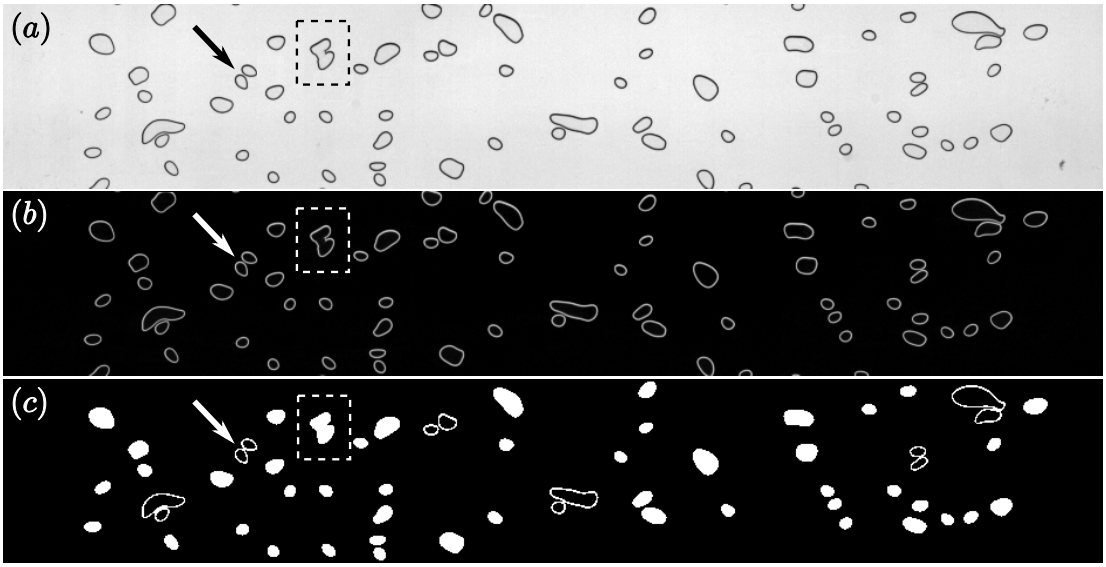

Figure 4.4: Portion of a registered image, of size equivalent to a measuring window, under the digital image processing steps. (*a*) Original grayscale image. (*b*) Inversion of the pre-processed image showing the brightness normalization and the improved gray-level gradient between the bubbles edges and the background. (*c*) Binarized image in which all the detected bubbles have been classified as single bubbles (shown as filled objects) or as bubbles in collision (shown as hollow objects). A typical bubble collision is pointed by an arrow. A just coalesced bubble is also highlighted by the box with dashed frame.

4.2.2 Image recording and digital analysis

The particular morphology of this configuration allows a direct analysis of the whole bubble population, since the planar motion prevents the bubbles from overlapping in the recording plane. Therefore, the bubble swarm downstream evolution is described by means of a statistical analysis of the bubble population characteristic parameters averaged over the horizontal cell width.

The registered cell section at each recording position consisted of a 16-bits grayscale rectangle of size 350 mm $\times$ 152.49 mm with a pixel-size resolution of 350 μm. In order to increase the spatial resolution of the measurements, the results of each image analysis are divided into five equal horizontal windows (width A = 350 mm and length L_w = 50.83 mm), with an overlapping of 50% of their length as indicated in figure 4.2. At each recording position, sets of around 3000 uncorrelated images have been registered at a frame rate up to 1/2 f.p.s. This acquisition rate ensures that all the bubbles present in the image have been renovated between each frame. The total number of collected images represents an amount of analyzed bubbles per window between 25 000 and 250 000, depending on the injected air flow rate and on the recording position. This ensures the statistical convergence of the characteristic parameters of the bubble population.

Since even the smallest bubble considered in our analysis results larger than the thin

gap of the cell, the bubble shape resembles a disk rather than a sphere. Therefore, most of the bubble surface results perpendicular to the light direction, appearing in the images as a region of connected pixels with a gray-level almost equal to that of the liquid background, surrounded by a closed narrow dark fringe (figure 4.4a). The width of this darker line remains nearly constant, independently of the bubble size, due to the curvature of the bubble interface onto the cell gap plane (Bongiovanni *et al.* 2000) and it delimitates the bubble edge (detailed images of isolated bubbles within the same experimental facility and for the same range of sizes reached in this work can be found in Roig *et al.* (2012)). Following this criterion, every image is analyzed using an specifically developed image processing routine. It is based on a two-step binarization process followed by a bubble detection and classification algorithm. Once the bubbles present in each image are detected, their centroid position as well as their bidimensional volume are measured. Although the whole raw registered image is processed as an unique element, figure 4.4 shows an example of the processing steps only in one of the measuring windows for the sake of clarity.

The first step involves a pre-processing of the original grayscale image (figure 4.4a). This implies the subtraction of a background reference image without bubbles and the normalization of the image brightness by correcting each value of the pixel intensity matrix. More detailed information regarding the brightness correction method can be found in Fu & Liu (2016). This brightness normalization reduces the uncertainties because of the variation of the illumination conditions and eases the next binarization step. Figure 4.4(b) shows an inversion of the resulting corrected image, in which any physical noise (e.g. glass wall scratches and background noise) has been removed while the gray-level gradient between the bubbles edges and the background has been improved. Then, the well-known Otsu's method (Otsu 1979) is used in the second step as an automatic, robust, global binarization-threshold selection technique.

After binarization, single bubbles can be detected as blobs of connected low-level pixels enclosed by unique edges of high-level pixels which are totally surrounded by background. Moreover, hydrodynamics interactions lead to several bubble collisions. The bubbles involved in a collision share the same edge of connected high-level pixels, however there exists an independent blob of low-level pixels for each involved bubble. Contrary to other works dealing with bubble collisions or cluster formation through a separation distance criteria (see e.g. Figueroa-Espinoza & Zenit 2005; Figueroa-Espinoza *et al.* 2018), the contact between at least one edge pixel of each bubble is required in the present work to define a collision. Figure 4.4(c) shows detected single bubbles as filled objects and those involved in a collision as hollow bubbles. This procedure to detect the bubble collisions allows us to clearly distinguish between two independent bubbles involved in a collision (denoted by an arrow in figure 4.4) and that newborn bubble just appeared due to the coalescence of two colliding bubbles (boxed by dashed lines in figure 4.4).

Once the bubbles have been detected and classified as *single* or *in-collision* bubbles,

their instantaneous characteristics are determined. The bubble position is obtained as the centroid position of the in-side blob of low-level pixels. The bidimensional volume is defined as the area occupied by the pixels belonging to the in-side blob plus those belonging to the edge. A difficulty arises obtaining the volume of those bubbles involved in collisions, since the pixels conforming the edge of the bunch is shared between all the bubbles. To deal with this, the total area of the bunch edge is distributed among the bubbles attending to the ratio between the number of pixels which form the bunch edge perimeter and those of the perimeter of each bubble in-side blob.

4.3 Statistics of the experimental results

According to Bouche *et al.* (2012, 2014) the agitation induced in a confined homogeneous bubble swarm leads to hydrodynamics interactions which substantially modify the bubbles motion compared to that of an isolated bubble of the same size. Furthermore, in our particular case, distilled water has been used letting the bubbles coalesce naturally, so the bubble collisions induced by hydrodynamics interactions eventually lead to bubble coalescence giving rise to new larger bubbles. Since the entrainment by bubble wakes was found to be the principal mechanism modifying the natural bubble motion in a monodisperse swarm (Bouche *et al.* 2012), the polydisperse size distribution typically found in our experiments (figure 4.2), introduces additional phenomena associated to the wakes of the newly formed bigger bubbles. Therefore, as the bubble size distribution becomes wider due to the generation of larger bubbles, the degree of agitation in the vicinity of bubbles is expected to increase, enhancing the bubble coalescence. However, the liquid perturbations induced by the bubble wakes and localised just behind them are strongly attenuated by the shear stress at sidewalls (Roig *et al.* 2012). In that case, turbulence cannot develop due to the confinement (Bouche *et al.* 2014).

As mentioned before, the bubble swarm at the bottom of the cell is nearly monodisperse, with an equivalent diameter of the injected bubbles, obtained through the digital image processing, that barely changes with the experimental injection conditions (see figure 4.3). In addition, the mean rise velocity of an isolated bubble of the same size can be obtained making use of the scaling law proposed by Filella *et al.* (2015)

$$U_b \simeq 0.75(w/D)^{1/6}\sqrt{gD}, \tag{4.1}$$

where g is the gravity acceleration, w the thickness of the cell and D the equivalent diameter of the bubble. Therefore, the Archimedes number, $Ar = \sqrt{gD}\,D/\nu$, the confinement ratio, $\delta = w/D$, the in-plane Reynolds number, $Re = U_b D/\nu$, and the gap Reynolds number, $Re\delta^2$, lie in the following ranges for the injected bubbles: $630 \leqslant Ar_0 \leqslant 850$, $0.24 \leqslant \delta_0 \leqslant 0.29$, $380 \leqslant Re_0 \leqslant 500$ and $28 < Re_0{\delta_0}^2 < 32$; being ν the water kinematic viscosity. For such dimensionless groups, the in-plane flow can be considered as bidimen-

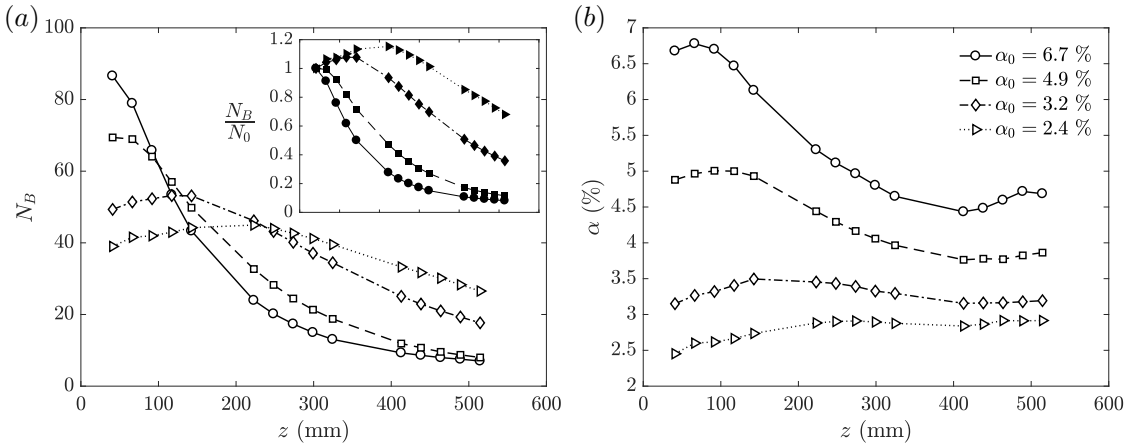

Figure 4.5: (a) Downstream evolution of the net number of bubbles measured in each position (window) for the different experimental injection conditions. The inset shows this evolution normalized by the initial number of bubbles, N_0. (b) Downstream evolution of the local air volume fraction, obtained from the bidimensional volume of the bubbles of all sizes present in each window.

sional and dominated by inertia (Bush & Eames 1998). In addition, the equivalent isolated bubble motion is characterized by slight vertical and strong horizontal oscillations, close to $0.1U_b$ and $0.45U_b$ respectively, and by unsteady wakes with periodic vortex shedding (Roig *et al.* 2012).

4.3.1 Global downstream evolution of the bubble swarm

The results of the image processing, discretized along the 15 measuring windows and averaged over the total number of analyzed images, allow an analysis of the evolution of the bubble population mean characteristic parameters. In fact, the net number of bubbles detected at each position, N_B, gives a qualitative interpretation of the importance of the coalescence within the bubble swarm. Figure 4.5(a) shows the downstream evolution of the amount of bubbles. For high injected air volume fractions (i.e. α_0 = 4.9 and 6.7 %, respectively) the large amount of monodisperse bubbles conforming the swarm near the bottom of the cell quickly decrease as the bubbles rise. Strong bubble-bubble interaction occurs as the bubbles are injected, giving rise to several collisions and coalescence events. In fact, once the first coalescence events take place, larger bubbles are generated leading to coalescence cascades which quickly involve more and more bubbles. The beginning of coalescence as well as the rate of *death* of the originally injected bubbles depend on the initial number of bubbles, N_0, as can be seen in the inset of figure 4.5(a). It should be pointed out that N_0 is directly related to the selected bubble generation frequency, f_b, and thus to the injected air volume fraction, α_0. In addition, as the bubble population is reduced, the net amount of coalescence events is reduced too. Although the number of bubbles decreases with the downstream distance, there is no evidence of reaching a

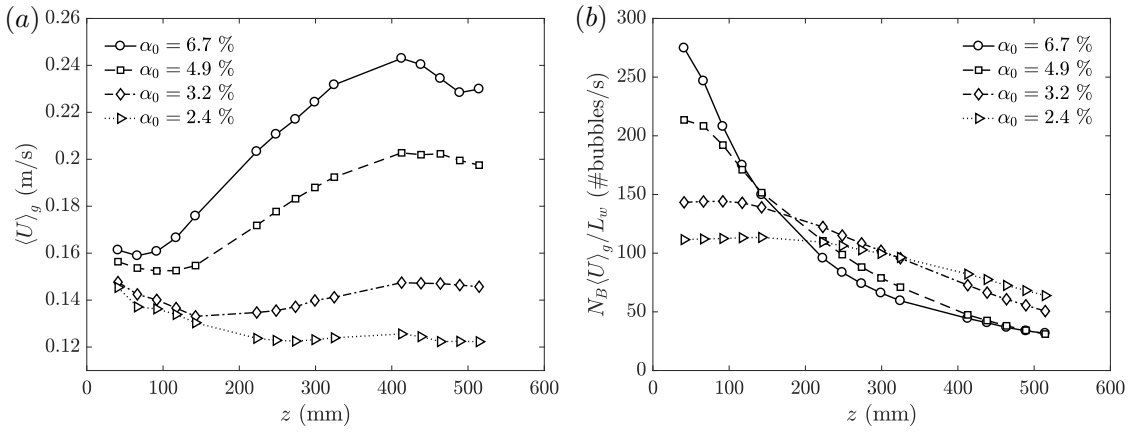

Figure 4.6: (a) Downstream evolution of the averaged vertical velocity of the gas phase. It shows an increment due to buoyancy driven variations of the rise velocity as larger bubbles appear due to coalescence. (b) Evolution of the total flux of bubbles per window. The value refers to an estimation of the bubble flux, assuming that the ascending velocity is the same for all the bubble sizes and equal to that of the whole gas phase $\langle U \rangle_g$.

final frozen-state where coalescence becomes negligible. In fact, we have observed that the bubble induced liquid agitation destabilizes the largest bubbles, giving rise to breakage events which increasingly influence the net number of bubbles, as we shall describe in Sect. 4.3.2. On the other hand, for lower injected air volume fractions (i.e. $\alpha_0 = 3.2$ and 2.4 %, respectively), it takes longer to give rise to bubble collisions. Therefore, coalescence appears at higher positions and the net number of bubbles decreases with an initial smaller rate (see middle positions in the inset in figure 4.5a). Once the coalescence begins (i.e. the net amount of bubbles starts to decrease), the evolution of the number of bubbles for these smaller air volume fractions follows a trend similar to those observed for the larger injection fractions but widely expanded along the cell height. An additional phenomenon arises from the analysis of the evolution along the first measuring windows, where coalescence is not present yet. In fact, the number of bubbles slightly increases, showing an increment of the bubble concentration with the position. Since the bubble population remains monodisperse, there is no bubble breakage and this agglomeration effect is directly related to the deceleration of the ascending bubbles, as we shall explain below. Although equally present, this effect cannot be detected in the evolution of the number of bubbles for larger injected air volume fractions, due to the stronger role of coalescence.

The local air volume fraction at each position, $\alpha(z)$, can be obtained through the bidimensional volume occupied by the entire population of bubbles present in each measuring window (figure 4.5b). Assuming that the average liquid velocity is negligible everywhere in the cell and taking into account that the reduction of the number of bubbles leads to the presence of larger bubbles within the bubble population, the downstream evolution

of α reflects the buoyancy driven variations of the averaged ascending velocity of the gas phase that increases as larger bubbles are generated due to coalescence. Therefore, the continuity equation allows an estimation of this local ascending velocity of the whole gas phase as

$$\langle U \rangle_g = q_g(\alpha A)^{-1}. \tag{4.2}$$

Figure 4.6(a) shows the downstream evolution of $\langle U \rangle_g$ which is highly influenced by presence of large bubbles within the swarm, mainly for the highest injected air volume fractions (i.e. $\alpha_0 = 4.9$ and 6.7 %, respectively). However, as we will show in Sect. 4.3.2, for the smallest air fractions (i.e. $\alpha_0 = 3.2$ and 2.4 %, respectively), the larger bubbles contribution to the population is less important, being $\langle U \rangle_g$ dominated by the smaller bubbles mean ascending velocity. In addition, the downstream evolution along the lower positions clearly reflects the injected bubbles deceleration effect previously mentioned. In fact, according to the estimated values of the air flow rate (see Table 4.1), the injected air velocities obtained in the first measuring window substantially exceed the terminal velocity of an isolated bubble of the injection size (i.e. ~ 0.115 m/s, predicted by equation 4.1). This overvelocity is attenuated until the isolated bubble mean velocity is almost reached around 200 mm above the injection position (see the results for $\alpha_0 = 2.4$ % in figure 4.6a), resulting from a balance between the buoyancy force and the in-plane drag force (Filella *et al.* 2015). This transient effect has not been reported in previous works related to this configuration (Roig *et al.* 2012; Bouche *et al.* 2012; Filella *et al.* 2015; Alméras *et al.* 2016, among others) since their region of analysis was located sufficiently far from the inlet to avoid the injection effects, assuring that the mean ascending velocity of an isolated bubble is well described by equation (4.1). It is worth noting that this initial deceleration effect results inherent to the swarm generation system, affecting only the injected bubbles. Any other bubble size, emerging from coalescence, keeps a mean ascending velocity close to that predicted by equation (4.1) depending on its equivalent diameter, simply affected by the swarm induced liquid agitation. Moreover, the deceleration related bubble agglomeration favors the bubble-bubble interactions along the earlier positions as the inter-bubble distance is progressively reduced.

Finally, a rough estimation of the total flux of bubbles of all sizes per position can be obtained assuming that the ascending velocity is the same for all the bubble sizes and equal to that of the whole gas phase, $N_B\langle U \rangle_g / L_w$ (figure 4.6b). The downstream evolutions obtained for all the injected air volume fractions reflect that the initial bubble coalescence rate highly depends on the injection conditions, since the generated bubble swarms result monodisperse and the variations introduced in the different experiments are based on the initial number of bubbles, N_0, selected through the injected air flow rate.

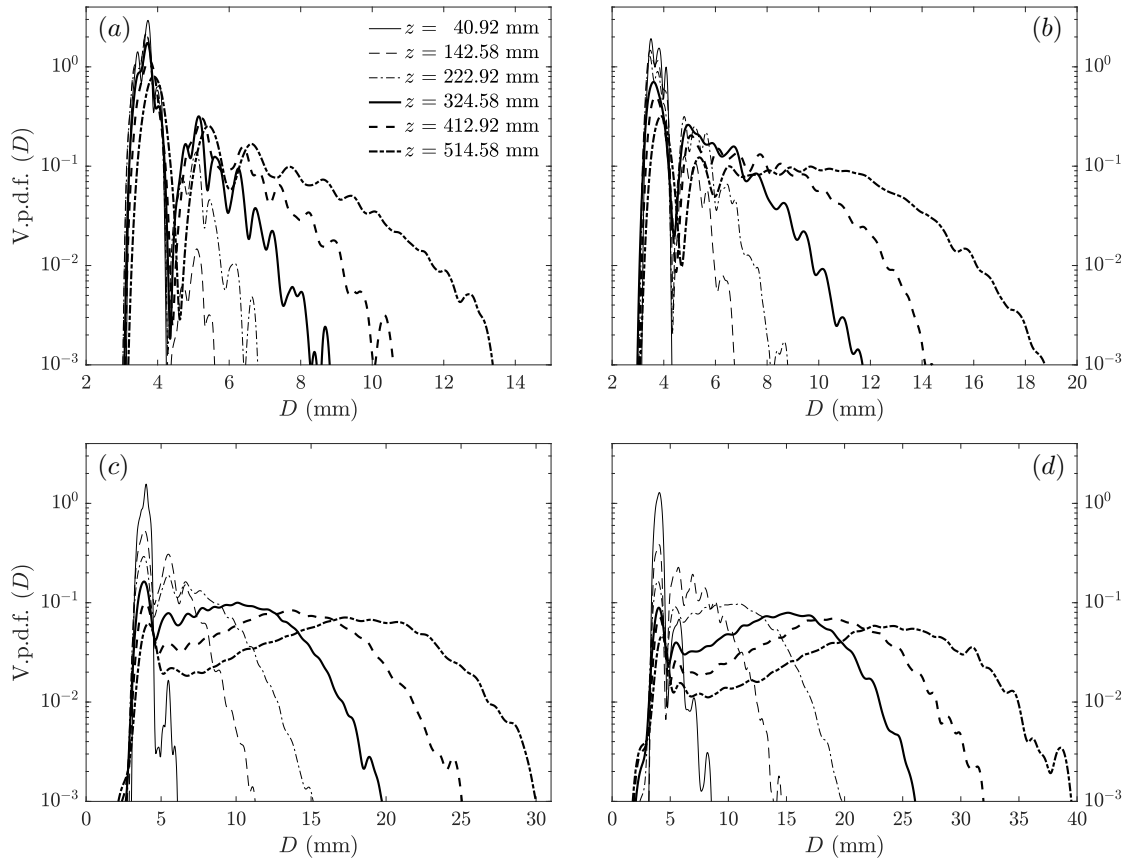

Figure 4.7: Downstream development of the bubble size distribution described by the bidimensional volume-size bubble p.d.f. for (*a*) $\alpha_0 = 2.4$ %, (*b*) $\alpha_0 = 3.2$ %, (*c*) $\alpha_0 = 4.9$ % and (*d*) $\alpha_0 = 6.7$ %. Only some measuring locations have been plotted for clarity. The generated bubble swarm for every injection condition starts from the same monodisperse distribution near the bottom of the cell which widens further downstream due to bubble coalescence.

4.3.2 Development of the bubble size distribution

For each measuring window, the equivalent diameters of the detected bubbles, even those involved in collisions, have been computed from the bidimensional volume obtained in the binary images. Then, a clear characterization of the bubble size distribution at each position can be achieved calculating the bidimensional volume probability density function (Martínez-Bazán *et al.* 1999*a*)

$$\text{V.p.d.f.}\,(D) = \frac{D^2\ \text{p.d.f.}\,(D)}{\displaystyle\int_{D_{min}}^{D_{max}} D^2\ \text{p.d.f.}\,(D)\ \mathrm{d}D}\ , \tag{4.3}$$

which, in our bidimensional approach, represents the volume occupied by bubbles of size D compared to that of the entire distribution between the smallest, D_{min}, and the largest, D_{max}, bubble size detected in each window. The evolution of the V.p.d.f resulting from

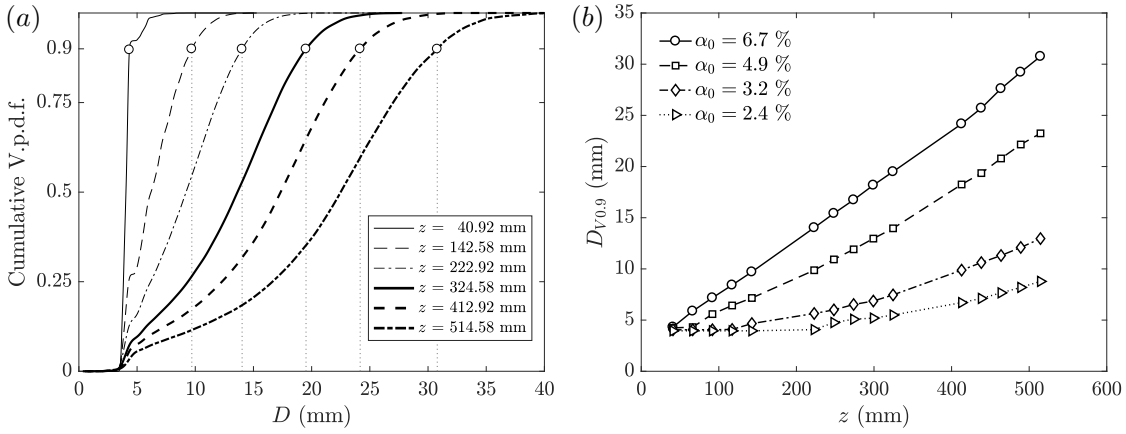

Figure 4.8: (*a*) Cumulative V.p.d.f. for $\alpha_0 = 6.7$ % at the same positions shown in figure 4.7. The diameter of bubbles such that 90% of the total bidimensional volume is contained within bubbles of smaller diameter, $D_{V0.9}$, is marked with symbols. (*b*) Downstream evolution of $D_{V0.9}$ for the different injection conditions. Notice that, no variations of $D_{V0.9}$ is observed until coalescence takes place leading to larger bubble sizes.

coalescence processes as the injected bubbles rise along the thin-gap cell is shown in figure 4.7. For the sake of clarity, we have only plotted the same six measuring locations for each experimental injection condition. Qualitatively, equivalent downstream development of the distribution is observed for all the injected air volume fractions: the narrow distribution found near the bottom of the cell progressively widens further downstream due to bubble coalescence. It can be observed that the size of the largest bubbles found in each position increases with α_0, indicating that the rate of coalescence also increases with α_0, in agreement with the information obtained from figure 4.5(a).

A detailed analysis of the downstream evolution of the bubble-volume p.d.f. helps to understand the nature of the coalescence cascades that take place once the bubble population begins to become polydisperse. Since bubbles of constant size are periodically injected at the bottom of the cell, the shape of the distribution at the lowest measuring window remains narrow with a large peak around the mean value of the injected bubbles diameter (see the measured distribution at $z = 40.92$ mm in figure 4.7(a, b), corresponding to low values of α_0). However, for larger values of α_0, secondary peaks are observed at $D = \sqrt{2}D_0$, indicating the existence of coalescence events, even at this first measuring location, which lead to the *death* of small bubbles and to the *birth* of bigger ones ($z = 40.92$ mm in figure 4.7c, d). For lower values of α_0, the first coalescence events are observed at higher locations ($z = 142.58$ mm in figure 4.7a, b), as it has been previously noted through the evolution of the total flux of bubbles, shown in figure 4.6(b). Once the coalescence process starts, the size of the largest bubble present in the distribution monotonically increases with the height, being its growing rate a function of the net degree of coalescence occurring at each previous position. In fact, the number of coalescence events involving each diameter

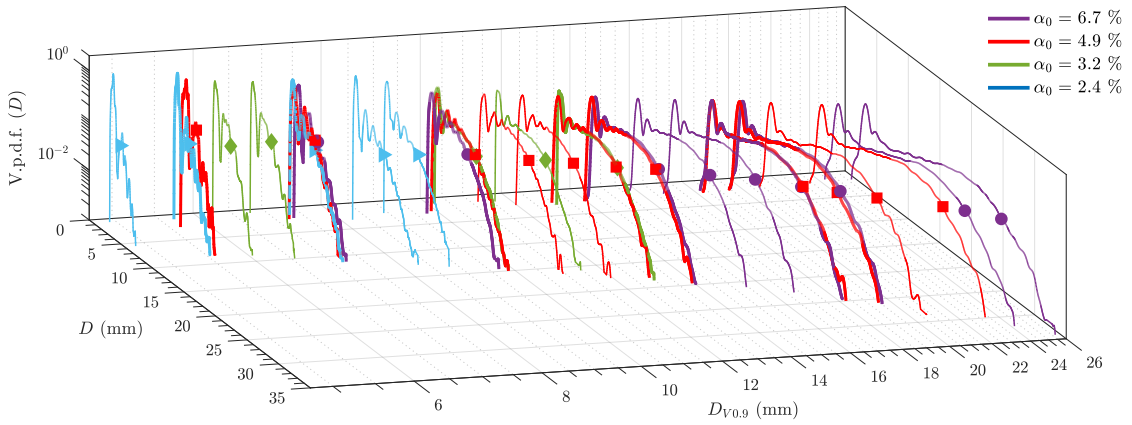

Figure 4.9: Evolution of V.p.d.f. as a function of $D_{V0.9}$. The different stages of the distribution development for all the experimental injection conditions have been plotted together showing the same trend. For clarity, only some measuring locations have been plotted and a logarithmic scale is used for the variable $D_{V0.9}$. Distributions with equal characteristic diameter $D_{V0.9}$ (thicker lines) present the same shape, independently of the value of α_0. The values of V.p.d.f. for $D_{V0.9}$ are depicted over the distributions with symbols.

present in the distribution at the previous location determines the population of the new larger bubbles, which are available for coalescence, in the next position. Therefore, the behavior of these cascades of coalescence, involving larger bubbles of the population and which leads to the *birth* of bigger ones, depends on the shape of the distribution of sizes whose downstream evolution depends on the number of coalescence events. It is worth remembering at this point that the initial bubble size distribution changes more rapidly as the injected air volume fraction increases, as it was shown in figures 4.5(a) and 4.6(b). Hence, a faster development of the V.p.d.f (D) along the cell is observed for larger values of α_0 (figure 4.7c, d) in comparison to that achieved for the lower values of the injected air volume fraction (figure 4.7a, b). Nevertheless, although the distributions evolve at different rates depending on the value of α_0, similar shapes of the distribution can be found at different positions for each α_0, corresponding to equivalent stages of the development. In fact, the distribution shapes obtained at higher positions for the lower air volume fractions, result equivalent to those observed at larger air volume fractions but at lower locations (figure 4.7). This result indicates that, since the initial bubble size distribution is nearly the same for all the experimental conditions reported in this work, a given shape of the distribution will be achieved after a given series of coalescence steps. Thus, it will take longer for low values of α_0 than for larger ones. In order to better understand the role played by the distribution shape on its evolution independently of the injection conditions, another representation of the different stages followed by the V.p.d.f., avoiding the height dependence and thus being independent of the net amount of coalescence, results necessary, as we shall explain in detail below.

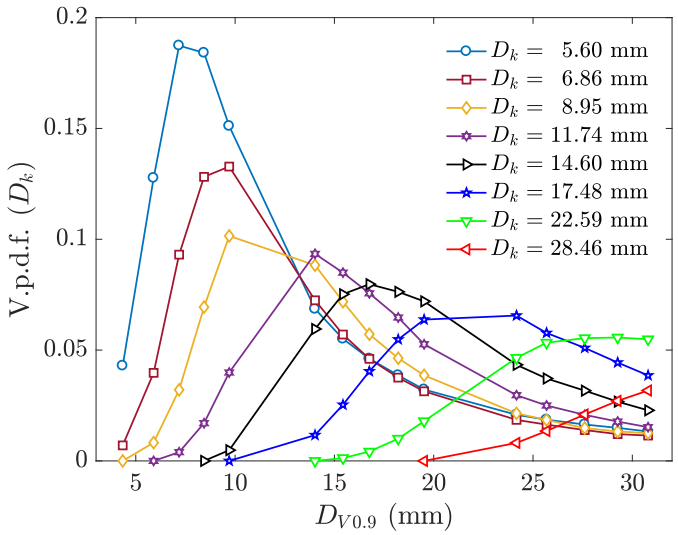

Figure 4.10: Discretized fraction of the total volume of the distribution, occupied by each bubble class larger than the injection one, at the different development stages, which are represented by their corresponding values of $D_{V0.9}$. For clarity, only the results obtained for the highest injected air fraction (i.e. $\alpha_0 = 6.7$ %) are plotted, since similar values are obtained for any other injection condition at the same development stages. Injection class not shown, color for this class not defined (see main body in Sect. 4.3.3).

The changes in the bubble size distribution between two different stages of the development are determined by the fraction of bubbles of each size involved in the cascades of coalescence. However, the distribution development depends on the shape of the distribution itself. In order to characterize the distribution shape, the cumulative V.p.d.f., defined as the fraction of volume occupied by bubbles of diameter smaller than or equal to D (Martínez-Bazán *et al.* 1999*b*), is computed at each position. From each cumulative volume probability density function, we obtain the distribution characteristic diameter $D_{V0.9}$, which represents the diameter of a bubble such that 90% of the total volume is contained within bubbles of smaller size. Figure 4.8(a) shows, as an example, the downstream evolution of the cumulative V.p.d.f. for $\alpha_0 = 6.7$ %, together with the corresponding values of the distribution characteristic diameter $D_{V0.9}$. As coalescence takes place, $D_{V0.9}$ monotonically increases giving a good representation of the largest bubble generated at the different stages of the distribution development. Moreover, figure 4.8(b) shows the values of $D_{V0.9}$ along the cell height for each α_0, reflecting the different rate of change associated to the net degree of coalescence of each injection condition. Notice that, for $\alpha_0 = 2.4\%$ and 3.2%, $D_{V0.9}$ barely changes until $z > 150$ mm, indicating that coalescence has not begun yet. However, for $\alpha_0 = 4.9\%$ and 6.7% coalescence is already observed near the injecting point.

In figure 4.9 we have represented the different stages followed by the distribution of sizes while it develops under the effect of coalescence, as a function of the corresponding

value of $D_{V0.9}$. Results from all the experimental injection conditions are plotted together. It can be observed that all the distributions follow the same developing trend with different rates of change. As mentioned previously, smaller degrees of development are achieved for lower values of α_0 (i.e. the maximum bubble size present in the distributions at the top of the measuring region results smaller than those obtained for higher values of α_0), which implies that the obtained final values of $D_{V0.9}$ are smaller too (see figure 4.8*b*). In spite of these different rates of change, associated to each injection condition α_0, equal distribution shapes are obtained for the same values of $D_{V0.9}$ independently of α_0 (figure 4.9). Considering that all the injected bubble swarms start from the same monodisperse distribution, the equal shapes reached at each development stage imply that the induced cascades of coalescence follow the same pattern. Therefore, between two stages of the development, the fraction of each size involved in the cascades of coalescence is the same for every injection condition, being determined by the shape of the distribution at the first stage.

In addition, the development of the fraction occupied by a certain bubble size larger than the injection one, reflects the fraction of daughter bubbles of this size emerging from coalescence events compared to the fraction of this size disappearing in coalescence events as a parent bubble. In order to analyze the role played by each size of the population on the cascades of coalescence we have discretized the measured bubble diameters in different size classes, as follows. The first class involves the injected bubbles. The second size class includes those diameters which arise from the coalescence of two bubbles of the first class. The rest of the classes are defined as the coalescence of bubbles coming from the two immediately preceding classes. Every class is represented by the mean value of the diameters included in the corresponding size bin, D_k. The evolutions obtained for each class are represented in figure 4.10 as a function of the corresponding value of $D_{V0.9}$. Since, as mentioned previously, the evolution of each class fraction between the different stages results similar for every injection condition, only the results obtained for $\alpha_0 = 6.7$ % are shown. Given the nature of the cascades of coalescence, the fraction occupied by each class firstly increases, as coalescence of smaller classes takes place. However, as the weight of a certain class becomes relevant in the distribution, this size is progressively involved in the coalescence cascades and eventually, as we shall explain in next sections, its diameter dominates the coalescence process, accelerating its *death* rate and thus highly decreasing its fraction in the distribution. As the fraction of the immediately larger class increases, due to the coalescence of the analyzed size, the coalescence is dominated by this new larger diameter and the decrease of the fraction of the analyzed class becomes smoother.

4.3.3 Mechanisms driving bubble collisions

As it has been described in previous sections, the evolution of the bubble swarm is driven by a coalescence process that generates larger bubbles and modifies the size distribution. These bigger bubbles end up controlling the process and giving rise to new stages of the

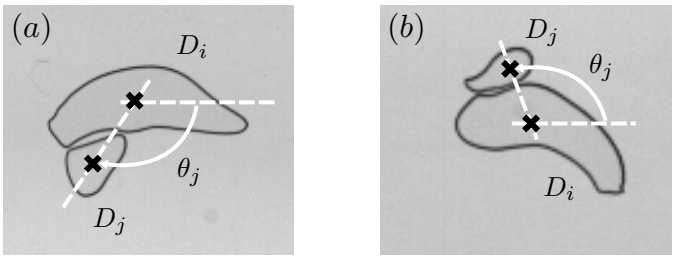

Figure 4.11: Snapshots of typical binary collisions of a large bubble of diameter D_i with a smaller one of diameter D_j. The relative position of the smallest bubble is defined as the angle θ_j under which the bubbles collide. (a) Collision driven by the wake entrainment mechanism (negative values of θ_j). (b) Collision due to buoyancy induced rise velocity difference (positive values of θ_j).

distribution development. Generally, the coalescence of two bubbles is described as a three-step process (Prince & Blanch 1990). First, the bubbles approach each other until they collide, confining a thin film of liquid between their surfaces. The bubbles keep in contact while the liquid film is drained out. Finally, once the film reaches its critical thickness, film rupture occurs resulting in coalescence. In this section we will identify the underlaying physical mechanisms which control the first stage of the process, bringing the bubbles together and inducing the collisions.

Assuming that the average liquid velocity is negligible everywhere in the cell and that turbulence cannot develop due to confinement, the sources of the relative bubble motion leading to collisions (Liao & Lucas 2010) are related to the intrinsic path oscillations of confined bubbles, that is, buoyancy induced rise velocity differences and the liquid agitation mainly induced by the bubbles wakes. In addition, the bubble deceleration effect described in Sect. 4.3.1, can be seen as a mechanism enhancing coalescence which only affects the injected bubbles while they rise along the first measuring windows. Although collision mechanisms are cumulative (Swift & Friedlander 1964), the relevance of each source can be obtained by means of a detailed analysis of the collisions detected at each measuring window. Moreover, as it has been shown in Sect. 4.3.2, the cascades of coalescence that drive the changes of the bubble size distribution between two different stages exhibit the same nature, independently of the injection conditions. Therefore, only the results obtained for $\alpha_0 = 4.9$ % are reported here, resulting equivalent to those obtained for the rest of the experimental injection conditions at the same stages of the distribution development.

It has to be pointed out that most of the collisions registered in the images involve only two bubbles, independently of the injection conditions and of the degree of development of the size distribution. Therefore, we focus on the detected binary collisions (figure 4.11). From the results of the images analysis, we obtain the characteristics of the bubbles involved in the same collision. The equivalent diameter of the largest involved bubble, D_i, and that of the smallest one, D_j, are determined from their projected areas, as it has

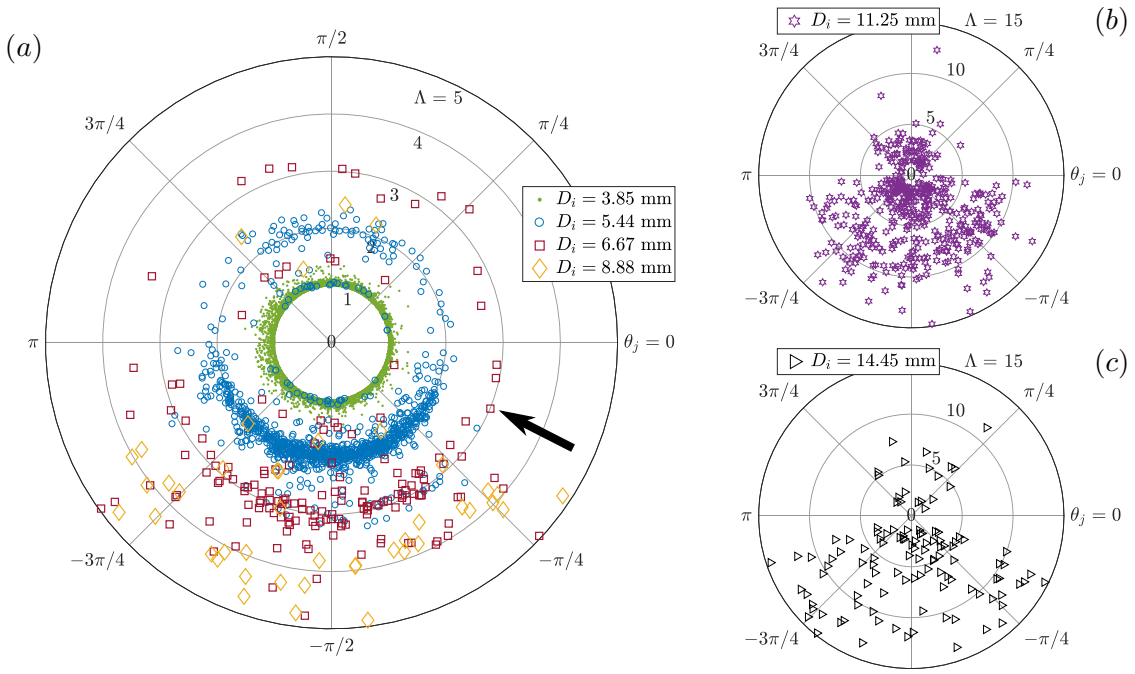

Figure 4.12: Bubble collision angle θ_j as a function of the colliding bubbles bidimensional volume ratio Λ for $\alpha_0 = 4.9$ %. The diameter of the largest bubble in each collision is represented by different symbols. (a) Map of collisions of a population of bubbles with $D_{V0.9} = 6.87$ mm. (b, c) Collisions involving bigger bubbles in a population of bubbles where $D_{V0.9} = 10.93$ mm, (b) $D_i = 11.25$ mm $\simeq D_{V0.9}$ and (c) $D_i = 14.45$ mm.

been described in Sect. 4.2.2. The relation between both sizes is characterized by means of the colliding bubbles bidimensional volume ratio $\Lambda = (D_i/D_j)^2 \geqslant 1$. In order to clearly show the results as a function of the involved bubble sizes, in addition to Λ, we discretize the measured diameter of the largest bubbles making use of the same size classes proposed in Sect. 4.3.2, each class shall be hereinafter depicted in figures with the same colors and symbols defined in figure 4.10. Finally, the angle of approach under which the bubbles collide describes the relative position of the small bubble with respect to the large one, θ_j. It is defined as the angle forming by a horizontal line crossing the centroid of the large bubble and the line going through the centroid of both bubbles (figure 4.11).

Thus, the source of each detected collision can be identified according to the relative position of the bubbles involved. Figure 4.12 shows polar plots where the collision angle, θ_j, is represented as a function of the involved bubbles volume ratio, Λ, at a certain stage of the distribution development, determined by $D_{V0.9}$. Each point represents a detected collision. The azimuthal coordinate indicates the position of the smallest bubble involved in the collision relative to the largest one. In addition, the different type of symbols represents different size classes of the largest bubble. Therefore, every collision of a certain bubble class with all the smaller (or equal) bubbles are displayed with the

same symbol, being the volume ratio of the two bubbles colliding represented by the correspondent value of Λ as the radial coordinate. For example, the point indicated with an arrow in figure 4.12(a), placed in $\Lambda \simeq 3$, corresponds to a bubble of $D_j = 3.85$ mm colliding with a larger bubble of $D_i = 6.67$ mm at $\theta_j \approx -\pi/8$ in a population of bubbles where $D_{V0.9} = 6.87$ mm.

Since the distribution starts from a nearly monodisperse swarm, the initial coalescence process takes place between bubbles of the injection size. It has been observed that the mechanisms that induce the collision between two injected bubbles are of equal nature even at stages of higher development degree, considering that this type of collision is the first step that triggers the cascade of coalescence. Figure 4.12(a) shows the collisions registered at an early stage of the development (i.e. $D_{V0.9} = 6.87$ mm). Although the size distribution presents a low development degree, the coalescence cascade has already started and the distribution has evolved reaching a maximum size class around $D_k = 8.88$ mm. It can be observed that the collisions that take place between two injected bubbles (green dots at $\Lambda \simeq 1$) do not present any preferential collision angle. This reveals an underlain mechanism leading to almost random collisions. Such a collision process highly depends on the fluctuating bubble motion, naturally driven by the path oscillations induced by vortex shedding (Roig *et al.* 2012), together with the inter-bubble distance, established through the bubble injection frequency and the injectors separation, which is progressively reduced by the deceleration effect as well as by the net bubble induced liquid agitation (Bouche *et al.* 2014). However, as larger bubbles emerge from this first coalescence step, a cascade of coalescence events is developed due to different mechanisms.

As can be observed, most of the registered collisions in which the largest bubbles belong to the second class, $D_i = 5.44$ mm, involve injection bubbles as the smallest ones (blue circles at $\Lambda \simeq 2$ in figure 4.12a). In this case, the relative positions of the smallest bubbles show that this type of collision mostly takes place with the smallest bubble coming from the bottom of the largest one, as noticed by the large density of data found in the region of negative θ_j values (figure 4.11a). This reveals a collision process driven by the so-called wake entrainment mechanism (Wu *et al.* 1998; Liao & Lucas 2010). Under this effect, the trailing small bubble, which naturally would have an ascending velocity lower than that of the leading larger one, is accelerated by the entrainment provided by the leading bubble's wake (Stewart 1995; Huisman *et al.* 2012; Filella *et al.* 2019). On the other hand, a small fraction of the detected collisions is driven by buoyancy effects, represented by those points in the region of positive θ_j values. In this case, the different rise velocity allows the large bubble to reach the small one and collide (figure 4.11b). The relevance of each mechanism as well as their evolution with the size distribution development shall be explored in figure 4.13.

Following the coalescence cascade, the collisions of the next class, which is immediately larger, $D_i = 6.67$ mm, with the rest of smaller (or equal) bubbles (red squares in

figure 4.12*a*) occur in a similar way to that described above for the previous class, being dominated by the wake entrainment mechanism. In fact, most of the collisions involve injection bubbles as the small ones, since the largest density of points are located at $\Lambda \simeq 3$. However, it should be pointed out that, at the current analyzed stage, this class corresponds to the size of the characteristic diameter $D_{V0.9}$, and some different collisions start to take place, involving the immediately previous class, $\Lambda \simeq 1.5$. This new type of collision appears as a next step in the cascade of coalescence. In this case, it can be observed a incipient number of collisions at positive values of θ_j for $\Lambda \simeq 1.5$. In general, for a certain bubble class considerably larger than the injection one, this different type of coalescence emerges at stages where the analyzed class has achieved a relevant weight in the distribution, as it was anticipated in Sect. 4.3.2. This mechanism is established by those collisions involving the analyzed class, as the largest colliding bubble, and smaller classes whose size is large enough to develop a wake sufficiently intense to trap the largest bubble. In that case, both negative and positive values of the colliding angle θ_j, describe collisions driven by the wake entrainment mechanism, the former due to the large bubble wake and the latter due to that of the small one. Figure 4.12*b* clearly displays this step in the coalescence cascade. It shows the collisions of a bubble class much larger than the injection one, $D_i = 11.25$ mm, with the rest of smaller (or equal size) bubbles, in a stage where the distribution is highly developed, $D_{V0.9} = 10.93$ mm $\simeq D_i$. Those collisions involving very small bubbles, $\Lambda > 5$, are clearly induced by the largest bubble's wake entrainment, being all the detected points located in the region of negative values of θ_j. However, for those classes closer to the analyzed one, $\Lambda < 5$, the new type of coalescence described above results relevant since the collisions are spread along both negative and positive values of θ_j, although the effect of the largest bubble's wake seems to be dominant.

Finally, the largest size class found at each stage, larger than $D_{V0.9}$, has a smaller weight in the distribution and thus fewer collisions have been detected (yellow diamonds and black triangles in figure 4.12*a*, *c*, respectively). Most of them are induced by the largest bubble's wake entrainment, although a few events at positive values of θ_j are also observed, especially for $\Lambda \leqslant 5$.

Once the main mechanisms governing the collision have been identified, their relative influence at each stage of development of the bubble size distribution can be described analyzing the evolution of the probability density function of the collision angle, θ_j. Thus, we will consider a certain bubble class, of size D_i larger than the injection one, colliding with the rest of smaller (or equal size) bubbles at different stages (figure 4.13*a*). It can be observed that the entrainment of bubbles in the wake of the large bubble (of characteristic size D_i), represented by negative values of θ_j, is the main mechanism controlling the relative bubble motion leading to collision, in accordance with the results presented in Bouche *et al.* (2012) for an homogeneous bubble swarm. However, the fraction of collisions with $\theta_j > 0$ increases as the bubble size distribution evolves and larger bubbles are formed

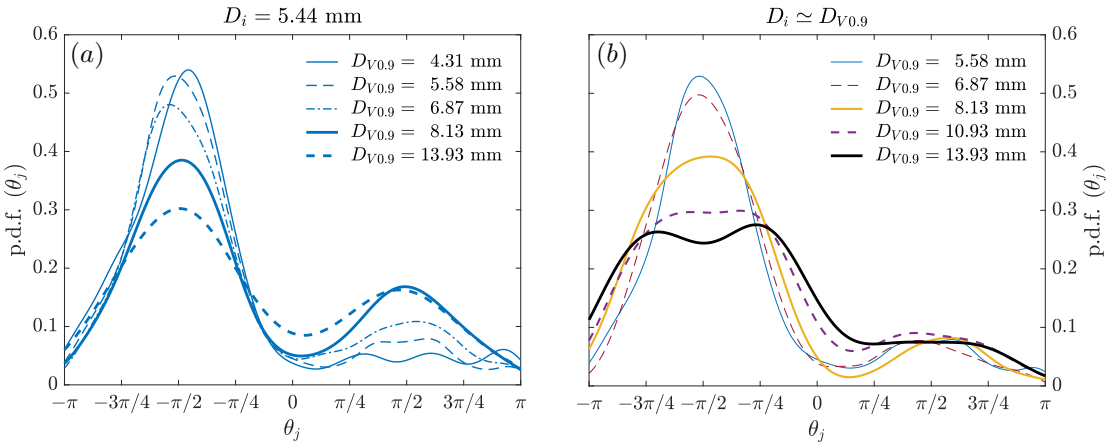

Figure 4.13: Evolution of the normalized p.d.f. of the collision angle with the bubble size distribution (i.e. $D_{V0.9}$) for $\alpha_0 = 4.9$ %, (a) for a constant value of the size of the largest colliding bubble, $D_i = 5.44$ mm and (b) for collisions where the largest colliding bubble is almost equal to $D_{V0.9}$.

due to the coalescence of smaller ones (i.e. as $D_{V0.9}$ increases). This behaviour can be explained as follows. Initially, monodisperse bubbles of diameter D_0 are injected, which start to coalesce after a given time. Once that bubbles of certain class are generated due to coalescence, their collisions with smaller bubbles driven by buoyancy effects are almost negligible and they mostly collide with bubbles that come from behind and are entrained in their wake (see case where $D_i > D_{V0.9}$ in figure 4.13a). However, as larger bubbles are generated, since their rising velocity is slightly faster than that of the smaller bubbles above them, they start to reach them increasing the number of collisions caused by buoyancy effects, occurring at $\theta_j > 0$. As the coalescence process evolves ($D_i \leqslant D_{V0.9}$ in figure 4.13a), the number of collisions of bubbles of size D_i with smaller or equal size ones that are above them, $\theta_j > 0$, keeps increasing in part due to the liquid agitation induced by the wakes of bubbles larger than D_i. This coalescence cascade process keeps taking place until the final stages, represented by very large values of $D_{V0.9}$ compared to D_i, where the number of bubbles of diameter D_i and smaller has been considerably reduced because they have already coalesced forming larger bubbles (see figure 4.10), and the coalescence events mostly involve bubbles greater than D_i. Nevertheless, the dynamics of such larger bubbles increases the dispersion in the angle of collision of bubbles of size D_i.

Similar process has been observed for each bubble class. In fact, figure 4.13(b) shows the evolution of the probability density function of the collision angle of bubbles of size $D_i \simeq D_{V0.9}$ with bubbles of the same size and smaller ones. In this case $D_{V0.9}$ represents largest bubble of the population in each step. Initially, for $D_{V0.9} = 5.58$ mm, the distribution is identical to that corresponding to $D_{V0.9} = 5.58$ mm in figure 4.13(a). As the population of bubbles incorporates larger ones, $D_{V0.9}$ increases and more collision events

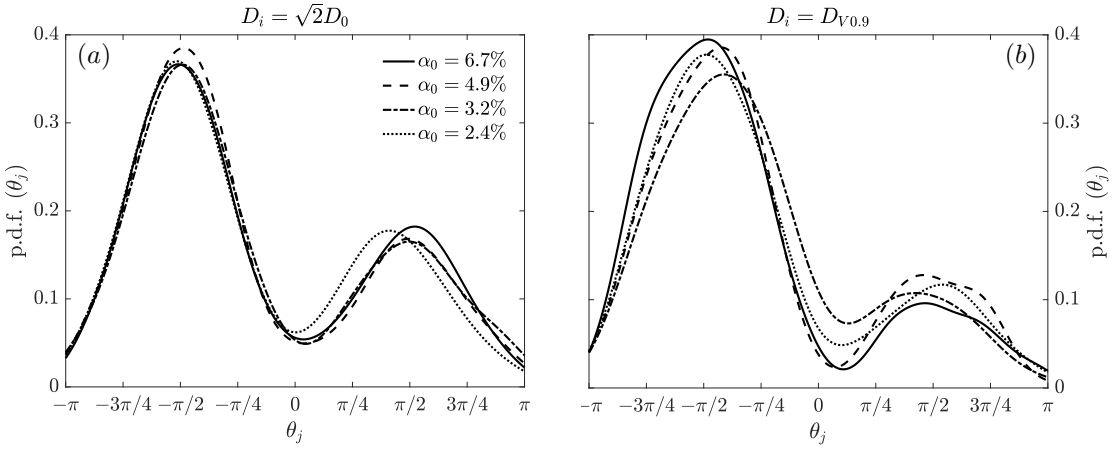

Figure 4.14: Normalized p.d.f. of the smallest bubble collision angle for various injection conditions but for equal bubble size distribution (i.e. $D_{V0.9} = 9.71$ mm), being the discretized size of the largest involved bubble: (a) $D_i = \sqrt{2}D_0$ and (b) $D_i \simeq D_{V0.9}$.

with bubbles from above take place ($\theta_j > 0$). It is worth noticing that the p.d.f.(θ_j) in the negative range ($\theta_j < 0$) evolves spreading with the size of $D_{V0.9}$, although the total probability of this region remains almost constant. This increase in the range of collision angles is due to the growth of the diameter of the larger bubble involved in the collision, D_i, and consequently the region where the wake of the bubble is able to entrain smaller ones. In addition, two incipient peaks can be observed for the largest bubbles, showing the effect of the symmetrical recirculating wake that characterizes these bubble sizes (Roig *et al.* 2012).

Finally, taking into account that the induced coalescence cascade which governs the evolution of the distribution of sizes does not depend on the injection conditions, the mechanisms leading to this coalescence process should be also equivalent. This conjecture can be corroborated by the results obtained for different experimental injection conditions, which are shown in figure 4.14. The contribution of the different mechanisms, represented through the p.d.f. of the collision angle, for various injection conditions but at the same stage of the distribution development, results almost equal for two different size classes representing small sizes of the distribution (figure 4.14a) and large sizes (figure 4.14b), respectively. The good agreement obtained in both cases confirms that the nature of the coalescence cascade depends on the size distribution although the net coalescence rate at each stage depends on the concentration of the bubble population.

4.4 Direct measurements of the rate of change of the bubble population

In the absence of dissolution, the rate of change of the population of bubbles existing in a time t, at a given position $\mathbf{x}$, $n(v, \mathbf{x}, t)$, can be described by the Population Balance Equation,

$$\frac{\partial n}{\partial t} + \nabla \cdot (\bar{\mathbf{u}}\, n) = \dot{Q}_b \; + \; \dot{Q}_c \; , \tag{4.4}$$

where $\bar{\mathbf{u}}(v, \mathbf{x}, t)$ is the mean velocity of all the bubbles of volume v and, $\dot{Q}_b(v, \mathbf{x}, t)$ and $\dot{Q}_c(v, \mathbf{x}, t)$ are the rate of change of $n(v, \mathbf{x}, t)$ due to breakup and coalescence respectively, whose expressions are given in equations (1.6) and (1.7), respectively. In the present work, the rate of change of the number density of bubbles can be written as the sum of the *Death* rate of bubbles of volume v due to their coalescence forming larger ones and due to breakage leading to a bubble pair; as well as the *Birth* rate of bubbles of volume v resulting from the coalescence of smaller ones and those bubbles of volume v' and $v - v'$, respectively, resulting from the breakage of larger ones. These terms can be expressed as,

$$D_e \;\; = \;\; - n(v) \int_0^\infty \lambda_c(v, v')\, h_c(v, v')\, n(v')\; \mathrm{d}v' - g_b(v)\, n(v) \tag{4.5}$$

$$\begin{aligned} B_i \;\; = \;\; & \frac{1}{2} \int_0^v \lambda_c(v - v', v')\, h_c(v - v', v')\, n(v - v')\, n(v')\; \mathrm{d}v' \\ & + \int_v^\infty f(v', v)\, m(v')\, g_b(v')\, n(v')\; \mathrm{d}v' \end{aligned} \tag{4.6}$$

In equations (4.5) and (4.6) only the dependence of v and v' have been indicated for convenience. Therefore, $n(v)g_c(v) = n(v)\int_0^\infty \lambda_c(v, v')h_c(v, v')n(v')\mathrm{d}v'$ is the amount of bubbles of volume v which *die* due to coalescence and $g_b(v)\, n(v)$ is the number of bubbles which *die* due to breakage. Similarly, in the B_i equation, $\int_0^v \lambda_c(v - v', v')h_c(v - v', v')n(v - v')n(v')\mathrm{d}v'$ is the number of bubbles of volume v generated from coalescence and $\int_v^\infty f(v', v)\, m(v')\, g_b(v')\, n(v')\; \mathrm{d}v'$ is the number of bubbles of volume v generated from the breakage of bigger ones. Thus, reliable models for the frequencies, g_c and g_b, are needed to properly close equation (4.4).

4.4.1 Bubble tracking velocimetry and coalescence/breakage detection

To that aim, we conducted additional experiments taking images of the swarm evolution with a high-speed camera at acquisition rates of 250 f.p.s. This recording rate is high enough to continuously follow the bubbles as they rise along the field of view. Thus, the bubbles collisions taking place as they rise can be detected and tracked to determine if the bubbles colliding separate or they coalesce, generating new larger bubbles. The experimental measurements also allow to detect breakup events, giving *birth* to smaller

daughter bubbles, although this phenomenon barely occurs in the present work. For this purpose, high-speed movies of 25 s duration were recorded at the same three positions described in Sect. 4.2.1, with equal spatial resolution and for the same injections conditions. The total duration of the experimental recordings involved an amount of analyzed bubble histories per recording position between 20 000 and 75 000, depending on the injection conditions and on the measuring location.

The history of each bubble present in the swarm was obtained by means of a specifically developed bubble tracking routine, which includes a coalescence/breakage detection algorithm, hereafter called BTV. Generically, it consists of the detection of the bubbles present in each frame k, followed by the search and identification of these bubbles in the previous frame $k-1$. For new bubbles, born in frame k either by coalescence or breakage, family trees are established between the daughter (frame k) and the parents (frame $k-1$).

More precisely, the performance of the routine involves a first step in which frame k is processed using the digital analysis described in Sect. 4.2.2. As a result, the bubbles present in this frame are detected, obtaining their centroids positions as well as their bidimensional volume. Then, every bubble is classified as *single* or *in-collision* bubble. In addition to the bubbles, the detected collisions, defined as agglomerations of two or more bubbles in direct contact (see Sect. 4.2.2), are treated as independent entities and thus their parameters are measured too, including the total number of involved bubbles. In order to facilitate the search of corresponding objects in two consecutive frames, a bounding-box containing the target object is defined for every bubble and collision. Figure 4.15 shows the BTV performance superimposed over the original grayscale image at different instants, being the zero reference time the frame in which a coalescence event takes place (figure Figure 4.15g). Although the whole field of view is processed at the same time, only a reduced region is presented, and just a few bubbles are depicted for clarity. The trajectories followed by the bubbles are represented as a succession of dots, which correspond to the centroid locations in previous frames. The solid circles denote the bubble's centroid locations in frame $k-1$. The cited bounding-boxes are plotted in figure 4.15(a-d) for two different bubbles as a red and blue boxes, respectively, while that corresponding to a collision event is shown in figure 4.15(e, f) in green. However, the bounding-box of each individual bubble involved in the collision is not depicted for simplicity. Notice that the bounding-box of the collision turns into that of the newborn coalesced bubble in figure 4.15(g) since the collision event ends up with the coalescence of the two bubbles, as shall be described in detail below.

Once every object present in frame k has been detected, the key point of the tracking routine is to search for the corresponding one in frame $k-1$. In that sense, every single and in-collision bubble must be related, at least, to one object from the previous frame. Moreover, every detected collision must be related to a previous collision or, at least, to two previous bubbles. The procedure works sequentially identifying objects, tak-

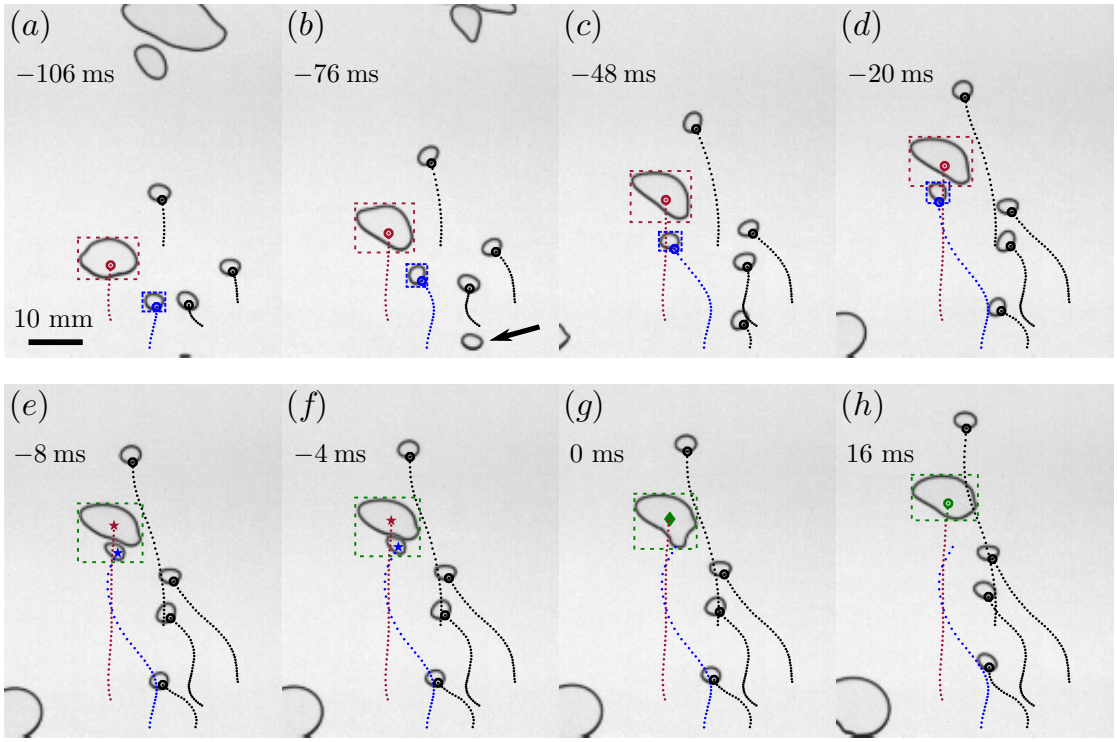

Figure 4.15: Characteristic sequence of the BTV performance showing the tracking process, superimposed over a portion of the original grayscale images at different instants. The trajectories of the properly tracked bubbles are represented by means of a succession of different dots corresponding to the bubble centroid locations in previous frames. (*a*-*d*) Examples of the correlation method applied to two different bubbles (red and blue, respectively), showing the centroid obtained in frame $k-1$ (circle) lying inside the corresponding bounding-box in frame k (dashed box). The black arrow in (*b*) indicates a detected new bubble entering the field of view. (*e*-*f*) Typical collision detected and tracked in two consecutive frames. The bounding-box of the whole collision object is shown with a dashed dark green rectangle in each frame. The identified bubbles which are involved in the collision are marked with colored stars. (*f*-*g*) Sequence of the end of a collision event due to bubble coalescence. The parent bubbles involved in the collision (colored stars) give rise to a new bubble (green diamond). (*h*) The coalesced bubble is hereafter tracked as a single bubble (green circle).

ing into account the continuity of the bubbles trajectories and the conservation of the bidimensional volume of the objects. In a first step, only single bubbles in both frames are considered. Therefore, a single bubble in frame k is related to the single one in frame $k-1$ whose centroid position falls inside the bounding-box of the bubble in frame k. Given the experimental acquisition rate, this bounding-box criteria results highly effective, even for the smallest bubbles that are accelerated in the wake of larger ones (figure 4.15*c*, *d*). However, when bubbles of very different sizes become closer (without contact), more than a centroid detected in frame $k-1$ can be contained in the bounding-box of the larger bubble in frame k. To avoid possible errors, an additional criterion based on the conservation of volume is imposed (Rodríguez-Rodríguez *et al.*, 2003). Therefore, the volume of the

corresponding bubbles in both frames must be equal. Moreover, bubbles located near the bottom edge of the field of view in frame k, which cannot be associated with any object in frame $k-1$ (see e.g. the bubble highlighted by an arrow in figure 4.15*b*), are directly classified as new bubbles just entering the analysis region. Any other single bubble that cannot be related to a previous one, is taken out for further analysis. The rest of single bubbles properly tracked are stored and removed from both frames.

Next step is devoted to collision events detected in frame k. As it has been previously stated, one of the three coalescence stages consists of the drainage of the thin liquid between the bubbles while they remain in contact. It has been observed in our experiments that the duration of this drainage stage typically exceeds the time delayed between two recording frames. Therefore, coalescence emerges from a collision which has been registered within, at least, two or three different frames. On the other hand, colliding bubbles can bounce back or slide each other without coalescing. In both cases, the detected collisions, induced through the mechanisms described in Sect. 4.3.3, can be used as a guide to determine the origin of new single bubbles found in each frame. In that sense, every collision detected in frame k, seen as an unique object, is analyzed searching for the corresponding collision object in frame $k-1$. The same correlation based on the bounding-box (frame k) and the centroid (frame $k-1$) is applied here. In addition to the volume of the whole collision, the number of involved bubbles is another parameter that must be conserved between the corresponding collision objects in both frames. If the corresponding collision is found in the previous frame, the different involved bubbles (see bubbles marked with colored stars in figure 4.15*e*, *f*) are identified as well using the same criteria used for single bubbles. On the other hand, if no corresponding collision is found in frame $k-1$, it is assumed that the collision detected in frame k is a new one occurring because two different bubbles have been brought together (figure 4.15*e*). In that case, the bubbles involved in the collision are analyzed searching for the corresponding previous single bubbles leading to the collision. Every collision properly tracked and the identified as new ones, as well as all the bubbles involved in these collisions, are stored and no further action is perform with them in the current frame. Additionally, the corresponding objects, either collisions or single and in-collision bubbles, are cleared from the previous frame.

At this point, it is assumed that all the remaining bubbles in frame k have emerged either from the breakage of a mother bubble in frame $k-1$ or from the death of a previous collision. The later gives rise to two different situations, namely death by coalescence, creating a new larger bubble, or death by the separation of the involved bubbles, leading to different single bubbles in the current frame. Both situations respectively arise from a collision in frame $k-1$ which does not have a corresponding collision object in frame k. Therefore, a forward analysis, from the previous to the current frame, is applied to the remaining collision objects in frame $k-1$. In that case, the correlation method used to track a single bubble is applied here for each bubble involved in the collision

detected in frame $k-1$, searching for the corresponding bubble in frame k. Only the remaining bubbles in frame k whose centroid falls inside the bounding-box of the analyzed collision object in frame $k-1$, are considered. If the death of the collision is due to separation, every involved bubble will be related to a corresponding single bubble in the current frame, fulfilling both the bubble bounding-box criteria as well as the bubble volume conservation. However, if collision event ends up with the coalescence of the two bubbles, the volume conservation will not be individually assessed for each involved parent bubble. Consequently, the daughter bubble emerging from the coalescence is determined as the remaining single bubble in frame k whose centroid falls inside the bounding-box of the analyzed collision object in frame $k-1$, being its bidimensional volume almost equal to the sum of those of the parent bubbles in the previous frame. A typical detected coalescence event is shown in figure 4.15(f, g). The parent bubbles involved in the collision can be seen in frame $k-1$ (figure 4.15f), being their centroids indicated by colored stars, while the newborn bubble appears in frame k (figure 4.15g), with its centroid marked with a green diamond. From this point, the new bubble appeared because of coalescence, is tracked as a single bubble (figure 4.15h).

Finally, the remaining daughter bubbles present in frame k, which appear as a consequence of the breakage of a mother bubble in frame $k-1$, are identified through a backward-forward implementation of the correlation method, following the idea proposed by Rodríguez-Rodríguez *et al.* (2003). Basically, in the breakage process, the volume of the single mother bubble is split in two different single daughter bubbles (Martínez-Bazán *et al.*, 1999*b*). In that sense, for a possible daughter bubble in frame k, the corresponding mother bubble is searched in frame $k-1$ as the larger bubble whose bounding-box includes the centroid of the analyzed daughter one. Then, the second daughter bubble is additionally searched in frame k as that whose centroid falls inside the bounding-box of the mother one and whose volume corresponds to complementary to that of the other daughter bubble, achieving together the total volume of the mother bubble. Therefore, both daughter bubbles in frame k are identified as new single bubbles appearing due to breakage, while the corresponding mother bubble in frame $k-1$ is defined as *death* due to breakage.

4.4.2 Global coalescence frequency in the swarm

The results obtained through the tracking algorithm, BTV, represent the history of every detected bubble along the field of view of each recording position. The information stored for each bubble includes the two dimensional volume, the centroid location, the bubble velocity components obtained by differentiation, as well as the bubble lifespan and the way in which its birth and death take place. In addition, family trees are established for each newly generated bubble, including the parents in a birth from coalescence, the mother and the sister in a birth from breakage, and the daughters if the analyzed bubble dies due

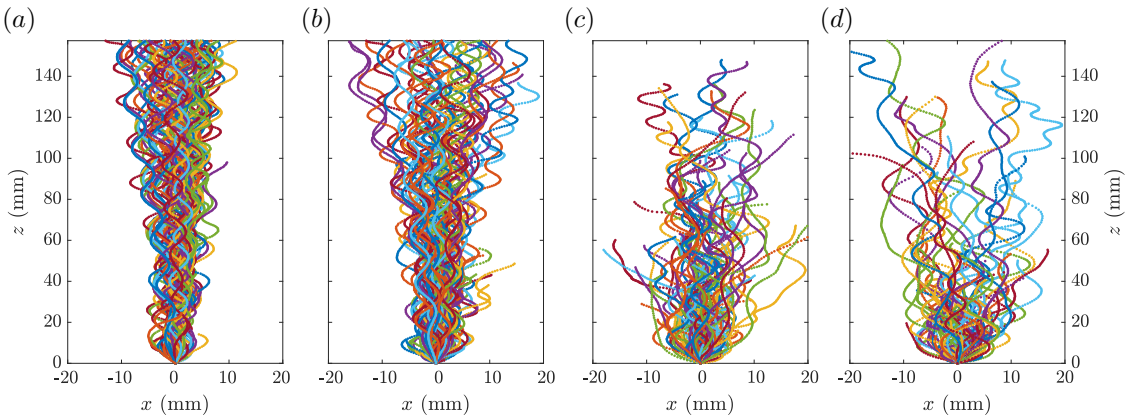

Figure 4.16: Superimposed trajectories of 100 random bubbles detected along the field of view of the first recording position, $z < 160$ mm, for the different injection conditions, (a) $\alpha_0 = 2.4$ %, (b) $\alpha_0 = 3.2$ %, (c) $\alpha_0 = 4.9$ % and (d) $\alpha_0 = 6.7$ %. The trajectory is defined as a succession of points corresponding to the bubble centroid at each instant. The origin is defined as the position where the bubble is detected for the first time.

to the cited events. The same 15 measuring windows described in Sect. 4.2.2 are used to spatially discretize the results.

As an example of the obtained results, figure 4.16 shows a set of random bubble trajectories for each injection condition registered at the first recording position. They have been displaced to have the same origin. It can be observed that the horizontal dispersion of the bubbles increases with the injected air volume fraction and with the vertical position, showing the effect of the hydrodynamics interactions driven by the agitation induced in the liquid by the vortex shedding and the wakes behind the bubbles. The bubble lifespan is typically larger for the smaller air volume fractions (figure 4.16a, b), since the number of coalescence events is still low at this recording position. The trajectories show the characteristic path oscillations similar to those found for an equivalent size isolated bubble (Roig *et al.*, 2012), indicating the weak effect of the hydrodynamic interactions at these low void fractions. However, the degree of coalescence substantially increases with the injected air fraction, giving rise to much shorter trajectories (figure 4.16c, d). The increment of the induced liquid agitation, that appears as the distribution of sizes become wider, can be observed through the bubble trajectories, which progressively lose the characteristics horizontal oscillations due to the hydrodynamic interactions.

Moreover, the tracking method allows a direct analysis of the coalescence events. For that purpose, besides the history of every bubble, additional information related to each detected collision is stored during the BTV performance. As mentioned before, every detected collision is treated as an individual entity, obtaining the position at which it initially occurs as well as the corresponding information of the involved bubbles. This information, together with the collisions lifespans as well as the positions and types of

mechanisms that lead to their end, can be used to determine $\lambda_c(v.v')$ and $h_c(v, v')$ in equations (4.5) and 4.6. In addition the BTV code can be used to extrapolate the number of bubbles of volume v which die due to coalescence, and the mean coalescence frequency of all bubbles present at each position, $\langle g_c \rangle_B$. This value can be seen as the mean frequency at which the bubble population changes due to coalescence of parent bubbles, whatever their sizes, $\langle g_c \rangle_B = \int_0^\infty n(v) g_c(v) \mathrm{d}v$. It has been previously stated that daughter bubbles which are born due to coalescence, come from previous binary collisions. In this sense, the detected number of collisions which end up in coalescence, N_c, during the total time of analysis, T_a, in a population of N_B bubbles, represent half of the net amount of bubbles dying due to coalescence per unit time and per unit window area, $N_B \langle g_c \rangle_B / 2$, which corresponds to the first integral term of the r.h.s. in equation (4.5), averaged over all bubble sizes present in the population. Therefore, the mean bubble coalescence frequency can be directly obtained from the experimental measurements as

$$\langle g_c \rangle_B = \frac{2 N_c}{N_B \, T_a}. \tag{4.7}$$

On the other hand, the collisions tracked which do not end-up coalescing can be used for further analysis focused on the collision efficiency. Although not reported in this work, preliminary results reveal that, due to the confinement imposed by the experimental cell, as bubbles cannot avoid each other out of plane, collision efficiencies higher than those found in unconfined swarms have been observed (see Liao & Lucas, 2010, and references therein).

In a similar way, the second integral term of the r.h.s. in equation (4.5), averaged over the entire population of bubbles, can be expressed as the amount of bubbles per unit time that die due to breakup. Thus, the direct measurement of all the bubbles identified as dead due to breakup, N_b, allows us to obtain the mean breakup rate as,

$$\langle g_b \rangle_B = \frac{N_b}{N_B \, T_a}. \tag{4.8}$$

Since both the coalescence and the breakage events are binary, the birth terms due to both processes in equation (4.6), averaged over all the sizes, can be obtained as $N_B \langle g_c \rangle_B$ and $2 N_B \langle g_b \rangle_B$, respectively. In addition, the validity and convergence of the results obtained by means of the tracking analysis of the experiments performed at high-frequency image acquisition, can be check by comparing both sides of the equation (4.4) averaged over all bubble sizes. To that aim, the l.h.s. in the averaged PBE can be achieved by integration of equation (4.4) from the minimum bubble volume to the maximum possible one. Thus, applying the Leibnitz rule for integration and using the previously obtained expressions for the global terms of *Death* and *Birth*, in the steady state situation of interest here, the averaged PBE simplifies to

$$-\frac{1}{N_B} \frac{\partial \left(\bar{U}_z \, N_B \right)}{\partial z} = \langle g_c \rangle_B - \langle g_b \rangle_B \, , \tag{4.9}$$

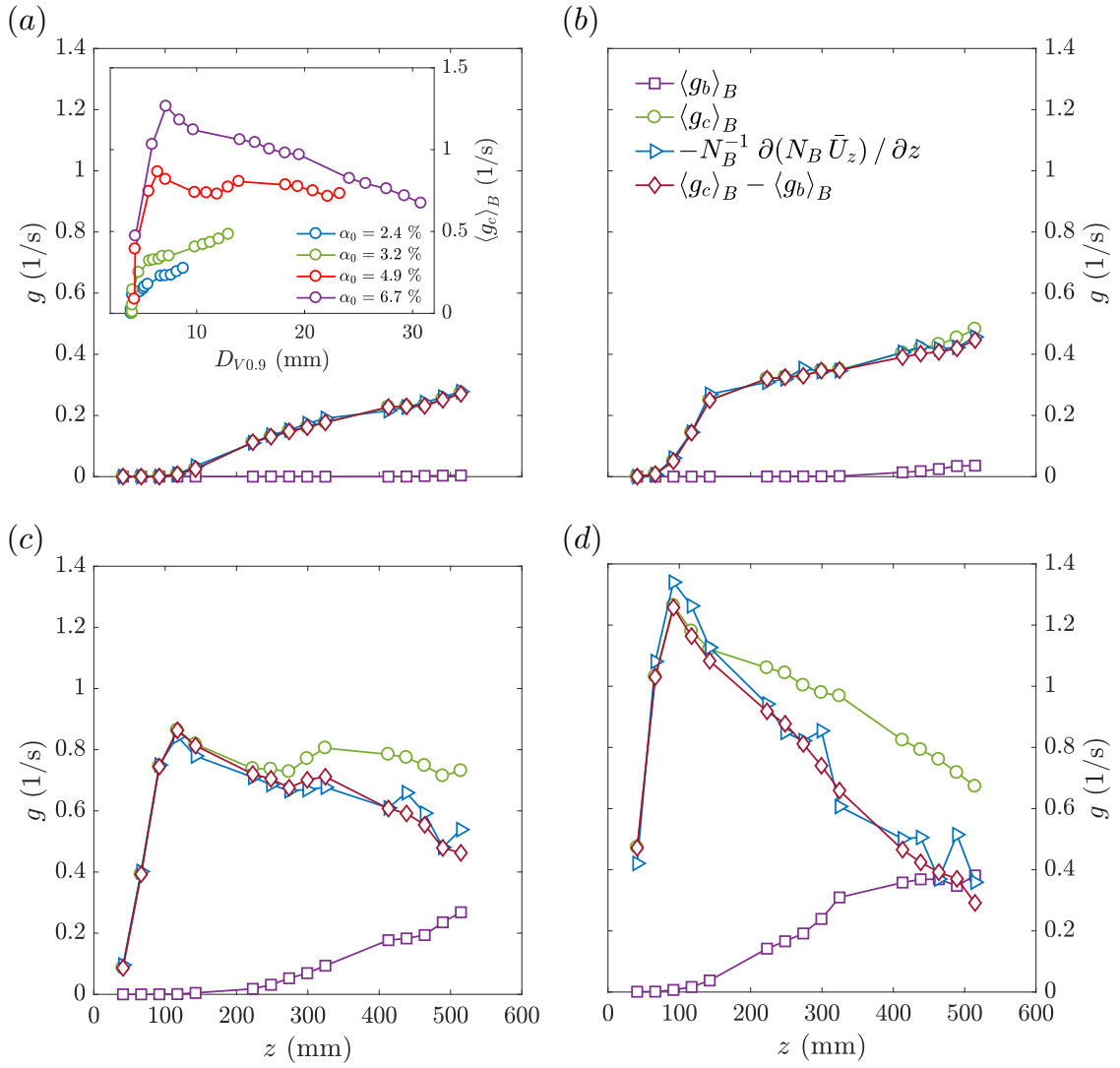

Figure 4.17: Downstream evolution of the different frequencies of change involved in the PBE averaged over all bubble sizes (Eq. 4.9), for the experimental injection conditions, (*a*) $\alpha_0 = 2.4$ %, (*b*) $\alpha_0 = 3.2$ %, (*c*) $\alpha_0 = 4.9$ % and (*d*) $\alpha_0 = 6.7$ %. The inset in (*a*) shows the mean coalescence frequency as a function of the stage of development of the bubble size distribution, represented by its characteristic diameter $D_{V0.9}$, for the different injected air volume fractions.

being $\bar{U}_z$ the mean rising velocity of the bubbles present in the measuring window. This mean velocity is obtained from the BTV code, using two different methods: 1) computation of the mean value of the ascending velocity signals averaged over the residence time of the bubbles in the measuring window and, 2) averaging the instantaneous velocity of all the bubbles in each window of an image, for a large number of uncorrelated images, such that the time from one images to the following one is larger than the bubble residence time in the window. Both methods provided identical values of $\bar{U}_z$. It is worth highlighting that this mean bubble velocity $\bar{U}_z$, directly computed from the detected bubbles, differs from

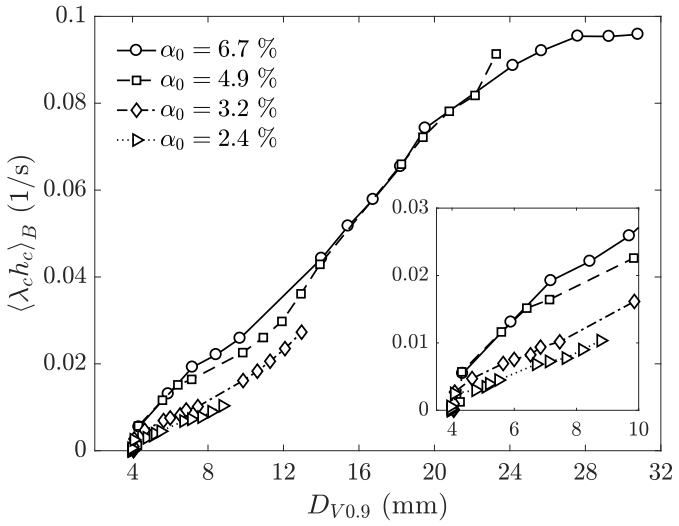

Figure 4.18: Global coalescence frequency per bubble number directly obtained from the coalescence events registered at the different development stages of the distribution of sizes, which are represented by their corresponding values of $D_{V0.9}$, for all the experimental injection conditions. The inset represents a zoom of the region of low values of $D_{V0.9}$, highlighting the effect of the injected air volume fraction.

that estimated by equation (4.2), for the whole gas phase at each position, $\langle U_g \rangle$. This discrepancy increases as the range of bubble sizes increases (i.e as the size distribution becomes wider), since $\langle U_g \rangle$ represents the velocity weighted by the bubble volume while $\bar{U}_z$ is weighted by the number of bubbles.

Figure 4.17 shows the different terms in both sides of equation (4.9), evaluated at different measuring locations, for all the experimental injection conditions. As expected, an excellent agreement is observed between both sides of the equation (triangles and diamonds, respectively). This outcome confirms the validity of the experimental procedure, as well as the effectiveness of the developed bubble tracking method and the convergence of the results obtained. In addition, it can be noticed that breakup events (purple squares) also take place in the swarm, especially for the higher values of the injected air fraction (figure 4.17c, d). As previously mentioned, the evolution of the bubble population is clearly dominated by coalescence. Indeed, the position at which a certain shape of the size distribution is reached depends on the number of coalescence events (see Sect. 4.3.2), which is, in turn, driven by the global coalescence frequency, $\langle g_c \rangle_B$, in the previous positions. However, the inset in figure 4.17(a) shows that the global coalescence frequency, expressed as a function of $D_{V0.9}$ or similarly as a function of the size distribution, evolves differently for each injection condition. This reveals the important roles played by the bubble concentration, $\alpha(z)$ and the bubble size distribution, $n(v, z)$, at each position.

In order to extract useful information on the hydrodynamics controlling the collisions, from the direct experimental measurements, the effect of the bubble concentration should be isolated from the measured global coalescence rate, $N_B \langle g_c \rangle_B$. To that end, considering

only those collisions which lead to coalescence, it can be defined the global basic coalescence frequency (Valentas & Amundson, 1966) as, $\langle \lambda_c h_c \rangle_B = \langle g_c \rangle_B / N_B$, which represents an averaged value of the frequency per bubble number at which a bubble of any size coalesces with any other bubble, whatever its size. The values of this averaged coalescence frequency obtained at each development stage of the size distribution, represented by its characteristic diameter $D_{V0.9}$, are plotted in figure 4.18 for every experimental injection condition. Similar evolution with $D_{V0.9}$ is found for the different injected air fractions. Generally, as stated in Sect. 4.3.3, the coalescence process is dominated by the wake entrainment mechanism by which a trailing bubble is accelerated in the wake region of a leading one (Stewart, 1995; Wu *et al.*, 1998). In this case, the characteristic approaching velocity, U_r, generically defined in equation (1.11), depends on the involved bubble sizes, on the distance between them and on the liquid velocity in the wake region, which in turn depends on the leading bubble diameter (Wang *et al.*, 2005; Huisman *et al.*, 2012; Bouche *et al.*, 2012; Filella *et al.*, 2019). Since the induced cascades of coalescence are eventually dominated by the large bubbles of the distribution properly described through $D_{V0.9}$, the increasing evolution of the coalescence frequency with $D_{V0.9}$ found in figure 4.18 is in accordance with the results obtained in the low-frequency image acquisition experiments shown in Sect. 4.3. Finally, there exists a slight increment of the coalescence frequency with the injected air volume fraction, which can be clearly noticed in the zoomed area represented in the inset of figure 4.18. Since this effect occurs even for equal values of $D_{V0.9}$, it could be directly related to the decrease of the inter-bubble distance for higher air volume fractions, reducing the approaching time and thus increasing the coalescence frequency. This represents an actual effect associated to the bubble concentration, not necessarily simply related to a linear effect of the total number of bubbles in the measuring windows. Furthermore, the net degree of liquid agitation induced by the rising bubble swarm increases with the air fraction (Bouche *et al.*, 2012, 2014), which leads to larger horizontal dispersion of the bubbles (see figure 4.16) and thus promoting the bubble collision. However, as the distribution of sizes becomes wider due to coalescence, i.e. as $D_{V0.9}$ increases, the number of bubbles per position substantially decreases (see figure 4.5*a*) and thus the inter-bubble distance increases. At the same time, as $D_{V0.9}$ increases, the larger bubbles in the distribution become bigger and their wakes stronger, so the wake effect clearly dominates the coalescence and the rest of effects result negligible (see values of the coalescence frequency for $D_{V0.9} > 14$ mm in figure 4.18).

In addition to this description of the evolution of the global coalescence frequency with the development of the bubble sizes distribution, further analysis of the results of the high-speed measurements is still in progress. Thus, reliable coalescence models for the coalescence frequency are expected to be derived, since the main physical ingredients involved in the process have been discerned and they can be directly obtained from the experimental measurements described here. In fact, the detailed analysis can be easily

extended to the coalescence frequency related to each pair of bubble sizes, to obtain closure models for the present confined flow configuration. To that aim, the collision frequency of each size class, defined in Sect. 4.3.2, are being analyzed, instead of the coalescence frequency averaged over the whole bubble population, studied in this work.

Moreover, the rich information provided by the developed tracking method offers well-converged probability density functions of the bubble velocity, obtained for each discretized size class. Although not reported in this work, preliminary results reveal that the vertical velocity fluctuations p.d.f. for each bubble size resembles that of liquid velocity fluctuations in bubbly flows (Bouche *et al.*, 2012, 2014). They result clearly asymmetric, with strong upward fluctuations commonly attributed to interactions with bubble wakes (Zenit *et al.*, 2001; Risso & Ellingsen, 2002; Riboux *et al.*, 2010; Mercado *et al.*, 2010; Risso, 2016, 2018). In addition, their evolution with the development of the size distribution seem to scale with the mean velocity of bubbles whose size is equivalent to the corresponding $D_{V0.9}$, confirming that the relative velocity U_r driving the bubble collisions are controlled by the vertical liquid fluctuations induced in the wake of the large bubble of the distribution.

4.5 Conclusions

In this Chapter, the downstream evolution of the population of bubbles within a confined swarm of bubbles rising at high-Reynolds numbers driven by buoyancy, has been deeply analyzed. To that aim, an exhaustive experimental study has been carried out in a quasi two-dimensional thin gap cell filled with pure distilled water. Four different injection air flow rates have been described to determine the influence of the injected air volume fraction on the initially monodisperse bubble swarms.

An statistical analysis of the characteristic parameters of the bubble swarms at different downstream positions has been performed. It was based on thousands of uncorrelated images in which every single bubble, as well as the ones involved in collision events, have been detected and analyzed by means of a specially developed image processing routine. It has been found that most of the collisions involve only two bubbles. Moreover, the global downstream evolution of the swarm has been characterized through the mean number of bubbles at each position. It has been found that as bubble collisions take place, the number of bubble decreases due to the coalescence, depending its downstream evolution on the injected air volume fraction. In fact, for larger air fractions, the bubble-bubble interactions giving rise to coalescence begin earlier than in the cases at lower air fractions. Furthermore, the rate at which the bubble swarm changes has been found to increase with the mean number of bubbles of the population.

Moreover, the evolution of bubble size distribution has also been analyzed by means of the characteristic diameter $D_{V0.9}$. As larger bubble sizes are generated due to coalescence, the distribution becomes wider, following an evolution whose shape does not depend on

the number of bubbles of the population. Indeed, equivalent distribution shapes has been found for bubble populations with similar $D_{V0.9}$, independently of the mean number of bubbles.

In addition, the underlying mechanisms leading to bubble collision have been determined performing a statistical analysis of the collision angle between the involved bubbles. It has been observed that the collisions occurring when the swarm remains monodisperse are induced by the oscillatory motion of the bubbles, as well as by the agitation induced in the liquid by the bubble vortex shedding. As larger bubbles are created, the wake entrainment of large bubbles has been identified as the main mechanism leading to collisions. In fact, the coalescence process at each position is dominated by the larger bubbles in the population, nearly described by the corresponding $D_{V0.9}$, with most of the collisions taking place with the smaller bubbles being accelerated in the wake region of the larger ones.

Finally, in order to determine the rate of change of the bubble population, additional experiments using a high-frequency image acquisition system have been performed. A bubble tracking algorithm has been specially developed which allows the detection of every coalescence and breakage event taking place at each measuring location. Considering the whole bubble population, the global coalescence rate has been found to highly depend on the bubble concentration and the size distribution, being its downstream evolution different for each injection condition. However, the basic coalescence frequency per bubble number shows similar trend for different injected air volume fraction. More precisely, and according to the previous results, the coalescence frequency is controlled by the large bubbles in the population, being the characteristic approaching velocity between colliding bubbles determined by the liquid velocity induced in their wake regions.

CHAPTER
FIVE

Conclusions and future work

5.1 General conclusions

This PhD thesis presents experimental studies focused on the improvement of the current knowledge of the dynamics of the bubble formation process and the evolution of a population of bubbles driven by coalescence. In this sense, in the first part, two different methodologies have been developed in order to externally control the bubble generation, selecting both the formation frequency and the bubble size. The effects of the introduced mechanisms have been deeply analyzed, describing the new established bubbling processes through the characteristic parameters of the forcing method. In the second part, the evolution of the population of bubbles in a confined bubble swarm has been explored, leading to the identification of the main mechanisms which drive the bubble interaction and their subsequent coalescence.

Chapter 2 describes a forcing method which is able to control the bubbling process in planar co-flow configurations. Its performing is based on the modulation of the water velocity which induces periodic perturbations of the air-water interface, leading to the bubble detachment at the prescribed frequency. To that aim, a forcing device has been implemented in a planar water-air-water co-flow configuration. A wide range of natural bubbling regimes, characterized by the Weber number, $We = \rho_w u_n^2 H_o/\sigma$, and the water-to-air velocity ratio, $\Lambda = u_n/u_a$, have been forced at different frequencies to establish the corresponding values of the forcing amplitude, ε_c, that control the generation of monodisperse bubbles at the selected frequency, f_f. The experimental results indicate that the required amplitude to achieve an effective bubbling process depends on the selected frequency and on the air velocity, as an effect related to the underpressure induced by the air stream at the nozzle exit. These dependencies have been confirmed when the dimensionless critical amplitude, $\epsilon_c = \varepsilon_c/u_n$, is expressed as a function of $\Lambda\, St^2$, showing that $\epsilon_c \propto \Lambda\, St^2$. The effects of the forcing mechanism over the liquid stream have been described by means of a one-dimensional model of the liquid sheet interface. It has been found that the air stream has an important influence on the transverse dynamics of the air-water interface. However, it has an almost negligible effect on the longitudinal dynamics.

In order to explore different ways of actuation and complementary geometries of the configuration, in Chapter 3 an alternative forcing method has been implemented in an

axisymmetric air-water co-flowing jet. In this case, the external actuation is based on the periodic variation of the pressure in the feeding gas phase, which leads to a modulation of the air flow rate towards the forming bubble. It has been shown that the bubble generation frequency, as well as the volume of the obtained monodisperse bubbles can be independently controlled, substantially reducing the strong undesired influence of the injector geometry. In addition, two different bubble breakup regimes, namely mode M1 and mode M2, have been observed, depending on the unperturbed flow conditions and on the demanded frequency. Bubble volume reductions up to 80% of the corresponding volume obtained for the same unperturbed flow conditions, have been achieved under the effect of this forcing method. The forced bubbling process has been characterized in terms of the distance from the injector at which the bubble pinch-off occurs, i.e. the intact length, l_i. A scaling law for this length, $l_i/r_o \sim St^{-1}\Lambda^{1/5}We^{1/4}$, has been proposed. This result allows us to determine the particular conditions under which the breakup mode M2 is triggered. This mode is understood as an interesting alternative since it allows the production of very uniform bubbles under flow conditions which are not enabled for the corresponding unperturbed case, overcoming the limitation imposed by the geometry of the injector. Finally, the forced bubbling regime within the breakup mode M1 has been modelled by means of the inviscid form of the spherical Rayleigh-Plesset equation. The results show that the forcing effect assists the bubble formation process, boosting both the initial overpressure and the subsequent pressure decrease. This leads to a rapid formation of the neck that eventually collapses, detaching a bubble.

Finally, Chapter 4 is focused on the analysis of the collective dynamics of confined bubbles in a two-dimensional swarm. This particular confined configuration allows the direct measurement of the events that drive the evolution of the bubble size distribution. Major changes of the bubble size probability density function have been observed along the vertical direction, mainly caused by bubble coalescence. An statistical analysis of the characteristic parameters of the bubble swarm, as well as of the collisions occurring between bubbles at different downstream positions, has revealed the important role of the coalescence on the evolution of the size distribution. These coalescence processes have been found to be governed by the wake entrainment mechanism, by which the smaller bubbles are accelerated towards the larger ones in the wake region of the largest bubbles present in the population. In addition, the coalescence frequency per bubble number has been determined by means of direct measurements of every coalescence event that takes place for each stage of the distribution of sizes. A strong dependency on the larger sizes present in the distribution has been found for the coalescence frequency, confirming that the coalescence process is controlled by the liquid velocity induced in the wake regions of the largest bubbles.

5.2 Future work

Many interesting questions have emerged during the development of this work. The main lines of investigation that arise from the present thesis are summarized here.

The first further step in this research implies the application of the forcing method proposed in Chapter 2 to the configuration presented in Chapter 3. In this sense, the velocity of the outer co-flowing liquid stream could be modulated while the inner air stream remains externally unperturbed but with the air flow rate varying as an effect of the growing bubble dynamics. Therefore, it is expected a better performance of the forcing effect thanks to the surface tension acting on the closing bubble neck. Additionally, the forced bubbling regime in the breakup mode M2 offers the best scenario to implement the forcing method based on the modulation of the water stream, taking into account that most of the noise in the water stream would be suppressed under the velocity modulation. In that case, larger intact ligaments are expected to be formed for larger values of Λ, increasing the range of flow conditions prone to be forced in the breakup mode M2.

In addition, it has to be pointed out that the forcing method presented in Chapter 3 makes use of sinusoidal modulations of the feeding chamber pressure simply as an effect of the loudspeaker performance. Since the role played by the feeding air pressure modulation on the bubbling process has been described in the present work, different methods to actively vary the feeding air flow rate during the bubbling cycle could be used to reproduce the necessary conditions that lead to the bubble pinch-off. In that sense, a system which is able to induce only the decrease of the air flow rate while the overpressure is simply generated by the dynamics of the neck collapse, seems to be the most interesting procedure.

The forcing methodologies presented in this work have been implemented in unbounded co-flow configurations. However, they could be easily extrapolated to any other configuration. Specifically, those configurations in which the bubbles are generated from the tip of a highly-stretched meniscus, such us the flow-focusing, present conditions in which the forcing methods are expected to perform in a very efficient way, demanding lower forcing amplitudes than in the cases shown in this work.

Concerning the bubble coalescence in confined swarms, it remains the most open issue of this work. In fact, the well converged direct measurements of the coalescence processes between the different sizes present in the distribution allows a detailed analysis of the coalescence frequency of any pair of bubble sizes, $h_c(v, v')$, as a function of the size distribution of the population. In addition, although the time resolution of our measurements does not provide accurate values of the duration of the film drainage, t_d, an estimation of the collision efficiency, $\lambda_c(v, v')$, could be obtained by considering the detected collisions which result in separated bubbles. The dependency on both sizes, v and v' respectively, and on the distribution of sizes could offer interesting information on the influence of the liquid agitation over the duration of contact, t_{exp}. Detailed information on $\lambda_c(v, v')$ and

$h_c(v, v')$ can be used to develop accurate coalescence models to be implemented in the population balance equation.

Moreover, as mentioned in Sect. 4.3.1, the analysis of the velocity fluctuations p.d.f.s for each bubble size for similar distributions of sizes but as a function of the air volume fraction, opens a very interesting research line that, to the best of the author's knowledge, has not been previously studied in this kind of heterogeneous confined bubble swarms. This study could be followed by measurements of the velocity field in the liquid phase, in order to better determine the influence of the wakes in the bubble approaching velocity. Additionally, the bubble dispersion as well as the preferential distribution along the horizontal direction deserve a further analysis.

Bibliography

Abe, K. & Sanada, T. 2015 The mechanism of bubble generation using a slit elastic tube and an acoustic pressure wave in the gas phase. *Chem. Eng. Sci.* **128**, 28–35.

Alméras, E., Cazin, S., Roig, V., Risso, F., Augier, F. & Plais, C. 2016 Time-resolved measurement of concentration fluctuations in a confined bubbly flow by LIF. *Int. J. Multiphase Flow* **83**, 153–161.

Alméras, E., Risso, F., Roig, V., Plais, C. & Augier, F. 2018 Mixing mechanism in a two-dimensional bubble column. *Phys. Rev. Fluids* **3** (7), 074307.

Åmand, L., Olsson, G. & Carlsson, B. 2013 Aeration control–a review. *Water Sci. Technol.* **67** (11), 2374–2398.

Basaran, O. A. 2002 Small-scale free surface flows with breakup: drop formation and emerging applications. *AIChE J.* **48**, 1842–1848.

Berberović, E., van Hinsberg, N. P., Jakirlić, S., Roisman, I. V. & Tropea, C. 2009 Drop impact onto a liquid layer of finite thickness: Dynamics of the cavity evolution. *Phys. Rev. E* **79** (3), 036306.

Bergmann, R., Andersen, A., Van der Meer, D. & Bohr, T. 2009 Bubble pinch-off in a rotating flow. *Phys. Rev. Lett.* **102** (20), 204501.

Bhunia, A., Pais, S., Komotani, Y. & Kim, I. 1998 Bubble formation in a coflow configuration in normal and reduced gravity. *AIChE J.* **44**, 1499–1509.

Bolaños-Jiménez, R., Sevilla, A., Gutiérrez-Montes, C., Sanmiguel-Rojas, E. & Martínez-Bazán, C. 2011 Bubbling and jetting regimes in planar coflowing air–water sheets. *J. Fluid Mech.* **682**, 519–542.

Bolaños-Jiménez, R., Sevilla, A. & Martínez-Bazán, C. 2016 Modeling of the bubbling process in a planar co-flow configuration. *Int. J. Multiphase Flow* **82**, 86–92.

Bolaños-Jiménez, R., Sevilla, A., Martínez-Bazán, C. & Gordillo, J. M. 2008 Axisymmetric bubble collapse in a quiescent liquid pool. Part II: Experimental study. *Phys. Fluids* **20**, 112104.

Bongiovanni, C., Dominguez, A. & Chevaillier, J.-P. 2000 Understanding images of bubbles. *Eur. J. Phys.* **21** (6), 561.

Bouche, E., Cazin, S., Roig, V. & Risso, F. 2013 Mixing in a swarm of bubbles rising in a confined cell measured by mean of PLIF with two different dyes. *Exp. in Fluids* **54**, 1552.

Bouche, E., Roig, V., Risso, F. & Billet, A. M. 2012 Homogeneous swarm of high-Reynolds-number bubbles rising within a thin gap. Part 1. Bubble dynamics. *J. Fluid Mech.* **704**, 211–231.

Bouche, E., Roig, V., Risso, F. & Billet, A. M. 2014 Homogeneous swarm of high-Reynolds-number bubbles rising within a thin gap. Part 2. Liquid dynamics. *J. Fluid Mech.* **758**, 508–521.

Bush, J. W. M. & Eames, I. 1998 Fluid displacement by high Reynolds number bubble motion in a thin gap. *Int. J. Multiphase Flow* **24** (3), 411–430.

Canny, J. 1986 A computational approach to edge detection. *IEEE Trans. Pattern Anal. Mach. Intell.* (6), 679–698.

Castrejón-Pita, A. A., Castrejón-Pita, J. R. & Hutchings, I. M. 2012 Breakup of liquid filaments. *Phys. Rev. Lett.* **108** (7), 074506.

Castrejón-Pita, J. R., Martin, G. D., Hoath, S. D. & Hutchings, I. M. 2008 A simple large-scale droplet generator for studies of inkjet printing. *Rev. Sci. Instrum.* **79** (7), 075108.

Chaudhary, K. C. & Maxworthy, T. 1980*a* The nonlinear capillary instability of a liquid jet. Part 2. Experiments on jet behaviour before droplet formation. *J. Fluid Mech.* **96** (2), 275–286.

Chaudhary, K. C. & Maxworthy, T. 1980*b* The nonlinear capillary instability of a liquid jet. Part 3. Experiments on satellite drop formation and control. *J. Fluid. Mech.* **96** (2), 287–297.

Chesters, A. K. 1991 Modelling of coalescence processes in fluid-liquid dispersions: a review of current understanding. *Chem. Eng. Res. Des.* **69** (A4), 259–270.

Chesters, A. K. & Hofman, G. 1982 Bubble coalescence in pure liquids. *Appl. Sci. Res.* **38**, 353–361.

Chong, Z. Z., Tor, S. B., Loh, N. H., Wong, T. N., Gañán-Calvo, A. M., Tan, S. H. & Nguyen, N.-T. 2015 Acoustofluidic control of bubble size in microfluidic flow-focusing configuration. *Lab Chip* **15** (4), 996–999.

Chuang, S. C. & Goldschmidt, V. W. 1970 Bubble formation due to a submerged capillary tube in quiescent and coflowing streams. *J. Basic Engng.* **92** (4), 705–711.

Clift, R., Grace, J. R. & Weber, M. E. 1978 *Bubbles, drops and particles*. Dover Publications Inc.

Colella, D., Vinci, D., Bagatin, R., Masi, M. & Bakr, E. A. 1999 A study on coalescence and breakage mechanisms in three different bubble columns. *Chem. Eng. Sci.* **54** (21), 4767–4777.

Corchero, G., Medina, A. & Higuera, F. J. 2006 Effect of wetting conditions and flow rate on bubble formation at orifices submerged in water. *Colloids Surf. A* **290** (1-3), 41–49.

Coulaloglou, C. & Tavlarides, L. L. 1977 Description of interaction processes in agitated liquid-liquid dispersions. *Chem. Eng. Sci.* **32** (11), 1289–1297.

Cummings, A. 1986 Transient and multiple frequency sound transmission through perforated plates at high amplitude. *J. Acoust. Soc. Am.* **79** (4), 942–951.

Davidson, J. F. & Schuler, B. O. G. 1960*a* Bubble formation at an orifice in a viscous liquid. *Trans. Inst. Chem. Engrs.* **38**, 144–154.

Davidson, J. F. & Schuler, B. O. G. 1960*b* Bubble formation at an orifice in an inviscid liquid. *Trans. Instn. Chem. Engrs.* **38**, 335–342.

Di Bari, S. & Robinson, A. J. 2013 Adiabatic bubble growth in uniform DC electric fields. *Exp. Therm Fluid Sci.* **44**, 114–123.

Dollet, B., Van Hoeve, W., Raven, J.-P., Marmottant, P. & Versluis, M. 2008 Role of the channel geometry on the bubble pinch-off in flow-focusing devices. *Phys. Rev. Lett.* **100** (3), 034504.

Donnelly, R. & Glaberson, W. 1966 Experiments on the capillary instability of a liquid jet. *Proc. Roy. Soc.* **A290**, 547–566.

Eggers, J. & Dupont, T. F. 1994 Drop formation in a one-dimensional approximation of the Navier–Stokes equation. *J. Fluid Mech.* **262**, 205–221.

Eggers, J. & Villermaux, E. 2008 Physics of liquid jets. *Rep. Prog. Phys.* **71** (3), 036601.

Evangelio, A., Campo-Cortes, F. & Gordillo, J. M. 2015 Pressure gradient induced generation of microbubbles. *J. Fluid Mech.* **778**, 653–668.

Ferrara, K., Pollard, R. & Borden, M. 2007 Ultrasound microbubble contrast agents: fundamentals and application to gene and drug delivery. *Annu. Rev. Biomed. Eng.* **9**, 415–447.

Figueroa-Espinoza, B., Mena, B., Aguilar-Corona, A. & Zenit, R. 2018 The lifespan of clusters in confined bubbly liquids. *Int. J. Multiphase Flow* **106**, 138–146.

Figueroa-Espinoza, B. & Zenit, R. 2005 Clustering in high Re monodispersed bubbly flows. *Phys. Fluids* **17** (9), 091701.

Filella, A., Ern, P. & Roig, V. 2015 Oscillatory motion and wake of a bubble rising in a thin-gap cell. *J. Fluid Mech.* **778**, 60–88.

Filella, A., Ern, P. & Roig, V. 2019 Interaction of two oscillating bubbles rising in a thin-gap cell: vertical entrainment and interaction with vortices. *J. Fluid Mech.* (under review) .

Friedlander, S. K. 1977 *Smoke, dust and haze*. Wiley, New York.

Frommhold, P. E., Lippert, A., Holsteyns, F. L. & Mettin, R. 2014 High-speed monodisperse droplet generation by ultrasonically controlled micro-jet breakup. *Exp. Fluids* **55** (4), 1716.

Fu, Y. & Liu, Y. 2016 Development of a robust image processing technique for bubbly flow measurement in a narrow rectangular channel. *Int. J. Multiphase Flow* **84**, 217–228.

Fujikawa, S., Zhang, R., Hayama, S. & Peng, G. 2003 The control of micro-air-bubble generation by a rotational porous plate. *Int. J. Multiphase Flow* **29** (8), 1221–1236.

Gañán-Calvo, A. M. 2004 Perfectly monodisperse microbubbling by capillary flow focusing: An alternate physical description and universal scaling. *Phys. Rev. E* **69** (2), 027301.

Gañán-Calvo, A. M. & Gordillo, J. M. 2001 Perfectly monodisperse microbubbling by capillary flow focusing. *Phys. Rev. Lett.* **87**, 274501.

García, F. J., González, H., Castrejón-Pita, J. R. & Castrejón-Pita, A. A. 2014 The breakup length of harmonically stimulated capillary jets. *App. Phys. Lett.* **105** (9), 094104.

Garstecki, P., Gitlin, I., DiLuzio, W., Whitesides, G. M., Kumacheva, E. & Stone, H. A. 2004 Formation of monodisperse bubbles in a microfluidic flow-focusing device. *Appl. Phys. Lett.* **85**, 2649–2651.

Gekle, S., Peters, I. R., Gordillo, J. M., van der Meer, D. & Lohse, D. 2010 Supersonic air flow due to solid-liquid impact. *Phys. Rev. Lett.* **104** (2), 024501.

Goedde, E. & Yuen, M. 1970 Experiments on liquid jet instability. *J. Fluid Mech.* **40** (3), 495–511.

González, H. & García, F. 2009 The measurement of growth rates in capillary jets. *J. Fluid Mech.* **619**, 179–212.

González, R. C. & Woods, R. E. 2002 *Digital image processing*. Prentice-Hall, USA.

Gordillo, J. M. 2008 Axisymmetric bubble collapse in a quiescent liquid pool. I. Theory and numerical simulations. *Phys. Fluids* **20** (11), 112103.

Gordillo, J. M., Cheng, Z., Gañán-Calvo, A. M., Márquez, M. & Weitz, D. A. 2004 A new device for the generation of microbubbles. *Phys. Fluids* **16** (8), 2828–2834.

Gordillo, J. M., Gañán-Calvo, A. M. & Pérez-Saborid, M. 2001 Monodisperse microbubbling: Absolute instabilities in coflowing gas–liquid jets. *Phys. Fluids* **13** (12), 3839–3842.

Gordillo, J. M., Sevilla, A. & Martínez-Bazán, C. 2007 Bubbling in a co-flow at high Reynolds numbers. *Phys. Fluids* **19** (7), 077102.

Gordillo, J. M., Sevilla, A., Rodríguez-Rodríguez, J. & Martínez-Bazán, C. 2005 Axisymmetric bubble pinch-off at high Reynolds numbers. *Phys. Rev. Lett.* **95** (19), 194501.

Grinis, L. & Monin, Y. 1999 Influence of vibrations on gas bubble formation in liquids. *Chem. Eng. Technol.* **22** (5), 439–442.

Guerrero, J., González, H. & García, F. J. 2012 Spatial modes of capillary jets, with application to surface stimulation. *J. Fluid Mech.* **702**, 354–377.

Gutiérrez-Montes, C., Bolaños-Jiménez, R., Sevilla, A. & Martínez-Bazán, C. 2013 Experimental and numerical study of the periodic bubbling regime in planar co-flowing air–water sheets. *Int. J. Multiphase Flow* **50**, 106–119.

Gutiérrez-Montes, C., Bolaños-Jiménez, R., Sevilla, A. & Martínez-Bazán, C. 2014 Bubble formation in a planar water–air–water jet: Effects of the nozzle geometry and the injection conditions. *Int. J. Multiphase Flow* **65**, 38–50.

Hibiki, T. & Ishii, M. 2000 Two-group interfacial area transport equations at bubbly-to-slug flow transition. *Nuc. Eng. Des.* **202** (1), 39–76.

Hijano, A. J., Loscertales, I. G., Ibáñez, S. E. & Higuera, F. J. 2015 Periodic emission of droplets from an oscillating electrified meniscus of a low-viscosity, highly conductive liquid. *Phys. Rev. E* **91** (1), 013011.

Hirsch, C. 2007 *Numerical computation of internal and external flows: The fundamentals of computational fluid dynamics*. Elsevier.

Howe, M. S. 1998 *Acoustics of fluid-structure interactions*. Cambridge university press.

Huisman, S. G., Ern, P. & Roig, V. 2012 Interaction and coalescence of large bubbles rising in a thin gap. *Phys. Rev. E* **85** (2), 027302.

Jiménez-González, J. I. & Huera-Huarte, F. J. 2017 Experimental sensitivity of vortex-induced vibrations to localized wake perturbations. *J. Fluids Struct.* **74**, 53–63.

Kalaaji, A., Lopez, B., Attane, P. & Soucemarianadin, A. 2003 Breakup length of forced liquid jets. *Phys. Fluids* **15**, 2469–2479.

Kalkach-Navarro, S., Lahey Jr, R. T. & Drew, D. A. 1994 Analysis of the bubbly/slug flow regime transition. *Nuc. Eng. Des.* **151** (1), 15–39.

Kamp, A. M., Chesters, A. K., Colin, C. & Fabre, J. 2001 Bubble coalescence in turbulent flows: a mechanistic model for turbulence-induced coalescence applied to microgravity bubbly pipe flow. *Int. J. Multiphase Flow* **27** (8), 1363–1396.

Kim, I. & Sirignano, W. A. 2000 Three-dimensional wave distortion and disintegration of thin planar liquid sheets. *J. Fluid Mech.* **410**, 147–183.

Kocamustafaogullari, G. & Ishii, M. 1995 Foundation of the interfacial area transport equation and its closure relations. *Int. J. Heat Mass Transfer* **38** (3), 481–493.

Kolev, N. 1993 Fragmentation and coalescence dynamics in multiphase flows. *Exp. Thermal Fluid Sci.* **6** (3), 211–251.

Kolmogorov, A. N. 1949 On the breakage of drops in a turbulent flow. *Dokl Akad Nauk SSSR* **66**, 825–828.

Krishna, R. & Ellenberger, J. 2003 Influence of low-frequency vibrations on bubble and drop sizes formed at a single orifice. *Chem. Eng. and Process* **42** (1), 15–21.

Kumar, R. & Kuloor, N. K. 1970 The formation of bubbles and drops. *Adv. Chem. Eng.* **8**, 255–368.

Lafrance, P. 1975 Nonlinear breakup of a laminar liquid jet. *Phys. Fluids* **18** (4), 428–432.

Lasheras, J. C., Eastwood, C., Martínez-Bazán, C. & Montañés, J. L. 2002 A review of statistical models for the break-up of an immiscible fluid immersed into a fully developed turbulent flow. *Int. J. Multiphase Flow* **28** (2), 247–278.

Lee, H. C. 1974 Drop formation in a liquid jet. *IBM J. Res. Dev.* **18** (4), 364–369.

Leib, S. & Goldstein, M. 1986*a* Convective and absolute instability of a viscous liquid jet. *Phys. Fluids* **29** (4), 952–954.

Leib, S. & Goldstein, M. 1986*b* The generation of capillary instabilities on a liquid jet. *J. Fluid Mech.* **168**, 479–500.

Liao, Y. & Lucas, D. 2009 A literature review of theoretical models for drop and bubble breakup in turbulent dispersions. *Chem. Eng. Sci.* **64** (15), 3389–3406.

Liao, Y. & Lucas, D. 2010 A literature review on mechanisms and models for the coalescence process of fluid particles. *Chem. Eng. Sci.* **65** (10), 2851–2864.

Lichtarowicz, A., Duggins, R. & Markland, E. 1965 Discharge coefficients for incompressible non-cavitating flow through long orifices. *J. Mech. Engng. Sci.* **7** (2), 210–219.

Longuet-Higgins, M. S., Kerman, B. R. & Lunde, K. 1991 The release of air bubbles from an underwater nozzle. *J. Fluid Mech.* **230**, 365–390.

Lozano, A., García-Olivares, A. & Dopazo, C. 1998 The instability growth leading to a liquid sheet breakup. *Phys. Fluids* **10** (9), 2188–2197.

Luong, T., Howe, M. S. & McGowan, R. S. 2005 On the Rayleigh conductivity of a bias–flow aperture. *J. Fluids Struct.* **21** (8), 769–778.

Maier, C. G. 1927 *U. S. Bur. Mines Bull.* **260**.

Makuta, T., Suzuki, R. & Nakao, T. 2013 Generation of microbubbles from hollow cylindrical ultrasonic horn. *Ultrasonics* **53** (1), 196–202.

Makuta, T., Takemura, F., Hihara, E., Matsumoto, Y. & Shoji, M. 2006 Generation of micro gas bubbles of uniform diameter in an ultrasonic field. *J. Fluid Mech.* **548**, 113–131.

Marchisio, D. L. & Fox, R. O. 2013 *Computational models for polydisperse particulate and multiphase systems*. Cambridge University Press.

Martínez-Bazán, C. 1999 Splitting and dispersion of bubbles by turbulence. PhD thesis, University of California San Diego, USA.

Martínez-Bazán, C., Montañés, J. L. & Lasheras, J. C. 1999*a* On the breakup of an air bubble injected into a fully developed turbulent flow. Part 1. Breakup frequency. *J. Fluid Mech.* **401**, 157–182.

Martínez-Bazán, C., Montañés, J. L. & Lasheras, J. C. 1999*b* On the breakup of an air bubble injected into a fully developed turbulent flow. Part 2. Size PDF of the resulting daughter bubbles. *J. Fluid Mech.* **401**, 183–207.

Martínez-Bazán, C., Rodríguez-Rodríguez, J., Deane, G. B., Montañés, J. L. & Lasheras, J. C. 2010 Considerations on bubble fragmentation models. *J. Fluid Mech.* **661**, 159–177.

Mehring, C. & Sirignano, W. A. 1999 Nonlinear capillary wave distortion and disintegration of thin planar liquid sheets. *J. Fluid Mech.* **388**, 69–113.

Mehring, C. & Sirignano, W. A. 2001 Nonlinear capillary waves on swirling, axisymmetric free liquid films. *Int. J. Multiphase Flow* **27** (10), 1707–1734.

Meier, G. E. A., Klöpper, A. & Grabitz, G. 1992 The influence of kinematic waves on jet break down. *Exp. Fluids* **12** (3), 173–180.

Mercado, J. M., Gomez, D. C., Van Gils, D., Sun, C. & Lohse, D. 2010 On bubble clustering and energy spectra in pseudo-turbulence. *J. Fluid Mech.* **650**, 287–306.

Monkewitz, P. A. & Sohn, K. 1988 Absolute instability in hot jets. *AIAA J.* **26** (8), 911–916.

Mu, K., Si, T., Li, E., Xu, R. X. & Ding, H. 2018 Numerical study on droplet generation in axisymmetric flow focusing upon actuation. *Phys.Fluids* **30** (1), 012111.

Najafi, A. S., Xu, Z. & Masliyah, J. 2008 Single micro-bubble generation by pressure pulse technique. *Chem. Eng. Sci.* **63** (7), 1779–1787.

Oelgemoller, M. 2016 Solar photochemical synthesis: from the beginnings of organic photochemistry to the solar manufacturing of commodity chemicals. *Chem. Rev.* **116** (17), 9664–9682.

Oğuz, H. N. & Prosperetti, A. 1993 Dynamics of bubble growth and detachment from a needle. *J. Fluid Mech.* **257**, 111–145.

Ohl, C. D. 2001 Generator for single bubbles of controllable size. *Rev. Sci. Instrum.* **72** (1), 252–254.

Ostmann, S. & Schwarze, R. 2018 A compact device for the deterministic generation of medium-sized bubbles. *Rev. Sci. Instrum.* **89** (12), 125108.

Otsu, N. 1979 A threshold selection method from gray-level histograms. *IEEE Trans. SMC* **9** (1), 62–66.

Palanchon, P., Klein, J. & de Jong, N. 2003 Production of standardized air bubbles: Application to embolism studies. *Rev. Sci. Instrum.* **74** (4), 2558–2563.

Prince, M. J. & Blanch, H. W. 1990 Bubble coalescence and break-up in air-sparged bubble columns. *AIChE J.* **36** (10), 1485–1499.

Pruvost, J., Le Borgne, F., Artu, A. & Legrand, J. 2017 Development of a thin-film solar photobioreactor with high biomass volumetric productivity (AlgoFilm©) based on process intensification principles. *Algal Res.* **21**, 120–137.

Rayleigh, J. W. S. 1878 On the instability of jets. *Proc. R. Soc. Lond.* **10**, 4–13.

Rayleigh, J. W. S. 1945 *The theory of sound*. Dover, New York.

Riboux, G., Risso, F. & Legendre, D. 2010 Experimental characterization of the agitation generated by bubbles rising at high reynolds number. *J. Fluid Mech.* **643**, 509–539.

Risso, F. 2016 Physical interpretation of probability density functions of bubble-induced agitation. *J. Fluid Mech.* **809**, 240–263.

Risso, F. 2018 Agitation, mixing, and transfers induced by bubbles. *Annu. Rev. Fluid Mech.* **50**, 25–48.

Risso, F. & Ellingsen, K. 2002 Velocity fluctuations in a homogeneous dilute dispersion of high-reynolds-number rising bubbles. *J. Fluid Mech.* **453**, 395–410.

Rodríguez-Rodríguez, J., Martínez-Bazán, C. & Montañés, J. L. 2003 A novel particle tracking and break-up detection algorithm: application to the turbulent break-up of bubbles. *Meas. Sci. Technol.* **14** (8), 1328.

Rodríguez-Rodríguez, J., Sevilla, A., Martínez-Bazán, C. & Gordillo, J. M. 2015 Generation of microbubbles with applications to industry and medicine. *Annu. Rev. Fluid Mech.* **47**, 405–429.

Roig, V., Roudet, M., Risso, F. & Billet, A.-M. 2012 Dynamics of a high-Reynolds-number bubble rising within a thin gap. *J. Fluid Mech.* **707**, 444–466.

Roudet, M., Billet, A.-M., Cazin, S., Risso, F. & Roig, V. 2017 Experimental investigation of interfacial mass transfer mechanisms for a confined high-reynolds-number bubble rising in a thin gap. *AIChE J.* **63** (6), 2394–2408.

Ruiz-Rus, J., Bolaños-Jiménez, R., Gutiérrez-Montes, C., Sevilla, A. & Martínez-Bazán, C. 2017 Controlled formation of bubbles in a planar co-flow configuration. *Int. J. Multiphase Flow* **89**, 69–80.

Rusche, H. 2003 Computational fluid dynamics of dispersed two-phase flows at high phase fractions. PhD thesis, Imperial College London (University of London).

Rutland, D. F. & Jameson, G. J. 1970 Theoretical prediction of the sizes of drops formed in the breakup of capillary jets. *Chem. Eng. Sci.* **25** (11), 1689–1698.

Sanada, T. & Abe, K. 2013 Generation of single bubbles of various sizes using a slitting elastic tube. *Rev. Sci. Instrum.* **84** (8), 085106.

Sauret, A. & Cheung Shum, H. 2012 Forced generation of simple and double emulsions in all-aqueous systems. *App. Phys. Lett.* **100** (15), 154106.

Sevilla, A., Gordillo, J. M. & Martinez-Bazán, C. 2002 The effect of the diameter ratio on the absolute and convective instability of free coflowing jets. *Phys. Fluids* **14** (9), 3028–3038.

Sevilla, A., Gordillo, J. M. & Martínez-Bazán, C. 2005*a* Bubble formation in a coflowing air–water stream. *J. Fluid Mech.* **530**, 181–195.

Sevilla, A., Gordillo, J. M. & Martínez-Bazán, C. 2005*b* Transition from bubbling to jetting in a coaxial air–water jet. *Phys. Fluids* **17** (1), 018105.

Shirota, M., Sanada, T., Sato, A. & Watanabe, M. 2008 Formation of a submillimeter bubble from an orifice using pulsed acoustic pressure waves in gas phase. *Phys. Fluids* **20** (4), 043301.

Sirignano, W. A. & Mehring, C. 2000 Review of theory of distortion and disintegration of liquid streams. *Prog. Energy Comb. Sci.* **26** (4-6), 609–655.

Song, B. & Springer, J. 1996 Determination of interfacial tension from the profile of a pendant drop using computer-aided image processing: 2. Experimental. *J. Colloid Interface Sci.* **184** (1), 77–91.

Stewart, C. 1995 Bubble interaction in low-viscosity liquids. *Int. J. Multiphase Flow* **21** (6), 1037–1046.

Stone, H. A., Stroock, A. D. & Ajdari, A. 2004 Engineering flows in small devices: microfluidics toward a lab-on-a-chip. *Annu. Rev. Fluid Mech.* **36**, 381–411.

Swift, D. L. & Friedlander, S. 1964 The coagulation of hydrosols by brownian motion and laminar shear flow. *J. Colloid Sci.* **19** (7), 621–647.

Thobie, C., Gadoin, E., Blel, W., Pruvost, J. & Gentric, C. 2017 Global characterization of hydrodynamics and gas-liquid mass transfer in a thin-gap bubble column intended for microalgae cultivation. *Chem. Eng. Process.* **122**, 76–89.

Tsouris, C. & Tavlarides, L. L. 1994 Breakage and coalescence models for drops in turbulent dispersions. *AIChE J.* **40** (3), 395–406.

Tsuge, H., Tanaka, Y., Terasaka, K. & Matsue, H. 1997 Bubble formation in flowing liquid under reduced gravity. *Chem. Eng. Sci.* **52** (21-22), 3671–3676.

Valentas, K. J. & Amundson, N. R. 1966 Breakage and coalescence in dispersed phase systems. *I&EC Fundamentals* **5** (4), 533–542.

Vega, E. J., Montanero, J. M. & Fernández, J. 2009 On the precision of optical imaging to study free surface dynamics at high frame rates. *Exp. Fluids* **47** (2), 251–261.

Vejrazka, J., Fujasová, M., Stanovsky, P., Ruzicka, M. C. & Drahoš, J. 2008 Bubbling controlled by needle movement. *Fluid Dyn. Res.* **40** (7-8), 521.

Waghmare, Y., Rice, R. & Knopf, F. 2008 Mass transfer in a viscous bubble column with forced oscillations. *Ind. Eng. Chem. Res.* **47** (15), 5386–5394.

Wang, N., Chen, X., Yuan, J., Wang, G., Li, Y., Zhang, H. & Liu, Y. 2016 Bubble formation at a submerged orifice in high-speed horizontal oscillation. *Metall. Mater. Trans. B* **47** (6), 3362–3374.

Wang, S., Hernan, B. J. & Chen, C.-L. 2018 Towards enhanced bubble detachment within a thin liquid film by electrowetting with voltage modulation. *Phys. Fluids* **30** (6), 062102.

Wang, T., Wang, J. & Jin, Y. 2005 Theoretical prediction of flow regime transition in bubble columns by the population balance model. *Chem. Eng. Sci.* **60** (22), 6199–6209.

Williams, F. A. 1985 *Combustion theory*. Addison-Wesley, Redwood City, CA.

Wu, Q., Kim, S., Ishii, M. & Beus, S. 1998 One-group interfacial area transport in vertical bubbly flow. *Int. J. Heat Mass Transfer* **41** (8-9), 1103–1112.

Xu, H., Yan, R., Wang, S. & Chen, C.-L. 2017 Bubble detachment assisted by electrowetting-driven interfacial wave. *Phys. Fluids* **29** (10), 102105.

Yang, C., Qiao, R., Zhu, Z., Xu, R. & Si, T. 2019 Manipulation of jet breakup length and droplet size in axisymmetric flow focusing upon actuation. *Phys. Fluids* **31**, 091702.

Yao, W. & Morel, C. 2004 Volumetric interfacial area prediction in upward bubbly two-phase flow. *Int. J. Heat Mass Transfer* **47** (2), 307–328.

Yellin, E. & Peskin, C. 1975 Large amplitude pulsatile water flow across an orifice. *J. Dyn. Syst. - T. ASME* **97** (1), 92–95.

Zenit, R., Koch, D. L. & Sangani, A. S. 2001 Measurements of the average properties of a suspension of bubbles rising in a vertical channel. *J. Fluid Mech.* **429**, 307–342.

Zhu, P., Tang, X., Tian, Y. & Wang, L. 2016*a* Pinch-off of microfluidic droplets with oscillatory velocity of inner phase flow. *Sci. Rep.* **6**, 31436.

Zhu, P., Tang, X. & Wang, L. 2016*b* Droplet generation in co-flow microfluidic channels with vibration. *Microfluid. Nanofluid.* **20** (3), 47.

Zhu, Y., Oğuz, H. N. & Prosperetti, A. 2000 On the mechanism of air entrainment by liquid jets at a free surface. *J. Fluid Mech.* **404**, 151–177.